FULLY AUTOMATIC 3D OBJECT RECONSTRUCTION FROM

MULTI-VIEW RANGE SCAN DATA

By

JUNGJAE YIM

Bachelor of Information Communication Engineering
Hanbat National University
Daejeon, South Korea
2007

Master of Science in Electrical Engineering
Oklahoma State University
Stillwater, Oklahoma
2009

Submitted to the Faculty of the
Graduate College of the
Oklahoma State University
in partial fulfillment of
the requirements for
the Degree of
DOCTOR OF PHILOSOPHY
Dec, 2017

FULLY AUTOMATIC 3D OBJECT RECONSTRUCTION FROM

MULTI-VIEW RANGE SCAN DATA

Dissertation Approved:

Dr. Guoliang Fan
_____
Dissertation Advisor

Dr. Martin Hagan
_____

Dr. Weihua Sheng
_____

Dr. Sundar V. Madihally
_____

ACKNOWLEDGMENTS

Writing a dissertation is a long and arduous journey. I wish to take this opportunity to show my appreciation to all those people who have greatly contributed their time and effort to help me throughout this long process.

Most of all, I would like to express my sincere and deep gratitude to my advisor, Dr. Guoliang Fan, for his constant guidance and support throughout my graduate studies. His encouragement, knowledge, insightful suggestions, and patient guidance have helped me immensely through my long research process and dissertation writing. I would not have completed this dissertation without his help and encouragement.

I would also like to thank the members of my dissertation committee, Dr. Martin Hagan, Dr. Weihua Sheng, and Dr. Sundar V. Madihally, for their thoughtful suggestions and feedback regarding my dissertation. I also owe great thanks to my colleagues in the VCIPL lab for their warm comradeship and encouragement.

My special thanks go to all the members of my family back in Korea who have been greatly supportive of my graduate studies, especially to my parents and parents in-law for all their support and strong belief they have given me over the years in my long journey. Last, but most significantly, my heartfelt thanks go to my dear wife, Seungmin Yun, and my son, Jiwon Yim, for their unceasing love, prayers, and unshakable belief in me. Their encouragement and support gave me strength and made this work possible.

Name: JUNGJAE YIM

Date of Degree: Dec, 2017

Title of Study: FULLY AUTOMATIC 3D OBJECT RECONSTRUCTION FROM MULTI-VIEW RANGE SCAN DATA

Major Field: ELECTRICAL ENGINEERING

Abstract:

3D surface registration of two or more range scans is an important step in building a complete 3D model of an object. When the overlaps between multi-view scans are insufficient, it is highly compulsory to involve good initial alignment that typically requires some prior assumption such as pre-defined initial camera configuration or the use of landmarks. Specifically, this research attempts to address the problem of registering two or more range scans captured from the complex 3D objects which entail an extremely small amount of overlaps and where camera initialization or configuration is not known. This newly proposed algorithm consists of two steps of registration: coarse registration and fine registration. First, coarse registration involves two new techniques that can create an enclosed mesh model from a single range scan to extract reliable 3D surface features for initial alignment, Partial Artificial Heat Kernel Signature (PA-HKS) and Artificial Symmetric Volume Heat Kernel Signature (AS-HKS). Coarse registration is successfully achieved by estimation of the feature descriptors from the generated artificial 3D volume and by Heat Kernel Signature (HKS) from the artificial 3D mesh data, as an important attempt to correctly identify correspondences among the partial 3D range scan data. Secondly, fine registration involves a Modified Multi-view Iterative Contour Coherence (MM-ICC) algorithm. On the basis of the preliminary registration, the coarsely aligned partial range scan data is matched by the MM-ICC method in the fine registration step. This unique combination allows us to successfully handle multi-view range scan data with large out-of-plane rotation and limited overlaps between two adjacent views and without any camera information. The experimental results of a number of complex 3D objects clearly illustrate and validate the effectiveness and robustness of the proposed approach. To be more specific, the research outcomes are found to be highly successful even in case of 1-2% overlapping areas, whereas the previous studies require at least 45-50% of overlapping regions.

TABLE OF CONTENTS

LIST OF TABLES

LIST OF FIGURES

CHAPTER I

INTRODUCTION

1.1 Motivation

3D model reconstruction has long attracted attention as a highly versatile tool which can be adopted in a variety of fields [7–16]. For instance, modeling a person or an object has been applied to the field of 3D animation, robotics, online merchandizing, modeling spaces for exploration, clinical purposes, or surveillance, and so on. In the field of 3D animation, the major technique most frequently adopted so far is to utilize 3D markers [17, 18]. The 3D markers attached to the actors' body are carefully tracked; on the basis of this tracking result, it is possible to reconstruct the movement of the 3D animation characters. However, there is a limitation in using these 3D makers; the 3D makers are available restrictively in the indoor settings. Moreover, in the field of online merchandizing, an interesting application has recently been introduced and received more attention. Based on the body scanning data obtained through a laser scanner [19, 20], consumers are able to try on the items of their interest in virtual reality before making a decision, as exemplified in Figure 1.1. In addition, 3D reconstruction plays some important roles in the clinical field. It is now well known that 3D body scanning, such as CT and MRI [21, 22], is highly capable of providing more precise information in comparison to 2D and further allows medical teams to offer better and more effective treatment for patients. One step further, a simulation of surgery practice becomes possible and proves its effectiveness with using a scanned body in the virtual 3D spaces [23–25]. Figure 1.1 well illustrates a few examples of 3D modeling applications to a variety of different fields [1–4].
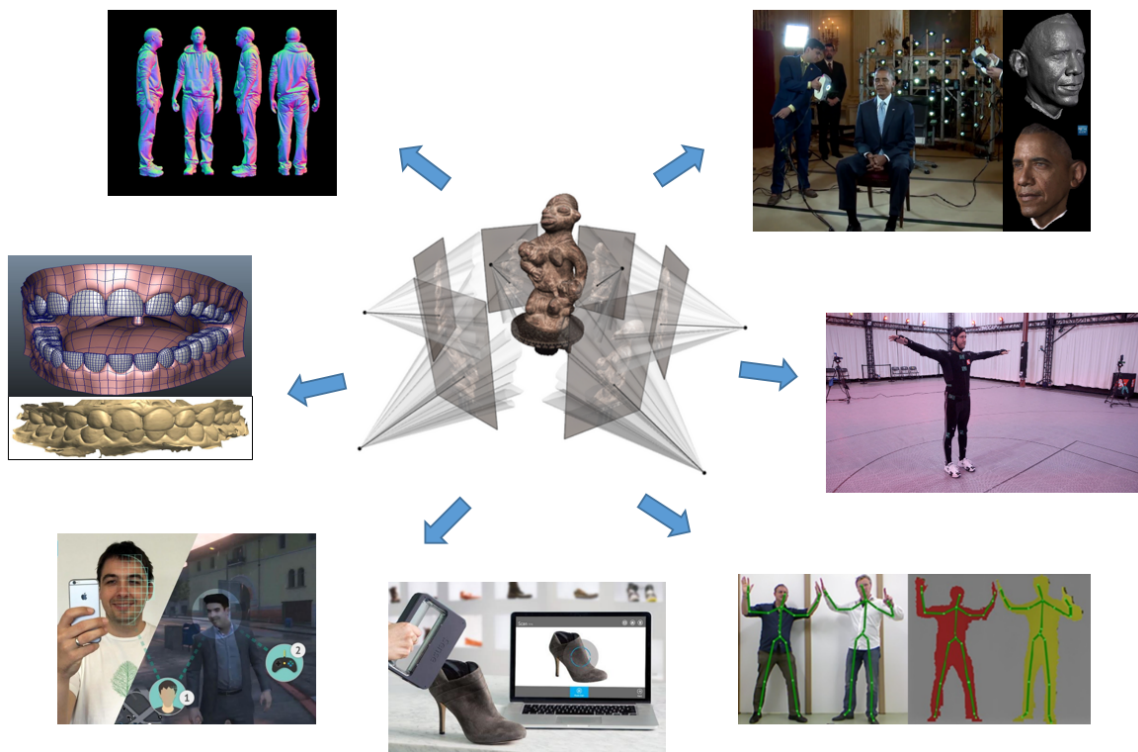
Figure 1.1: Applications of 3D modeling in different fields [1–4].

Despite the importance of 3D modeling, just a few years ago, the 3D scanners which can provide accurate 3D range scan data were not easily available for individual uses mainly due to some practical reasons including sizes and prices. However, the recent research and technique advancement has developed a number of devices that entails a portable size appropriate to individual uses and that can provide accurate depth information, such as Kinect, Xtion pro, Artec Eva 3D scanner, Sense 3D Scanner, and so on [1–4, 23, 26–28].

Figure 1.2 demonstrates the examples of the newly developed devices. These depth sensors are able to measure the depth of the object in front of a camera and to provide 2.5D depth images at real-time. Moreover, the depth images offered entail competitive resolution. In Figure 1.2, (d) and (h) are the excerpts from the movies, *Minority Report(2002)*, and *Divergent(2014)*, respectively. These two science fictions interestingly illustrate some significant research advancement in the field of 3D human

2

Figure 1.2: Current published depth camera and future of moving camera sensors; (a)-(c): Kinect, Sense, Xton pro, (e)-(g): Go!SCAN, Kinect pro 2, Hover.

body reconstruction using multiple moving range sensors. In order to translate these achievements into reality, some major research challenges should be properly overcome, such as 3D registration with no initialization, using barely overlapped data due to the limited number of sensors, with inconsistent alignment due to moving sensors and targets, and so on [16, 29–33]. Therefore, the present dissertation paper proposes a new algorithm that is capable of addressing and overcoming the challenges of the current 3D reconstruction research. The proposed paper aims to successfully perform full 3D reconstruction from multi-views range scan data despite of the extremely low overlaps between views and further without any camera initialization and calibration.

1.2 Research Background

RGB-D cameras [3, 23, 26–28] have enhanced its reputation mainly because they are capable of generating dense 3D images; nevertheless, the RGB-D cameras fail to provide full 3D images due to occlusions and limited views. In order to obtain full modeling reconstruction in 3D, it is highly compulsory that the data extracted should represent all the regions of the scene or object. It is important and required for successful reconstruction outcomes to include common features which are possibly

to be matched and/or prior information about the targeting environment which can provide some useful background to infer alignment. It can intuitively make sense that corresponding features are likely to exist in the overlapping regions of the views. Combining the data extracted from these corresponding pairs of the overlapping views allows us to successfully perform a full 3D reconstruction with higher accuracy [34–36].

A great deal of the previous research has identified some major research challenges in generating a full closed 3D object from the 2.5D depth information depending on the various settings, including the number of depth cameras used (single or multiple), or whether a camera is fixed or moving. First, in case of using fixed multiple depth cameras, the initialization of the multiple cameras is required as a crucial step. In order to perform registration of the input data, it is compulsory to operate calibration of the camera using a calibration board or 3D markers. Moreover, in case that the camera is shifted even just a little, the calibration step should be repeated [37–39]. Another challenge is found in case of using a fixed single depth camera. In this setting, the single depth camera entails a fixed location and the target object is rotated; accordingly, it requires some extra equipment such as rotational discs, etc., or needs the specially designed setting where the object is rotating by itself and shows its different perspective surface directly to the depth camera. Hence, even when using a fast registration algorithm, it is hardly possible to plot several depth data from the different perspective surface simultaneously and to perform real-time 3D model reconstruction [40–42]. In addition, the registration can be mostly performed limitedly when the target is rigid or when the non-rigid target object has extremely small motion. The most challenging point is to identify the correct correspondences of the features in the feature-based registration in order to find the rotation angle gap among the different perspective depth images. The third challenge can be explained in case of using a moving single-depth camera [43, 44]. It is closely related to the real-time algorithm to merge the adjacent depth image. The main

research task here is how to merge the multi-view depth data and to refine the merged information. The Kinect fusion [44–46] is one of the most well-known algorithms in this category. This methodological technique does not limit a target to a rigid one; however, in case of non-rigid target objects, it is extremely hard to attain successful 3D reconstruction outcomes when the non-rigid target or the depth camera is moving fast. In other words, in order to achieve the prosperous 3D reconstruction, it is mandatorily required to involve high overlapping data and low perspective angles between adjacent depth image frames; that is, a decent amount of adjacent depth image frames is highly compulsory to guarantee the good results. As shown, these previous studies have also well recognized some major research challenges mentioned above, including registration without initialization, registration using low overlapping data, and registration by recovering the alignment of the moving sensors, and the non-rigid target. In order to guarantee diverse applications, these limitations and challenges should be well addressed and overcome especially on the 3D reconstruction though the registration of the multi-view range scan data which are extracted from the multiple moving depth sensors. This calls for the needs of more research. Accordingly, the present research proposes to overcome these research challenges.

1.3   Research Objectives and Challenges

In the present dissertation study, a new algorithm is introduced as an attempt to provide a robust and highly precise registration outcomes without any initialization. The proposed algorithm is expected to show a competitive performance even in the setting of no pre-defined rough alignment given and with the range scan data that entails extremely low overlapping areas from large main rotation angles. On the basis of the fact that range scan data is extracted from the depth camera in one single direction, the range scan data involves 3D depth in one particular direction and accordingly it is inevitable that the invisible parts of the target exist. This feature

5

results in one of the major research challenges; that is, it is highly perplexing to generate a 3D model through registration of the range scan data with no initialization. False correspondences are frequently identified mainly because multiple range scans which are used for 3D registration contain non-overlapping regions. These false features have a significant effect on the final resolution. As claimed in the studies by Makadia [31], Chow [47] and Besl [48], approximately 45-50% is required to obtain successful outcomes as the minimum percentages of overlapping regions. This leads to an important research challenge and a need to develop the algorithm that is capable of producing robust outcomes even in case of extremely low overlaps. The present algorithm is proposed mainly to address and tackle this challenge. For this research purpose, the present dissertation paper suggests the two-fold procedure including the coarse registration and the combination algorithm. The first process aims to deal with the difficulties in registration without any initialization and with extremely low overlapping condition whereas the second process involves the find registration process in order to increase accuracy. The main objectives of the current research are addressed as follows:

- The proposed algorithm aims to successfully perform the registration with no initialization and/or camera calibration.

- The proposed algorithm aims to successfully perform the registration in a rough setting with partial and highly limited overlapping data.

- The proposed algorithm aims to significantly enhance the accuracy of 3D surface registration of multi-view range scan data, leading to more accurate and robust 3D model reconstruction.

1.3.1 Coarse Registration

The present research newly introduces the two algorithms for the coarse registration based on the Heat Kernel Signature(HKS) [5]: the Partial Artificial Heat Kernel Signatures (PA-HKS) algorithm and the Artificial Symmetry Heat Kernel Signatures (AS-HKS) algorithm. The HKS algorithm is, in general, applied to create the highly localized features from the 3D mesh model in the field of the pose estimation [43, 49] or the object recognition [50, 51]. The first PA-HKS coarse registration algorithm targets to operate 3D registration with no initialization and entails simpler and faster procedures. The latter one, the AS-HKS coarse registration, intends to provide more robust registration outcomes by decreasing the minimum number of the frames required and further guarantees higher accuracy even in the rough settings.
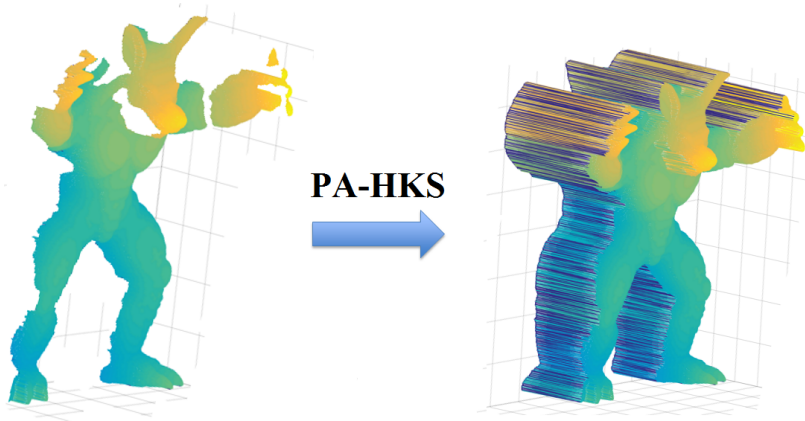
Figure 1.3: Illustration of PA-HKS.

Partial Artificial HKS (PA-HKS)

It is significant to discover the features from the partial range scan surface in order to operate the coarse registration with no initialization. As an attempt to achieve this goal, the HKS is utilized as a feature descriptor by using a curvature of the object surface. The previous research using HKS has shown that this technique could provide successful registration outcomes exclusively on the full 3D mesh data. However, in

case of the 2.5D range scan data which is created by self-occlusion, it is not possible to generate correct HKS descriptors in the boundary area. In order to address this research need, the improved and modified heat kernel features are developed to deal with the partially overlapping range scan data which are extracted from the different view angles. On the basis of HKS [5, 50], as the first step, a new Partial Artificial Heat Kernel Signature (PA-HKS) is proposed and performed to operate the coarse alignment of the multiple range scan data. Figure 1.3 shows the illustration of PA-HKS. This technique will be further discussed in more detail in Chapter 4.
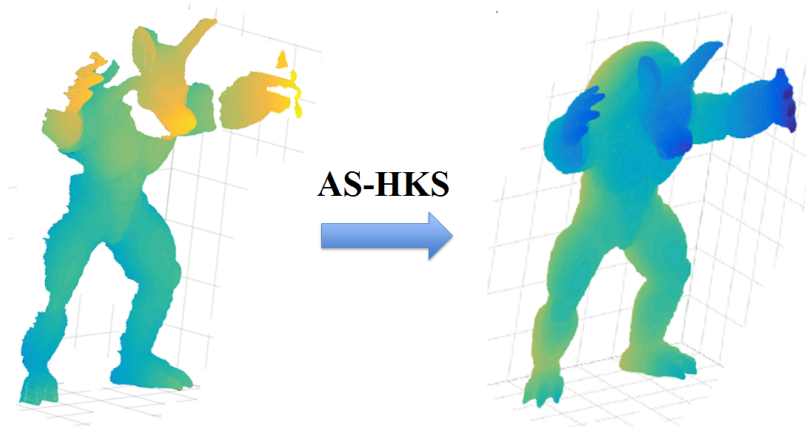
AS-HKS

Figure 1.4: Illustration of AS-HKS.

Artificial Symmetry HKS (AS-HKS)

As explained in the previous section, a new technique, the Partial Artificial Heat Kernel Signature (PA-HKS), is proposed to process the registration of the partial open 2.5D range scan data. It is true that this technique enables us to generate an accurate 3D model; nevertheless, this projection-based algorithm entails one major limitation when identifying an accurate matching model. Primarily because a mesh is created through projection, the visible surface mesh entails a consistency exclusively to the original target and the surface mesh in the invisible areas tends to show a big discrepancy. Further, the volume of each part of the target cannot involve an accurate

thickness, either. Accordingly, the extracted HKS keypoints are inaccurately located in the partial artificial mesh and tend to entail completely different and incorrect local curvatures around the boundary of the visible and invisible mesh. All in all, the HKS descriptors of the projection-based method are able to create the globally meaningful features in order to identify the corresponding feature points among the range scan data from different views. However, this method fails to generate locally meaning feature points. The HKS descriptors which are incorrectly extracted are not capable of attaining enough information to generate corresponding features.

This limitation of the PA-HKS becomes the starting point of the AS-HKS algorithm for the coarse registration. Hence, the present dissertation paper also proposes the Artificial Symmetry Volume Completion for 3D modeling as an attempt to cover the combination of local and global descriptors on the basis of the artificial symmetry volume meshes. The global features refer to the ones that entail the entire object with a single feature vector. These global features show a limited usage especially when the target object involves some occlusions, different poses, lighting, and/or intra-class variation. The local features are suggested, here in the study, to handle this research challenge. Figure 1.4 shows the illustration of AS-HKS. This proposed algorithm will be further elucidated in Chapter 5.

1.3.2 Fine Registration

This dissertation research also proposes the fine registration stage which is expected to generate final reconstruction outcomes with higher accuracy. In order to achieve more successful 3D reconstruction, the coarsely aligned 3D data which are obtained from the coarse registration process is thoroughly refined in this final stage.

The Modified M-ICC (MM-ICC) algorithm

The M-ICC algorithm [52] utilizes four partially overlapping range scan data in order to generate a 3D mesh model and is able to provide rather successful reconstruction outcomes. Nevertheless, this algorithm still involves some major limitations mainly because it always requires a certain assumption. It is compulsory, in the M-ICC algorithm, that the main rotation angle gap needs to be set by approximately 90 degrees among four input range scan data. In addition, the two pruning stages suggested are not enough to obtain higher accuracy. Among a deal of previous research which has made attempts to overcome these limitations, the MM-ICC algorithm is one of the studies to demonstrate the successful outcomes. The MM-ICC algorithm proposes a new additional pruning step in order to deal with the limitations and operate a more effective algorithm using the artificial partial 3D mesh. More details will be provided in Chapter 6.

1.4 Contributions

The present approach makes several contributions on 3D registration and reconstruction.

- First, the PA-HKS algorithm is proposed to competitively perform registration of the multiple partial range scan data with no initialization and calibration given in complex 3D object modeling. The original HKS algorithm functions on the basis of the gradient of the surface exclusively in the fully closed mesh model. Therefore, the present dissertation research attempts to address this limitation and to identify the features in the open 2.5D partial mesh. The proposed algorithm is able to generate the Partial Artificial (PA) mesh model; then the PA-HKS features are successfully extracted from the partial artificial mesh model created. This proposed algorithm enables us to find the corresponding

features over the different partial range scan data and also to provide the effective step for the coarse registration in fully automatic complete 3D modeling.

- Second, the AS-HKS algorithm, which is extended from the previous PA-HKS, is proposed in order to enhance reconstruction outcomes in identifying the features with higher accuracy by using both global and local feature vectors. This algorithm is capable of generating the artificial volume model closed to the original object; further, by using this volume model, it is possible to extract the features with both global and local descriptors and to identify more accurate correspondences of these features. Consequently, this algorithm provides more robust registration results compared to the PA-HKS mainly because the PA-HKS is able to obtain only the global descriptors.

- Third, the modified Multi-view Iterative Closest Contour (MM-ICC) algorithm is proposed as an attempt to enhance accuracy of the fine registration process in the setting with the extremely low overlapping data. The Multi-view Iterative Closest Contour (M-ICC) is the registration algorithm on the basis of the corresponding contours between two range scan data sets. The additional refinement step is suggested in order to obtain reconstruction outcomes with higher accuracy. As a result, this algorithm still promises good registration outcomes even in the setting where the data set has extremely low overlapping area due to huge rotation.

1.5 Outline

The present paper is organized as demonstrated in Figure 1.5. The succinct description of each chapter is presented as follows.

- In Chapter 1, the motivation and significance of this research is presented.

- In Chapter 2, the previous research work regarding 3D registration is reviewed in detail and categorized.

- In Chapter 3, the concept of the Heat Kernel Signatures(HKS) is introduced and further the Artificial Heat Kernel Signatures is proposed.

- In Chapter 4, the Partial-Artificial Heat Kernel Signatures (PA-HKS) is proposed in detail for the coarse registration.

- In Chapter 5, the Artificial-Symmetry Heat Kernel Signatures (AS-HKS) is proposed for the coarse registration.

- In Chapter 6, the Modified Multi-view Iterative Closest Contour (MM-ICC) is proposed for the fine registration.

- In Chapter 7, the experimental results are elucidated based on the combination of both coarse and fine registration.

- In Chapter 8, the current dissertation research is concluded and further future work is suggested.
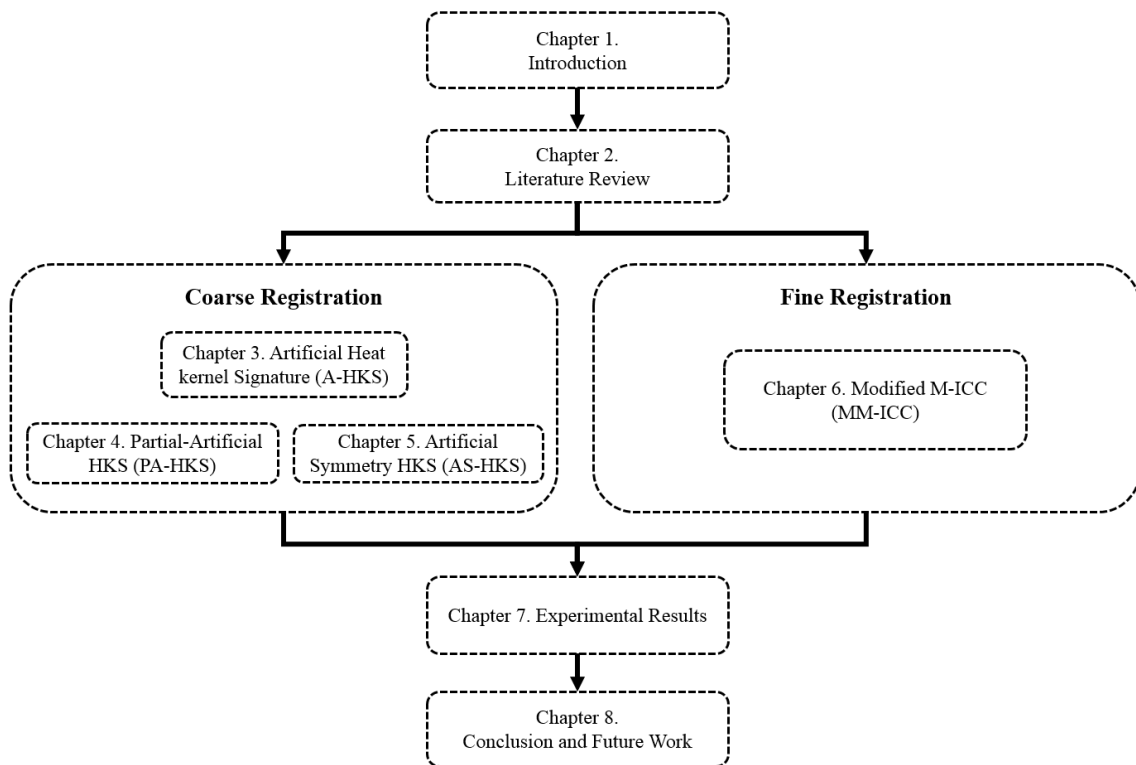
Figure 1.5: Outline of the Dissertation.

CHAPTER II

LITERATURE REVIEW

This present chapter aims to provide a detailed explanation regarding a number of previous research which has established the theoretical background and practical framework of the current dissertation research. Figure 2.1 gives an overview of this review of the literature. As clearly organized in Figure 2.1, the previous research has been categorized into two main types in 3D registration: the direct (appearance-based) registration and the feature-based registration. The former type involves three subcategories such as the Iterative Closest Point (ICP) [48], the Coherence Point Drift (CPD) [53, 54], and the Multi-view Iterative Closest Contour (M-ICC) [52] whereas the latter category includes the Heat Kernel Signature (HKS) [5], the Scale-invariant Feature Transform (3D-SIFT) [55], and the 3D-Harris [56]. As highlighted in Figure 2.1, this dissertation research proposes a new algorithm on the basis of the combination of the two algorithms from each category, the M-ICC algorithm and the HKS algorithm. The M-ICC, one of the direct registration methods, is the registration algorithm using corresponding contour points from the different views. This algorithm requires initialization of the range scan by pre-defined camera configuration. The HKS algorithm, one of the feature-based registration methods, is based on the concept of heat diffusion over the surface. In this algorithm, an interest point is selected if it remains as a local maximum of the geometry energy function; hence, it is challenging to identify the correct features in the partial object surfaces under self-occlusion. The present study begins with these limited features and aims to overcome through the combined algorithm of the two.
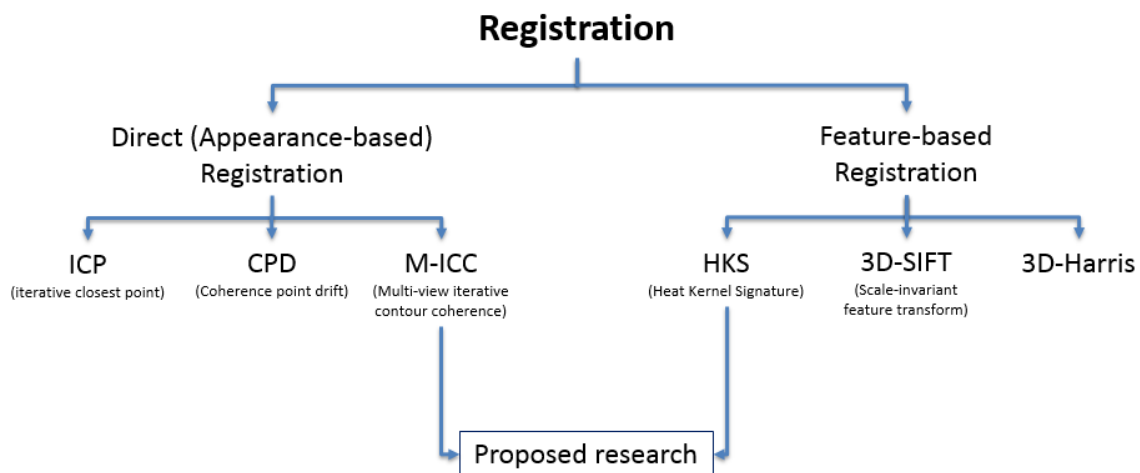
Figure 2.1: Taxonomy of Registration algorithms and Its relationship with our research.

Each registration algorithm in Figure 2.1 will be developed in more detail in the following sections. In addition, this literature review will also provide more information about some recent approaches in 3D reconstruction and clearly elucidate their achievement and the research challenges that still remain.

2.1   Direct (Appearance-based) Registration

The direct (appearance-based) registration refers to the process of identifying spatial transformation that aligns two point sets. Detecting such transformation aims to merge multiple data sets into a globally consistent model and also to plot new measurement to a known data set as an attempt to identify features or to estimate its pose. This direct alignment method is capable of performing the alignment of 2D and 3D points. Although this method requires good initialization in case of strong deformation, it still shows the effectiveness in avoiding being trapped in local extrema.

2.1.1 Iterative Closest Points (ICP)

One of the most widespread methods is the Iterative Closest Point (ICP) algorithm which was originally developed by Besl and McKay [48]. The ICP algorithm entails in-advance approximation to make convergence to a global minimum and this convergence to global minimum is not always secured especially in the setting where there is significant overlap. This algorithm aims to minimize the differences between two clouds of points. It is frequently employed to reconstruct 2D or 3D surfaces from different scan data, to make localization of robots, and also to achieve optical path planning, and so on. This algorithm iteratively performs revisions of the combination of translation and rotation, which is required to minimize an error metric, a distance from the source to the reference point cloud. It has become one of the widely adopted algorithms to operate the alignment of 3D models when an initial guess of the rigid target transformation is provided. There also have been a variety of studies derived from this ICP. [6, 57–59]

2.1.2 Trimmed ICP

The Trimmed ICP (TrICP) [59] has been presented as an extension of the well-known ICP algorithm aiming to provide natural, simple and more robust research outcomes. This newly proposed algorithm is grounded on the consistent use of the Least Trimmed Squares (LTS) approach in all the operation procedures. The TrICP algorithm is proven to be fast and highly applicable to the setting with overlaps under 50%, and further to be robust in case of incorrect measurement and shape defects. Moreover, it is simple and straightforward to set up parameters. The ICP is considered as one particular case of the TrICP where the overlap parameter is 100%.

2.1.3 Coherence Point Drift (CPD)

The Coherence Point Drift (CPD) algorithm [53,54], another well-known and widely employed 3D registration technique, is highly applicable to both rigid and non-rigid set registration. This CPD algorithm refers to the alignment of two point sets as a probability density estimation problem. It applies the Gaussian Mixture Model (GMM) [60] centroids which represents the first point sent to the second point set by maximizing the probability. These centroids are forcefully moved as a coherence group to reserve the topological framework of the point sets. The CPD algorithm is a fast algorithm that is able to reduce the complexity of the method computation to linear. It has been tested and validated both for rigid and non-rigid transformation even in case of noise, outliers, and missing points; and the results have successfully proven its effectiveness with its outperformance over the concurrent popular registration algorithms.

2.1.4 Multi-View Iterative Closest Contour(M-ICC)

Wang [52] proposed a wide baseline 3D modeling algorithm, named the Modified-ICC (M-ICC). This M-ICC algorithm operates the registration of the multi-view range scans through maximizing contour coherence between the observed and predicted contours across the multiple views. Based on the fact that the contour is considered as a rich source of geometric information for motion estimation and 3D reconstruction, the observed contours which are extracted from the original 2.5D range scan data is not be able to match the corresponding predicted contours which are derived from the projected 2.5D range scans. Accordingly, this algorithm iteratively establishes robust correspondences among apparent contours and minimize the distances in order to maximize the contour coherence. Nevertheless, the observed and predicted contours extracted entail false contour points mainly due to self-occlusion. This results in a main research challenge: how to eliminate the false contour points and how to

preserve exclusively the corresponding contour points. The key idea of this algorithm is to utilize two-step pruning to remove incorrect contour points; as a results, it provides complete reconstruction of the rigid and articulated objects using at least four frames.

Including the three major registration algorithms introduced above, a great deal of research has been conducted on the point set registration with a focus on where most pixels agree. Among many studies, the classic Iterative Closest Point (ICP) algorithm [48] and its variant [61] suggest the prosperous methodological technique to register the points and to reconstruct the model in a stable and effective manner. However, the ICP algorithm has shown some limitations; it requires good initialization and it is also time consuming mainly because this algorithm must include the process to identify the closest point pairs. The Coherence Point Drift (CPD) algorithm, which is another well-known method of the point set registration, and the modified CPD algorithms [62, 63] as well enable us to obtain more robust and stable outcomes despite of noise and outliers. The CPD algorithm is capable of producing highly robust results both in the rigid and non-rigid point sets. However, similar to the ICP algorithm, the CPD also requires good initialization to find correct correspondences. Another popular algorithm under the direct registration, the M-ICC algorithm in [52] aims to perform registration on the basis of the multi-view contour coherence. These algorithms briefly introduced above have confirmed to be effective and accurate under the reasonable initialization. However, successfully attaining accurate and robust registration without initialization still remain as a major challenge in the point set registration.

2.2 Feature-based Registration

The feature-based registration methods aim to identify corresponding features in the multiple data sets of different views and also to provide an effective and successfully

matching process of the extracted features across views. It is a fairly recent research trend that places an emphasis on detecting interest points in the 3D mesh models. Most research based on this feature-based registration focuses on the local surface descriptors [64, 65]. A multi-scale approach is commonly adopted to analyze the 3D surface at consecutive scales in order to find interest points at different levels [66]. A 3D extension of the 2D Harris operator is also proposed, which is grounded on the local autocorrelation of images [67, 68]. The studies in [68, 69] utilize the Heat Kernel Signature (HKS) of the 3D mesh model. On the basis of the geometry energy on the vertices, an interest point is selectively identified when it remains as a local maximum of the geometry energy function within several successive scales. The distinctiveness of an interest point is highly crucial for a stable outcome.

2.2.1 3D-SIFT (Scale-Invariant Feature Transform)

The 3D-Sift registration algorithm [55] refers to formulation of the 3D salient local features on the basis of the voxel grid under the framework of the Scale Invariant Feature Transform (SIFT). This algorithm identifies the outstanding keypoints, invariant points, on the 3D voxelized model and calculates invariant 3D local feature descriptors at these keypoints detected, as an attempt to represent the 3D model for shape retrieval. It is an advantageous technique for the rigid and articulated 3D models. The main contribution of this algorithm is its capability to create 3D salient feature implementation exclusively for the 3D models. Accordingly, the outstanding keypoints are able to locate only on the surface and completely 3D orientation normalization is guaranteed.

2.2.2 3D-Harris

The 3D-Harris operator [56] refers to the 3D extension of the 2D corner detection technique of Harris and Stephens [70]. This registration algorithm is grounded on the

first order derivatives following two orthogonal directions on the 3D surface. Recent technological advancement allows a great deal of 3D data and capture devices providing multimedia data at low cost; accordingly, how to choose relevant information has become a more and more important research topic. In the research fields of object registration, retrieval, and mesh simplification, it is crucial to detect a few salient structures, instead of the whole 3D object. This 3D-Harris registration algorithm presents an interest points detector for 3D objects on the basis of the Harris operator that has proven its effectiveness in computer vision applications. This algorithm is an adaptive technique to define the neighborhood of a vertex based on the Harris response calculated on that particular vertex. It has proven to be highly robust in transformations with the high repeatability values from the SHREC feature [71] detection and description benchmark, even in comparison to the recent technique such as the Heat Kernel Signatures, which will be fully discussed in Chapter 3.

Both of the two categories of point set registration reviewed above have involved their own strengths and weaknesses. Therefore, a number of attempts have been made to modify and/or combine different registration methodologies in order to alleviate the constraints and to obtaion more robust and accurate outcomes [69].

2.3   Recent Research on 3D reconstruction

This section provides further explanations on more recent research in the field of 3D registration and reconstruction on the basis of the classical registration algorithms discussed above. Three recent studies [12, 44, 46, 72, 73] will be introduced in this section.

2.3.1   KinectFusion

The KinectFusion allows a user to hold and move a standard Kinect camera as an attempt to promptly generate the detailed 3D reconstructions. The depth data from

Kinect is employed to detect the 3D pose of the sensor and also to reconstruct the 3D models of the physical scene with precise geometrical information in real-time [44, 46].

2.3.2 RGB-D Mapping

A RGB-D camera refers to the novel sensing system that is able to capture RGB images along with per-pixel depth information. This research examines how to successfully employ RGB-D cameras in the context of robotics; it focuses mainly on building dense 3D maps of indoor environments. The 3D maps created have advantageous applications in various fields, including robot navigation, manipulation, semantic mapping, and telepresence. The RGB-D mapping is a full 3D mapping algorithm using novel joint optimization which combines visual features and shape-based alignment. Additionally, in order to generate globally consistent maps, this algorithm also combines visual and depth information mainly for view-based loop closure detection [12].

2.3.3 Real-time Visual and Point Cloud SLAM

With an advent of affordable RGB-D cameras such as Microsoft Kinect, there has been a great improvement in VSLAM applications [72, 73], 3D object modeling and reconstruction by utilizing dense, synchronized depth and color images. On the basis of the needs for both fast and accurate algorithms in real-time registration to exploit the high frame rate of these devices, this research introduces a new technique that is capable of performing the generalized ICP on two frames in typical times of 10 minutes. This technique employs an efficient bundle-adjustment framework to combine ICP with visual feature matches both for frame-frame matching and overall global adjustment.

2.4 Challenges and Research Needs

In this chapter, a number of studies and registration algorithms have been introduced and discussed. The major drawback to the approaches discussed previously is that successful 3D reconstruction is exclusively available in the viewable areas. The previous approaches and algorithms on wide baselines aim to perform alignment of point clouds which are generated from largely varying views. Although the observation point of view is different, it is still possible to calculate and match a set of features in each view. It is mainly because there exist enough overlaps between two different data sets. Table 2.1 illustrates the amount of overlaps from the previous research on 3D reconstruction [12, 44, 52, 73–79]. As shown, the majority of the previous studies require enough amount of overlaps in order to successfully identify correspondences of the features and to obtain better outcomes. In other words, it is compulsory to include a good number of input data. This results in one of the major limitations in the registration algorithm based on wide baselines; accordingly, a research need has arisen to address this challenge. Further it triggers the present dissertation research where an attempt is made to successfully generate robust 3D reconstruction even in the setting with extremely low overlaps of approximately 5-10 percentages.

Authors	Title	Overlap
Shaharam Izadi et al.	KinectFusion: Reak-time 3D reconstruction and Using a Moving Depth Camera [44]	80-90%
Michael Ying Yang et al.	Robust Wide Baseline Scene Alignment Based on 3D Viewpoint Normalization [74]	50-70%
Hao Du et al.	Interative 3D Modeling of Indoor Environments with a Consumer Depth Camera [75]	80-90%
Nicola fioraio et al.	Realtime Visual And Point cloud SLAM [73]	80-90%
Yiben Liu et al.	A Point-Cloud-Based Multiview Stereo Algorithm for Free-Viewpoint Video [76]	50-70%
Peter Henry et al.	RGB-D Mapping: Using Depth Cameras for Dense 3D Modleing of Indoor Environments [12]	80-90%
Christoph Strca et al.	Dense matching of multiple wide-baseline views [77]	50-70%
Richard Newconbe et al.	Live Dense Reconstruction with a Single Moving Camera [78]	80-90%
Ruizhe Wang et al.	3D Modeling from Wide Baseline Range Scans using Contour Coherence [52]	40-60%
Todor Stoyanov et al.	Fast and accurate scan registration through minimization of the distance between compact 3D NDT repesentatoins [79]	80-90%

Table 2.1: Inferred Amount of Required Minimum Overlap from Related Works

CHAPTER III

Heat Kernel Signature

The current registration algorithm is proposed on the basis of the Heat Kernel Signature algorithm (HKS) [5]. This shape descriptor is derived from the heat kernel, which is a fundamental solution to heat equation (diffusion equation). Therefore, this chapter will provide a brief description on the heat kernel and the HKS; then, it will also demonstrate how the HKS has been adapted for registration of the multiple incomplete mesh models.

3.1 Heat operator and Heat kernel

Heat equation is the essential equation in the study of thermal conductivity and diffusion. It is a partial differential equation which illustrates the distribution of heat or temperature in space over a certain period of time, t. Let us suppose that there is a compact Riemannian manifold, M which could possibly be with boundary. In this assumption, heat diffusion process over M is governed by heat equation,

$$\Delta u(x,t) = -\frac{\partial u(x,t)}{\partial t}, \tag{3.1}$$

where $u(x,t)$ denotes the amount of heat on the surface at a point $x \in M$ in time t, and Δ defines the positive semi-definite $Laplace - Beltrami\ operator$. In case of initial heat function $f : M \rightarrow \mathbb{R}$, and heat operator H_t, the heat operator applied to f provides the heat distribution at time t , $H_t f$. And the $H_t f$ fulfills heat equation for all t and in initial heat distribution, $H_t f = f$. And the solution of heat equation

takes the form for any M,

$$H_t f(x) = \int_M \mathbf{k}_t(x,y) f(y) d_y, \tag{3.2}$$

where d_y is a volume form at $y \in M$ and $\mathbf{k}_t(x,y)$ is identified as *heat kernel* function. In other words, heat kernel, $\mathbf{k}_t(x,y)$ denotes the amount of heat that is transferred from x to y in time t, in case of a unit heat source at x.

For the compact Riemannian manifold M, heat kernel function can be illustrated as

$$\mathbf{k}_t(x,y) = \sum_{i=0}^{\infty} e^{-t\lambda_i} \phi_i(x)\phi_i(y), \tag{3.3}$$

where λ_i and ϕ_i are i^{th} eigenvalue and corresponding eigenfunction of Δ, Laplace-Beltrami operator satisfying $\Delta\phi_i = \lambda_i\phi_i$ Heat kernel function has been well-known for advantageous properties as described in detail in [5]. The essential properties of heat kernel are, in general, threefold: intrinsic property, informative property, and multi scale property, all of which are crucial requirements as an ideal feature descriptor. First, the intrinsic property claims that hear kernel has invariability under isometric transformation mainly because that the Laplacian can be presented in local coordinates as a metric function. Therefore, in case that a Riemannian manifold is undergoing isometric deformation, heat kernel of corresponding points on the pre-deformation manifold is the same as the one on the post-deformation manifold. One of the practical implications of this particular property is that heat kernel can possibly be utilized to investigate the shapes which are undergoing isometric deformations. This property entails the effectiveness in matching articulated shapes, including humans or animals in different poses. Secondly, the informative property implies that heat kernel involves all the information regarding the intrinsic geometry of a Riemannian manifold M; then, it is, accordingly, possible to have full characterization of the shape of M up to isometry. This property represents a basic consequence of the

below equation as in [80],

$$\lim_{t \to 0} t \log \mathbf{k}_t(x, y) = -\frac{1}{4} d^2(x, y), \tag{3.4}$$

where $d(x, y)$ is geodesic distance between points x and y. If both pre-and post-deformation manifolds show identical geodesic distance between all pairs of corresponding points, the two manifolds contain the same intrinsic shape. Last, heat kernel is capable of characterizing local shapes depending on the choice of scale parameter t. The multi-scale property of heat kernel, in the framework of point signatures, involves that in case of small values of t, small neighborhoods of x mainly determine function $\mathbf{k}_t(x, \cdot)$, and the neighborhoods build up bigger as t increase. This property indicates that given small t, $\mathbf{k}_t(x, \cdot)$ simply reflects local properties of the shape around x, whereas given large values of t, $\mathbf{k}_t(x, \cdot)$ identifies the global structure of M from the point of view of x.

3.2   Heat Kernel Signature (HKS)

The HKS is established on the basis of heat kernel, which is stable regardless of perturbation of the shape and also entails advantageous properties as above explained. These features have made heat kernel highly beneficial to point feature signature. Nonetheless, high computational complexity is the main flaw of using family of functions $\{\mathbf{k}_t(x, \cdot)\}_{t>0}$ to characterize point x. In case of each point on M, heat kernel $\{\mathbf{k}_t(x, \cdot)\}_{t>0}$ is identified based on the product of temporal and spatial domain $\mathbb{R}^+ \times M$. Accordingly, full heat kernel of all the points on M also entails $\mathbb{R}^+ \times M \times M$ space, in addition to the cost of matching the neighbors when comparing heat kernels of two points. Full heat kernel involves a number of superfluous information; and in the spatial domain, the alteration of heat kernel function is demonstrated according to the change in time. In an attempt to overcome this challenge, it has been proposed to reduce the dimensionality particularly to temporal domain and to limit heat kernel to

26

its subset. Afterward, the HKS meets the requirements above, as suggested in [5]. In case of a point x on the manifold M, its Heat Kernel Signature, $HKS(x)$, is identified as a function over the temporal domain:

$$HKS_t(x) = \mathbf{k}_t(x, x) = \sum_{i=0}^{\infty} exp^{\lambda_i t} \phi_i(x)^2, \tag{3.5}$$

where λ_i and ϕ_i are i^{th} eigenvalue and eigenfunction of Laplace-Beltrami operator. As evidenced in detail in [5], with no regard to limiting signature to the temporal domain and dropping the entire spatial domain, $\{\mathbf{k}_t(x, x)\}_{t>0}$ keeps all of the information of $\{\mathbf{k}_t(x, \cdot)\}_{t>0}$ in the condition of mild assumptions.

As illustrated in Figure 3.1, the HKS allows us to perform multi-scale matching between points by comparing their signatures at different time intervals [5].
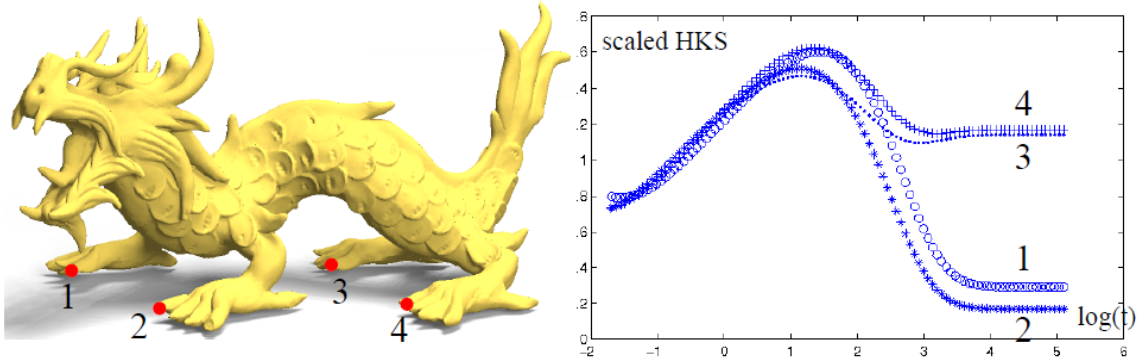
Figure 3.1: Left: Fully closed 3D dragon model; Right: Scaled HKS at points 1, 2, 3, and 4. All four signatures are closed at the small t's while the big t's separate the points on the front claws from those on back [5].

3.3   Relation of HKS to Curvature

It is widely accepted that as $t \to 0$, there is an asymptotic expansion of the HKS function at every point $x \in M$ of the form:

$$HKS_t(x) = \mathbf{k}_t(x, x) = (4\pi t)^{-d/2} \sum_{i=0}^{\infty} a_i t^i, \tag{3.6}$$

27

where $a_0 = 1$ and $a_1 = \frac{1}{6}s(x)$ with $s(x)$ being scalar curvature at point x. Heat has a tendency to diffuse slower at points with positive curvature and faster with negative curvature. This feature leads us to the point that Heat kernel signature function $\mathbf{k}_t(x,x)$ can be elucidated as intrinsic curvature at x at scale t.

$HKS(x,t)$ is closely related to the local curvature of region around point x. Figure 3.2 illustrates the values of heat kernel function $\mathbf{k}_t(x,x)$, in case of small fixed t given, on the models of the hand, Homer, and trim-star. The function values are mapped from a blue color for the lowest to a red color for the highest on the three models, respectively.
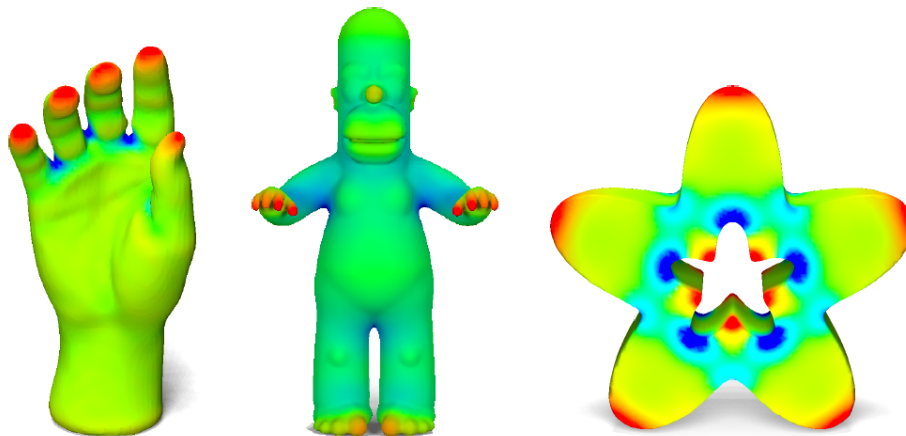
Figure 3.2: Heat kernel function $\mathbf{k}_t(x,x)$ for small fixed t on the hand, homer and trim-star models [5].

The present algorithm uses heat diffusion on the surface of a full 3D model in order to detect and identify highly local shape features. Heat diffusion over a longer period of time enables us to recognize the summaries of a shape in large neighborhoods whereas heat diffusion with a short time period is capable of identifying detailed local shape features. Consequently, through heat diffusion, it is highly possible to compare point signatures at different time intervals and to successfully accomplish multi-scale matching between points.

3.4 Artificial Heat Kernel Signature (A-HKS)

This chapter discusses the methodological approach to transform an incomplete mesh mode from the depth camera, which entails merely visible surfaces of the target in the depth camera direction, and to create a complete mesh model. It is worth noting that in case of the incomplete mesh model which is derived from the direction between a depth camera and the target, it is challenging to obtain significant features using HKS. The main reason of this difficulty is that the HKS algorithm operates on the basis of the curvature with neighboring points of the surface over time, t; hence, it becomes problematic to identify correct feature descriptors in the partial object surfaces under self-occlusion, which involves some missing areas. In an attempt to address this challenge, it is important to fill up and recover invisible areas with the artificial mesh. The more similarity to the original target the artificial mesh area shows, the higher accuracy can be found in the feature point descriptors; Further, it is possible to attain highly accurate registration outcomes. Figure 3.3 illustrates the idea of the registration based on A-HKS. Red dots indicate the corresponding features from the multiple partial mesh. As shown, the corresponding features extracted from the generated artificial mesh are capable of performing registration without pre-define calibration.

Incomplete Mesh Model

In order to create the complete mesh model from partial range scan data, the present algorithm proposes the following two different techniques: Partial Artificial HKS (PA-HKS) and Artificial Symmetry HKS (AS-HKA).

As in Figure 3.4, the first proposed technique, the PA-HKS, attempts to attain the artificial 3D mesh through projection. The 2.5D mesh data, which is derived from only visible surface depth data of the target, cannot entail fully closed surface mesh data. Therefore, the boundary of the extracted surface is unable to obtain neighboring
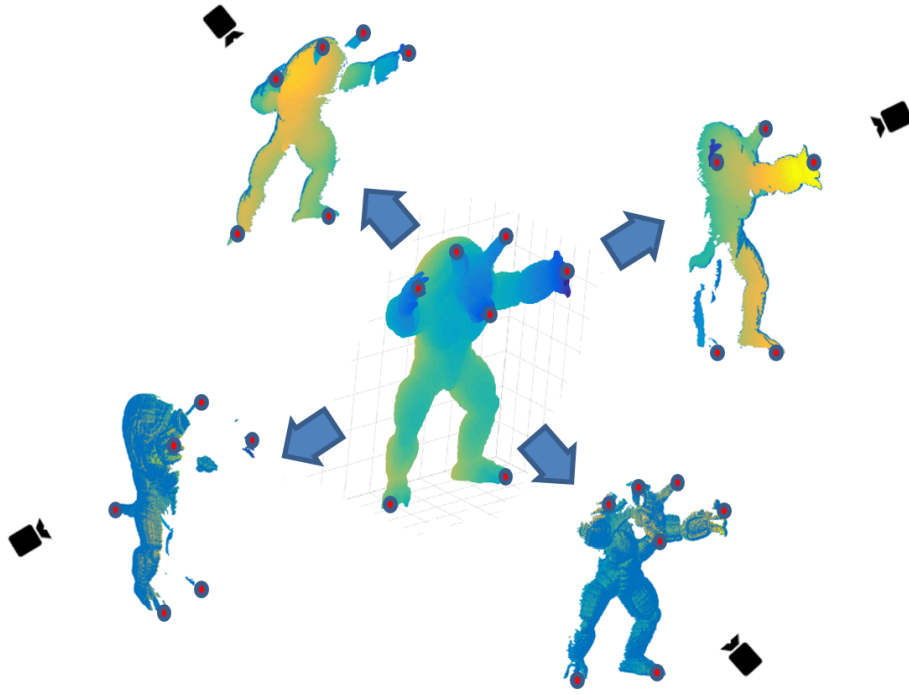
Figure 3.3: Idea of the A-HKS based Registration.

points; further, the boundary of these mesh points is unable to involve HKS which should be created through the curvature of neighboring points. In order to overcome this challenge, in the present algorithm, the range scan data is projected to the plane and the projected data is connected to the original range scan data using mesh. This newly generated closed mesh, which now entails a 3D volume, is utilized to apply the HKS algorithm to detect the feature descriptors. It is true that the generated artificial 3D mesh is only capable of capturing the partial geometric information from the 3D model; however, the extracted PA-HKS features are expected to preserve some global geometric characteristics and those characteristics enable us to successfully create fairly reliable alignment between the partial surface data from two adjacent views.

In the PA-HKS algorithm, coarse registration is performed on the basis of the global HKS descriptor over a longer period of time, which allows us to identify the summaries of the shape in large neighborhoods. Nonetheless, failures could be often found in detecting corresponding HKS keypoints mainly due to the difference of the

shapes between the artificial 3D mesh through projection and the original target. In other words, the visible surface meshes are directly extracted from the target and accordingly are the same as the original target; however, the meshes generated through projection represent invisible areas and boundaries and illustrate completely different surface curvatures.
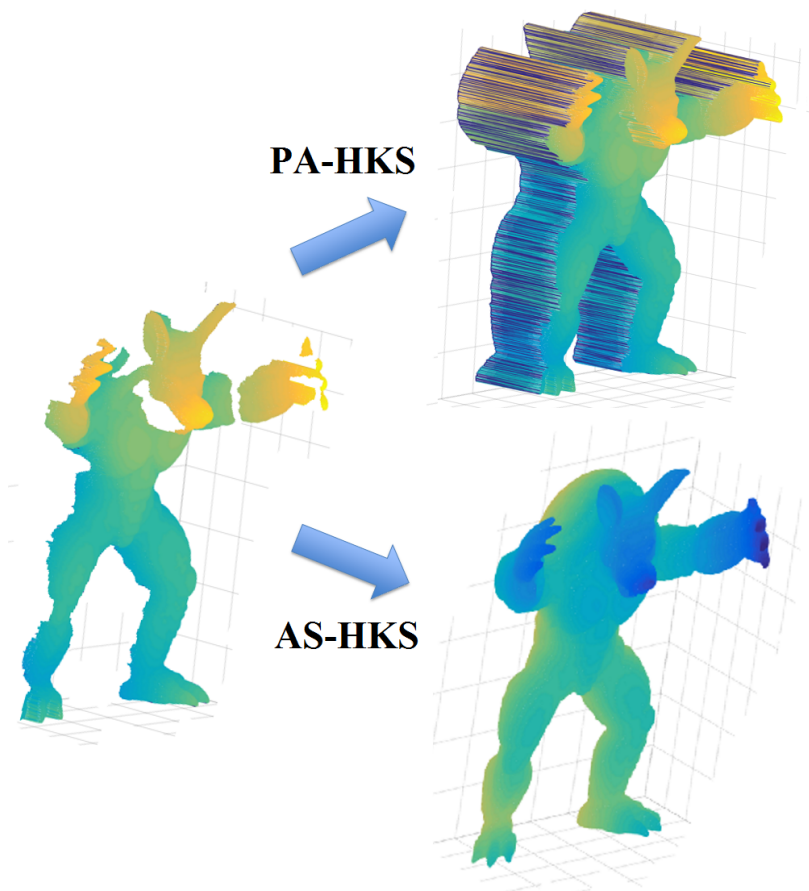
Figure 3.4: Left: 2.5D range scan mesh data; Right top: Partial artificial mesh by projection, as described in Chapter 4; Right bottom: Artificial symmetry volume mesh, as described in Chapter 5.

For obtaining accurate registration outcomes, both local and global KHS information is mandatorily required. Thus, in order to address this challenge, the second technique, the AS-HKS, is proposed on the basis of artificial symmetry 3D volume mesh, as shown in Figure 3.4. The fundamental concept of this technique is to gen-

erate artificial 3D mesh data with higher accuracy using an ellipsoid and a sphere. Based on the fact that solid objects which have a volume generally entail a rotational symmetry, one assumption is made that visible and invisible areas of the range scan data are symmetrical to each other according to a symmetry plane between the two. This assumption helps us to attain a symmetrical counterparts mesh on the basis of the visible area of the target to generate greatly accurate artificial 3D mesh. This generated artificial symmetry 3D mesh model is able to offer correct local and global HKS descriptors. Accordingly, it enables us to easily and correctly detect corresponding HKS feature points from the different multiple range scan data. As an attempt to generate artificial symmetry 3D volume mesh, the present algorithm employs 2D plane-distance and 3D depth-gap between two endpoints of cut mesh in four different angle directions. More detailed explanations in regard to the two techniques will be provided in Chapters 4 and 5.

CHAPTER IV

Coarse Registration based on PA-HKS

4.1 Proposed Approach

The present algorithm involves coarse registration through rough alignment of multiple partial overlapping range scans based on the partial artificial hear kernel signature (PA-HKS) which is extracted from each view. This PA-HKS algorithm is grounded on the heat kernel signature algorithm. As previously explained, the HKS algorithm is performed based on gradient of the surface; Therefore, it is not an easy process to identify the correct feature descriptor in the partial object surfaces with self-occlusion mainly because the partial object has an opened surface which has boundary and heat diffusion near the boundary doesn't exist. In order to address this research challenge, the range scan data is projected to the plane and connected to the original range data through mesh. This newly generated partial artificial 3D volume mesh is then employed to operate the PA-HKS algorithm to find the feature descriptor. It is true that the generated artificial 3D mesh is only able to capture partial geometric information from the 3D model; however, the extracted PA-HKS features are anticipated to preserve some geometric characteristics because the relatively reliable alignment can be produced between the partial surfaces which are observed from two adjacent views. This newly proposed algorithm consists of three steps; and the three steps will be discussed as follows: generating partial-artificial mesh, extracting PA-HKS from the generated artificial mesh, and alignment of multi-view range scan by matching the extracted PA-HKS.

4.1.1 Projection to the Back Plane

2.5D range scan R_i of frame i gives depth value $R_i(\mathbf{x})$ at each image pixel $\mathbf{x} = (x, y)^T \in \mathbb{R}^2$. In case of the pixels of an object in frame i as X_i given, the depth of pixels belonging to the background is fixed by infinite, $R_i(\mathbf{x}) = \infty$ for $\mathbf{x} \notin X_i$. In an attempt to generate the closed surface mesh, meshes are created on the opened surface area of the target through projecting range scan data.
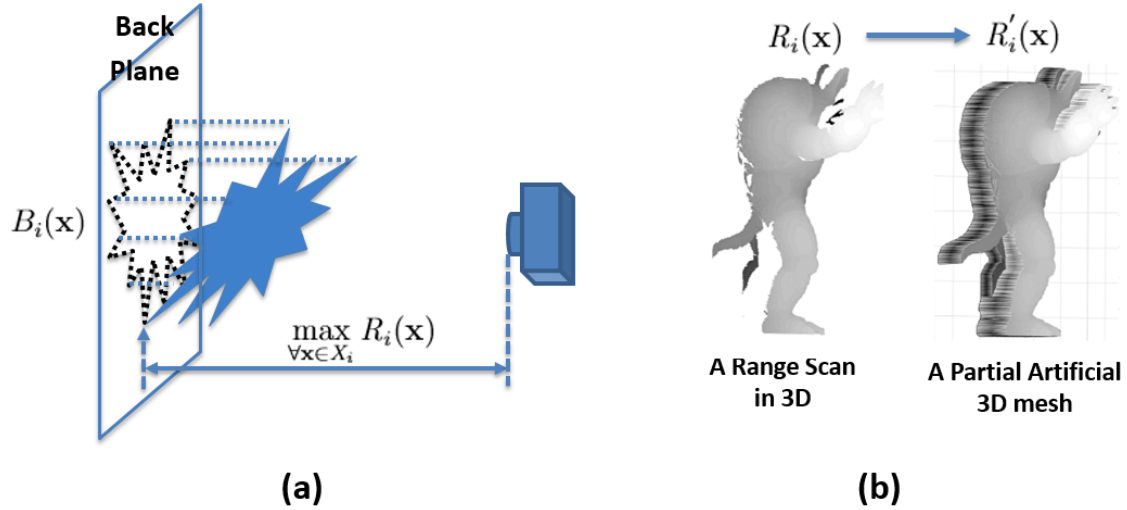
Figure 4.1: Illustration of Projection: (a) Projection to the back plane; (b) Generating partial closed mesh.

The projected vertices are B_i and entail the same location (x, y) pixels and different depth values in comparison to the original range scan data. Thus, the closing surface mesh can be used as the back area of the object.

$$B_i(\mathbf{x}) = \max_{\forall \mathbf{x} \in X_i} R_i(\mathbf{x}). \tag{4.1}$$

In Equation 4.1 and Figure 4.1(a), the maximum depth of the original range scan data determines the location of the back plane in the projection. Due to the fact that all surface points of the 3D volume object should have some degree of depth despite the uncertainty of volume thickness of the 3D object, the back plane should be positioned

with a consideration of maximum depth which is enough to have every single surface point, including the deepest depth point on the object surface, projected to the back plane.

$$R_i^{'}(\mathbf{x}) = B_i(\mathbf{x}) + R_i(\mathbf{x}). \tag{4.2}$$

After generating B_i, we update the range scan $R_i^{'}$ by combining partial range scan, R_i and the generated back-area range data, B_i as shown in Equation 4.2 and Figure 4.1(b). Afterward, a single constant camera calibration matrix K is used to transform points from the camera frame to the image plane. $V_i(\mathbf{x}) = K^{-1}R_i^{'}(\mathbf{x})\tilde{\mathbf{x}}$ can be represented as the back-projection operator which maps $\mathbf{x}$ in frame i to its 3D location, where $\tilde{\mathbf{x}}$ refers to homogeneous vector $\tilde{\mathbf{x}} = [\mathbf{x}^T|1]^T$.

As illustrated in Figure 4.2(a)-(b), partial artificial 3D mesh data is generated by projecting the range scan data to the back plane. The back and side planar surfaces of the artificial 3D mesh are added as an attempt to find PA-HKS keypoints on the frontal mesh surface which is visible in the original view.

4.1.2 Extracting, Shifting, and Grouping of PA-HKS keypoints

Some PA-HKS keypoints extracted are recognized along the contour between the back and the side surface; afterwards, these keypoints should be relocated to the front mesh surface primarily because only the original front range scan data is able to provide the correct location of the 3D space in order to identify the correspondence of the feature, as shown in Figure4.2(c).

As an attempt to guarantee one-to-one mapping across views, the keypoints are grouped through using their 3D geodesic distance [81–83] and the similarity of their PA-HKS signatures, as described in Figure 4.2(d). The geodesic distance between two points on the surface is determined according to the length of the shortest path which connects the two points. In this algorithm, it is computed between the extracted PA-HKS point p_1 and the other point p_2 constructing the surface on the basis of the
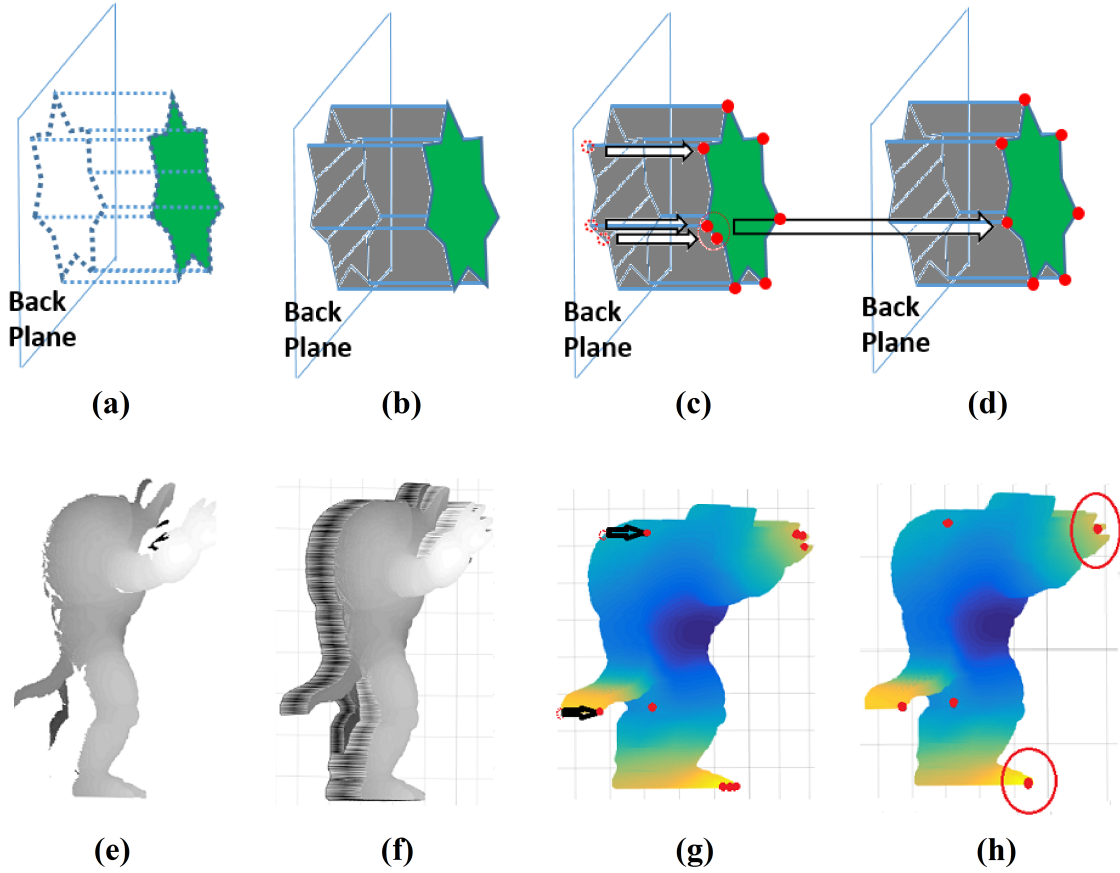
Figure 4.2: Illustration of PA-HKS: (a) Range scan in 3D (green); (b) Partial 3D mesh created from (a); (c) PA-HKS features after shifting; (d) PA-HKS features after grouping; (e)-(h) Real object examples corresponding to (a)-(d).

Jacobi iteration algorithm on the triangulated surface 3D range scan. The following equation describes how to approximate the geodesic distance δ_{p_1,p_2} between p_1 and p_2 [81–83]:

$$\delta_{p_1,p_2} = \min \gamma(\beta(p_1, p_2)), \tag{4.3}$$

where $\beta(p_1, p_2)$ is a path between p_1 and p_2 according to the surface, and $\gamma(\beta(p_1, p_2))$ is the shortest geodesic distance between two points along the surface. Therefore, a number of PA-HKS keypoints are located within a smaller length than η. These PA-HKS keypoints are grouped and relocated as one in the center of the PA-HKS

keypoints based on Euclidean space.

$$\tilde{p}_i(V_i(\mathbf{x})) = \frac{1}{n} \sum_{i=1}^{n} p_i(V_i(\mathbf{x})), \quad \text{if } \delta_p < \eta \tag{4.4}$$

where η is a threshold to determine grouping of the PA-HKS keypoints.

This leads to one single local PA-HKS keypoint in the area with high energy and rich geometric information. Despite the fact that the keypoints recognized may not entail the precise spatial information, they are still capable of providing the crucial 3D landmarks for initial point set alignment.

4.1.3 Matching of the PA-HKS Keypoints

Prior to the ICP-based alignment, the PA-HKS features are utilized to perform the initialization process of the correspondence between two adjacent views. Given two PA-HKS feature sets derived from two range scans as $\mathbf{S}$ and $\mathbf{T}$, the correspondence pairs across two views can be recognized by

$$\mathbf{t}_s = \arg \min_{\mathbf{t} \in \mathbf{T}} d(\mathbf{t}, \mathbf{s}), \ \forall \mathbf{s} \in \mathbf{S}, \tag{4.5}$$

where $d(\cdot)$ is distance function between two PA-HKS features. As an attempt to assure more robust feature matching outcomes, in case that $d(\mathbf{s}', \mathbf{t}_{s'})$ has a larger value than a threshold, it is declared that $\mathbf{s}' \in \mathbf{S}$ does not involve a correspondence in $\mathbf{T}$ and accordingly will not be included in the following ICP step. As followed by the initialization of the correspondences through PA-HKS, the ICP is used in order to identify initial transformation between two scans.

4.2 Experimental Results

The coarse registration algorithm based on the PA-HKS is evaluated by the degree of decrease in rotation and translation error. In the evaluation process, four input range scans of the 3D model, Armadillo from the Standard 3D model dataset [84]

are adopted and tested approximately at 90^0 apart; and two different settings, with limited overlap and without any initialization, are further designed to verify the effectiveness of the proposed algorithm, as in Figure 4.3.
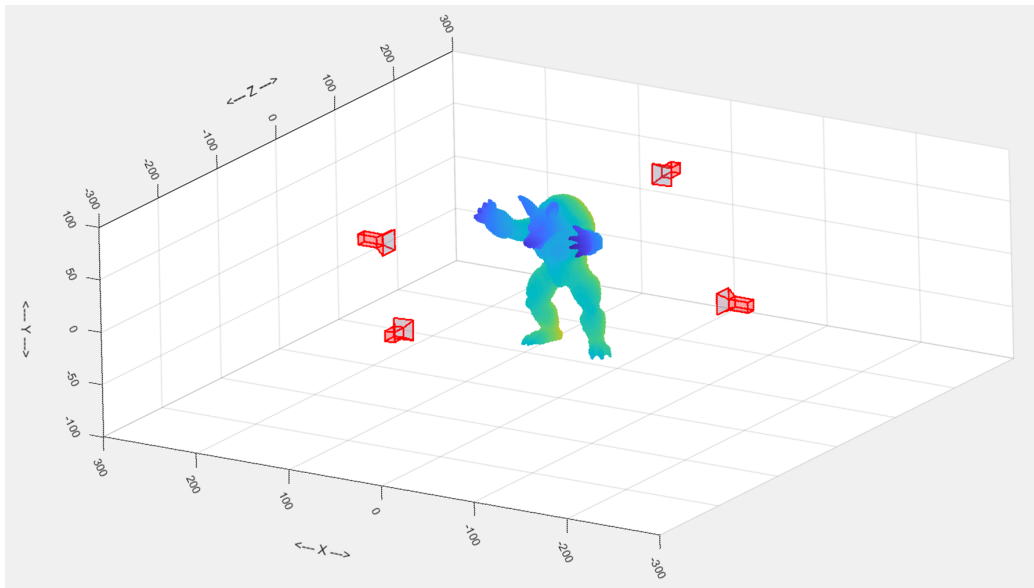
Figure 4.3: Experimental setting in a world coordinate.

The depth cameras keep the distance from the center of the target object by 200, and resolution of the depth camera is set to 640X480 pixels. And the target occupied a 3D volume approximately with a size of 120X150X110. Two separate criteria are considered in order to assess the effectiveness of the proposed algorithm. First, the numerical errors in the difference of rotation angles and translation is examined to evaluate the degree of transformation in comparison with ground truths. Secondly, the visibility information is also checked.

4.2.1 Numerical Results based on Transformation

Table 4.1 clearly verifies the efficiency of the current coarse registration based on the PA-HKS with numerical outcomes. Transformation by the PA-HKS is estimated and then compared with ground truth values in order to assess accuracy of the proposed PA-HKS algorithm. This estimation process of registration is set with no

initialization. As shown in the table, mostly, the estimation results of rotation are approximately $10° \sim 20°$ in Roll, Pitch, and Yaw rotation and translation errors are less than about 50.

			Rotation Angle Gap			**Translation** Gap		
			Roll	Pitch	Yaw	X	Y	Z
Case 1	Overlap	Ground truth	2.07°	1.93°	88.00°	196	3	-203
(V_1, V_2)	15.11%	PA-HKS	4.45°	11.50°	99.30°	190.4	5.5	-226.4
Error of PA-HKS			**2.38°**	**9.57°**	**11.30°**	**5.6**	**2.5**	**23.4**
Case 2	Overlap	Ground truth	4.57°	4.49°	$-174.4°$	-5	2	-402
(V_1, V_3)	29.80%	PA-HKS	$-6.22°$	10.16°	$-187.2°$	39.6	28.7	-392.6
Error of PA-HKS			**10.79°**	**5.67°**	**12.83°**	**44.6**	**26.7**	**9.4**
Case 3	Overlap	Ground truth	$-1.78°$	2.20°	$-96.00°$	-197	2	-195
(V_1, V_4)	27.89%	PA-HKS	6.25°	$-3.28°$	$-76.77°$	-182.7	-7.2	-165.4
Error of PA-HKS			**8.03°**	**5.48°**	**19.23°**	**14.3**	**9.2**	**29.6**

Table 4.1: Results of Coarse registration by PA-HKS in comparison to ground truth.

4.2.2 Visual Results of Coarse Registration

In order to further verify the effectiveness of the proposed algorithm, four different range scans, which are extracted from the 3D Stanford armadillo model, are utilized and the results are compared with the ones from the previous M-ICC algorithm. Figure 4.4 demonstrates this visual representation of the outcomes. In Figure 4.4 (a), the four range scans are visualized all together in the 3D space with no initialization. All four range scan are set to face the same camera direction under the unknown initialization setting. Figure 4.4 (b) illustrates the corresponding features generated by the proposed PA-HKS algorithm. The PA-HKS algorithm extracts corresponding features out of the partially overlapped range scan data by applying the heat kernel
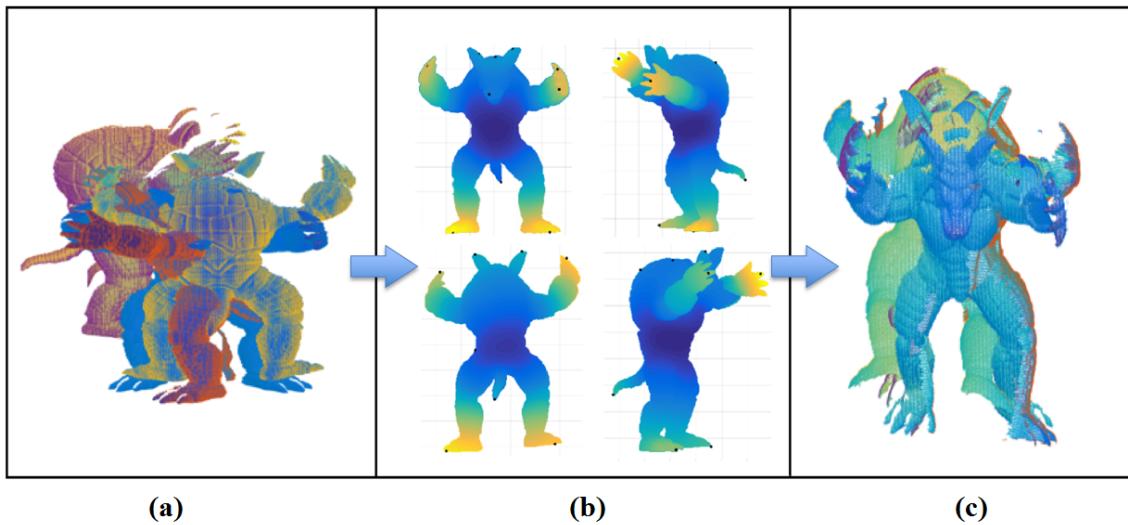
Figure 4.4: (a) Initial position of 4 range scans of Armadillo in camera coordinate; (b) PA-HKS features extracted from of 4 range scans (black dots); (c) Result of the PA-HKS based coarse registration.

signature (HKS) descriptor. Heat distribution is indicated using different colors of the surface. As shown in the figure, the warm colors around the PA-HKS features indicate high variance of local geometry; Accordingly, the similar distribution of the feature points in the multi-view scans indicates their consistency and reliability. As represented in Figure 4.4 (c), initial alignment results clearly validate the effectiveness of the PA-HKS in coarse registration.

4.3   Discussion

A new and robust 3D modeling algorithm has been proposed to perform coarse registration on multi-view range scan data with no initial condition given. To be more specific, the PA-HKS features which are derived from the partial artificial mesh models play a crucial role to perform rough alignment of the range scan data despite of large view gaps and complex object contours. The present algorithm, the PA-HKS coarse registration, provides a more robust and flexible technique to deal with

multi-view camera settings and 3D objects with complex shapes. This algorithm is proposed as a preliminary step before the MM-ICC, which will be introduced in detail in Chapter 6, in order to perform fully automatic registration.

CHAPTER V

Coarse Registration based on AS-HKS

5.1   Abstract

In the previous chapter, we introduced the first attempt to coarse registration using the PA-HKS. Although it allows us to generate a 3D model with higher accuracy in comparison with the recent research, this projection-based algorithm has a limitation in identifying the accurate matching model in huge different perspective range scan data. Due to the fact that mesh is created through projection, a visible surface mesh presents consistency to the original target but a surface mesh in invisible areas shows a big difference and the volume of each part of the target cannot entail accurate thickness. It is impossible that the incorrectly extracted HKS descriptors attain enough information to find corresponding features. The present paper begins with this limitation and attempts to solve it. This algorithm, the AS-HKS proposes Artificial Symmetry Volume Completion (matching) for 3D modeling to consider combination of local and global descriptors based on the Artificial Symmetry Volume meshes. This new coarse registration, the AS-HKS algorithm can provide successful outcomes of registration for extremely overlapping data as an indispensable factor. The coarsely aligned results from this powerful coarse registration algorithm is matched by the MM-ICC method in the fine registration step. The results are successful even in case of 1-2% overlapping areas, whereas previous studies require at least 45-50% [31,47,48] of overlapping regions.

5.2   Introduction

5.3   Proposed Approach

The proposed AS-HKS algorithm, which is grounded on the Artificial Symmetry Volume Completion for 3D modeling, aims for robust registration of multiple and complex range scan data with completely no initialization. The main concept of this algorithm is using a symmetrical counterpart to generate partial artificial symmetry volume 3D meshes with high accuracy. These symmetrically recreated 3D meshes allow us to precisely locate both local and global HKS descriptors. The combination of local and global HKS descriptors plays a crucial role to successfully find corresponding HKS feature points from multiple views. The proposed algorithm consists of the following three steps: generating artificial symmetry 3D volume mesh by detecting a proper thickness of the volume of the target using two criteria, identifying the AS-HKS descriptors which can provide both local and global information and refinement of the extracted features, and finally coarse initial registration of 3 HKS keypoints using HKS descriptors.

5.3.1   Artificial Symmetry 3D Volume Mesh

In the previous PA-HKS, the partial artificial 3D mesh is proposed using projection. Initial registration of the previous algorithm is performed based on the global HKS descriptor over a longer period of time, which enables us to spot the summaries of the shape in large neighborhoods. However, it often fails to correctly find corresponding HKS keypoints mainly because the artificial 3D meshes through projection show a big difference in shape from the original target. In other words, the visible surface meshes, which are directly extracted from the target, are the same as the original target; however, the generated meshes by projection to represent invisible areas and boundaries entail totally different surface curvature. It is true that HKS descriptors of
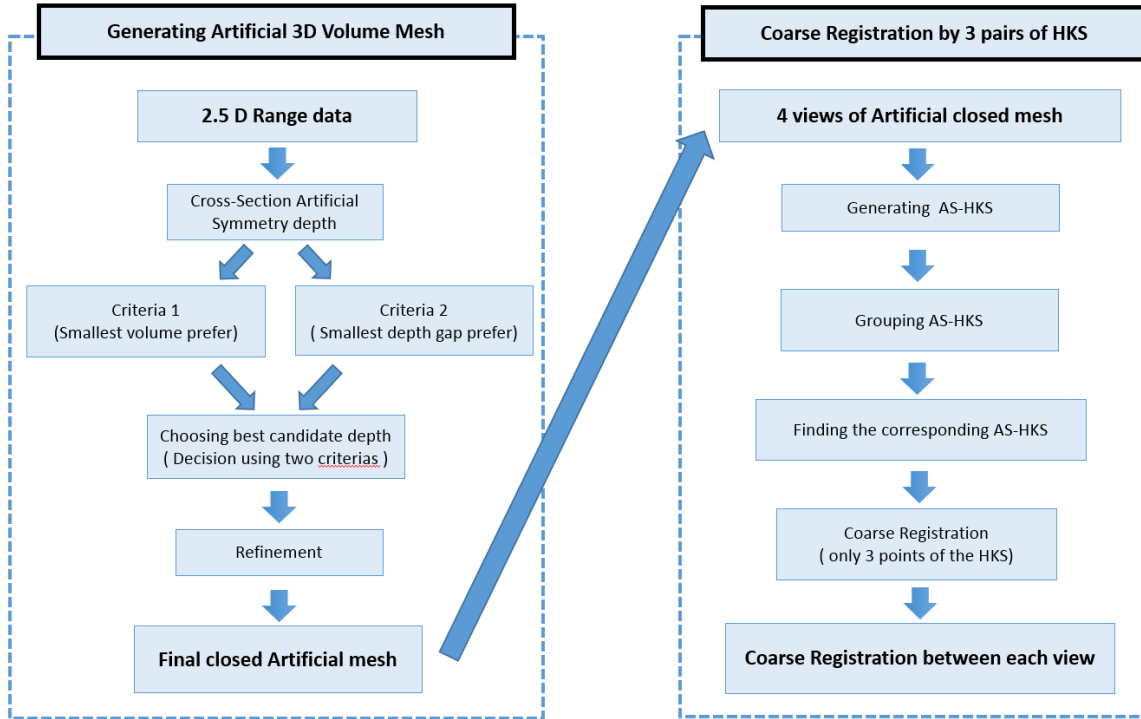
Figure 5.1: Flow chart of the AS-HKS steps.

the projection-based method are globally meaningful features to detect corresponding feature points among scan data from different views; however, it fails to perform successful detection locally. In order to obtain accurate registration outcomes, both local and global HKS information is highly required. To address this challenge, we propose the artificial symmetry 3D volume mesh.

Figure 5.2 illustrates the basic idea on how to generate an artificial symmetry volume from the 2.5D range scan data. Figure 5.2 (a) refers to an anatomical plane which is a hypothetical plane used to transect the human body [85]. In the blue (coronal) plane, the front area is visible whereas the back area is invisible from the camera when the camera is located in front of the target. The green (axial) plane provides the shape of the cross section of the human body, where we can check the shape of the cross section of the body has a symmetry volume between the visible and invisible areas. Therefore, it is attempted to generate the invisible area which
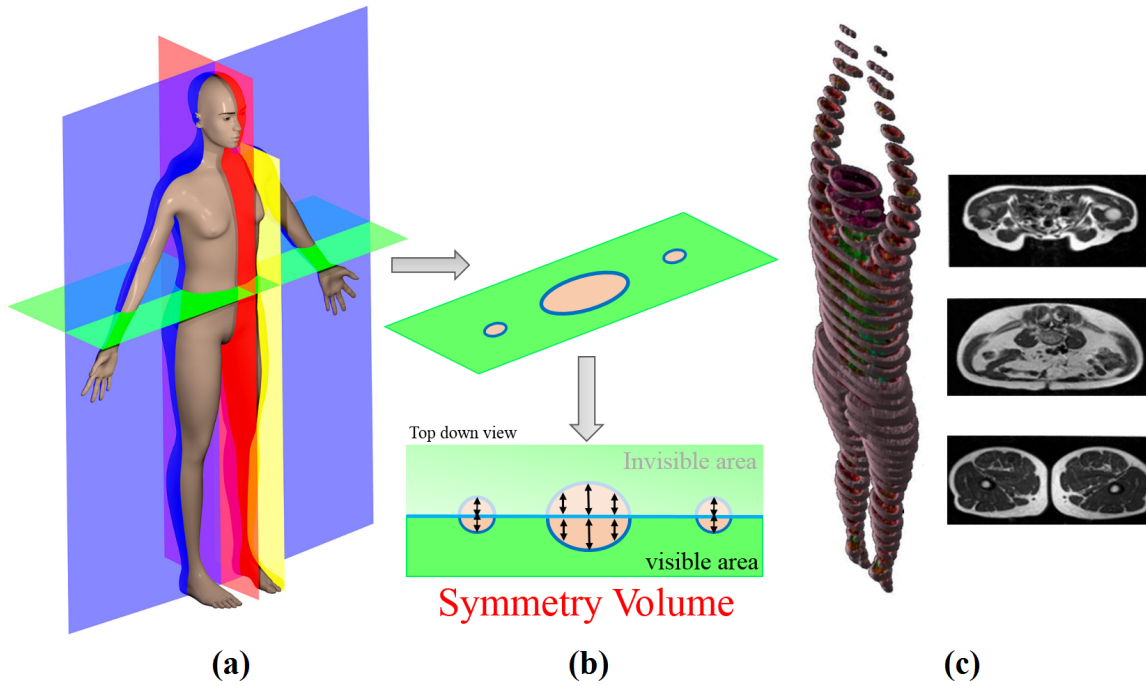
Figure 5.2: Key Idea of the Artificial Symmetry 3D Volume Mesh.

has the same symmetry shape as the visible area, as illustrated in Figure 5.2 (b). Figure 5.2 (c) is an illustration of the Magnetic Resonance Imaging(MRI) [86] which is a medical imaging technique used in radiology to form pictures of the anatomy. In other words, a number of pictures of the anatomy are extracted and then all the pictures extracted are stacked up to generate the 3D shape of the human body. The key concept of the proposed AS-HKS algorithm is grounded this MRI process. It generates a full artificial 3D symmetry volume body mesh using symmetrical volumes of visible and invisible areas.

3 Basic Concepts

To obtain accurate artificial symmetry volume mesh, the proposed algorithm is founded based on the three main ideas as follows.

- First, the basic concept of the proposed algorithm to generate an accurate artificial 3D mesh data comes from an ellipsoid and a sphere. On the basis of the fact that
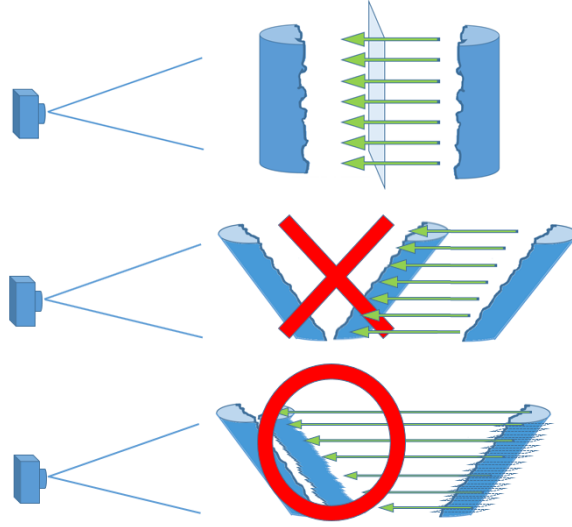
Figure 5.3: Illustration of Mesh cutting.

solid objects with volume have a rotational symmetry, it is assumed that visible and invisible areas of the range scan data are symmetrical to each other based on a symmetry plane between the two; then the generated artificial symmetry mesh is shifted with same distance to the original mesh in order to create the full closed mesh, as shown in Figure 5.3 (a) and Figure 5.2 (b). This assumption enables us to create a symmetrical counterpart mesh based on the visible areas of the target to generate a precise artificial 3D mesh. The generated artificial symmetry 3D mesh model can provide correct local and global HKS descriptors. Consequently, those local and global HKS descriptors allow us to easily find corresponding HKS feature points from different multiple range scan data.

- Second, in generating a symmetrical counterpart, the main challenge is how to identify the thickness of each part of the target. The generated symmetrical area mesh can simply be shifted to create a correct artificial 3D mesh as illustrated in Figure 5.3 (Top). However, as in the middle picture of the Figure 5.3, if the target is tilted and the range scan data entails different depth from a camera, a simple symmetrical counterpart is not capable of correctly identifying the thickness of the

46

target. To address and properly treat this problem, a mesh cutting concept is proposed. We shred the symmetrical counterpart into thin slices, as illustrated in the bottom picture of the Figure 5.3. Then, each cut depth contour line is shifted until it arrives at its corresponding visible depth mesh.

- Third, the thickness of an artificial volume mesh is occupied based on optimal depth value which is carefully selected among 4 different depth values from 4 different cutting directions. In Figure 5.4 (a), we generate a symmetry mesh following the horizontal cut direction and we attain the wrong depth model as shown in Figure 5.4 (b). Because all surface points in the same contour cut are shifted by the same amount, the black square area point has incorrect thickness distance from the front and back surface of the target. When the vertical direction slicer is utilized as demonstrated in Figure 5.4 (c), the black square area has correct depth thickness model in Figure 5.4 (d). Therefore, different angle cutting directions are mandatorily requested and the proposed algorithm suggests the 4 different angles, $(0°,45°,90°,135°)$ of slicers to obtain the optimal outcomes. In order to achieve higher effectiveness in this process, it is significant to select the best cutting direction. Hence, two criteria are proposed including 2D plane-distance and 3D depth-gap between two endpoints.

Rationale of 2 Criteria

The artificial closed contour is generated by one half of an ellipse from the original surface and its artificial half. Intuitively, in case of an object that has a smooth curvature on the surface, a smooth curve still exists in the boundary of visible and invisible areas of the surface. Thus, it is required that the generated artificial closed contour should also involve smooth curves. In Figure5.4 (b), the generated artificial contour points, identified with the black ellipse, have a simple linear line without a smoothly curved contour line in the boundary of the red (visible) contour and the

47
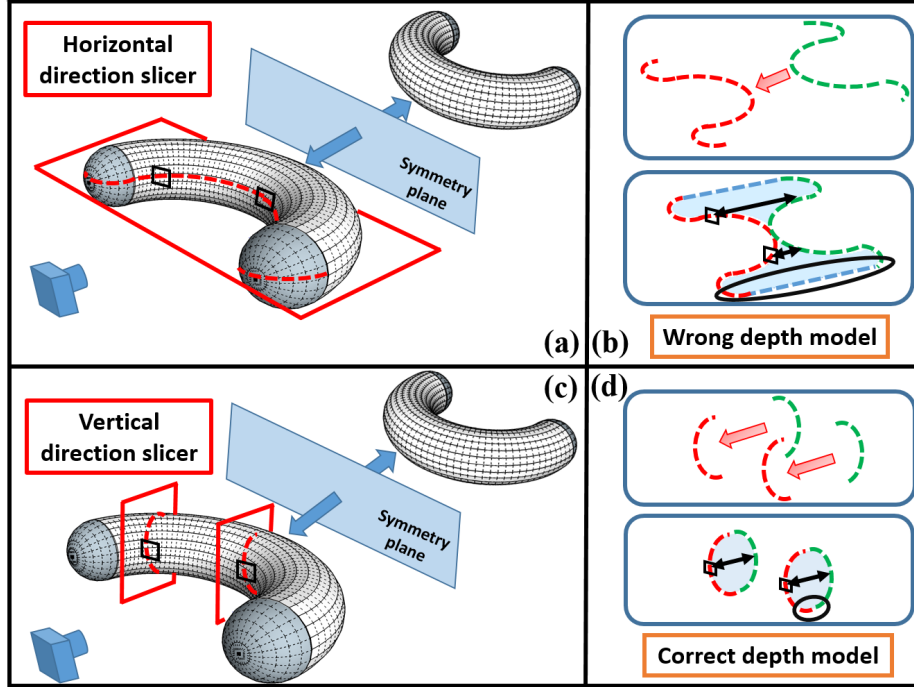
Figure 5.4: Illustration of Mesh cutting in 4 different angle directions.

green (artificial) contour. It is mainly because of the wrong thickness calculated by the horizontal direction. In other words, the cross section created by the horizontal cut entails an incorrectly extended area because the linear line between the visible and artificial contour creates extra space. On the other hand, in Figure 5.4 (d), the boundary of two contours, colored as red and green, has a smooth contour curve as presented with the small black ellipse. This clearly illustrates that the vertical cutting direction is required to attain the correct artificial symmetry depth value corresponding to the black square. These contrastive results provide a crucial implication that the smallest cross section area should be formed by cut; that is, the optimal cutting direction should be able to create the smallest cross section area in order to generate the artificial 3D mesh with correct thickness. In order to correctly choose an optimal cutting direction, two major criteria have been proposed in the present study.

1$^{\text{st}}$ Criterion: Shortest Path Direction of Depth Map

The 4 cutting directions introduced above are represented as the 4 different lines respectively in the 2D depth map image. Among these 4 lines, the cutting direction which can create the smallest cross section area involves the smallest number of the pixels in the 2D depth map image and should be selected as an optimal cutting direction for the successful outcome. Accordingly, the first criterion is proposed to discover the shorted path direction in the 2D depth map image.
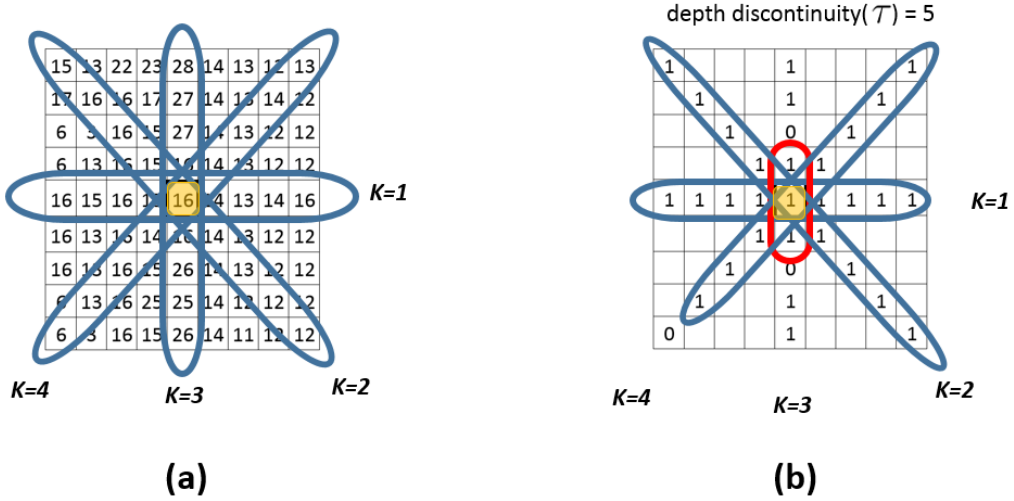
Figure 5.5: Illustration of 1$^{\text{st}}$ Criterion: (a) 2D Depth Map; (b) Depth discontinuity and the best candidate.

Depth discontinuity indexing, $\mathcal{P}_{i,j}$ is

$$\mathcal{P}_{i,j}^{(k)} = \begin{cases} 1, & \text{if } |d_{i,j} - d_{i+s,j+t}| < \tau \\ 0, & \text{if } |d_{i,j} - d_{i+s,j+t}| > \tau \end{cases} \tag{5.1}$$

where

$$(s,t) = \begin{cases} (0,\pm 1) & \text{if } k = 1 \\ (\mp 1, \pm 1) & \text{if } k = 2 \\ (\pm 1, 0) & \text{if } k = 3 \\ (\pm 1, \pm 1) & \text{if } k = 4 \end{cases} \tag{5.2}$$

where τ is a threshold to detect depth discontinuity, $d_{i,j}$ is depth value in (i,j) pixel in a depth map and k refers to four directions $(0°, 45°, 90°, 135°)$ as shown in Figure 5.5(a).

We name $\mathcal{A}_{i,j}^{(k)}$ as the array of depth continuity, $P_{i,j}^{(k)}$; $\mathcal{A}_{i,j}^{(k)}$ refers pixels from (i,j) pixel to the connected neighboring pixels, which have n number of continuous pixels in k direction. The number of elements in the array set is as follows:

$$n^{(k)} = (\left| \mathcal{A}_{i,j}^{(k)} \right|). \tag{5.3}$$

The first criterion to choose the correct depth is defined as,

$$\mathcal{C}_{i,j}^{(1)} = \operatorname*{argmin}_{k} (n^{(k)}), \tag{5.4}$$

where $\mathcal{C}_{i,j}^{(1)}$ value has an optimal cutting direction label as the first candidate of (i,j) pixel in the depth image in order to find the optimal depth among 4 different depth values. As in Figure 5.5(b), the red circle direction is selected as the best candidate.

Figure 5.6 provides the illustration of the 4 different angle directions and the optimal cutting of the whole surface of the object. In Figure 5.6(b), This AS-HKS algorithm attempts to check every single point using 4 different angle directions as an attempt to identify the most appropriate cut line to generate the correct symmetry volume mesh (Figure 5.6 (b)).

(a) 4 Different cutting directions

Depth Map from camera

(b) Choosing Shortest path direction

(c) Optimal cutting directions
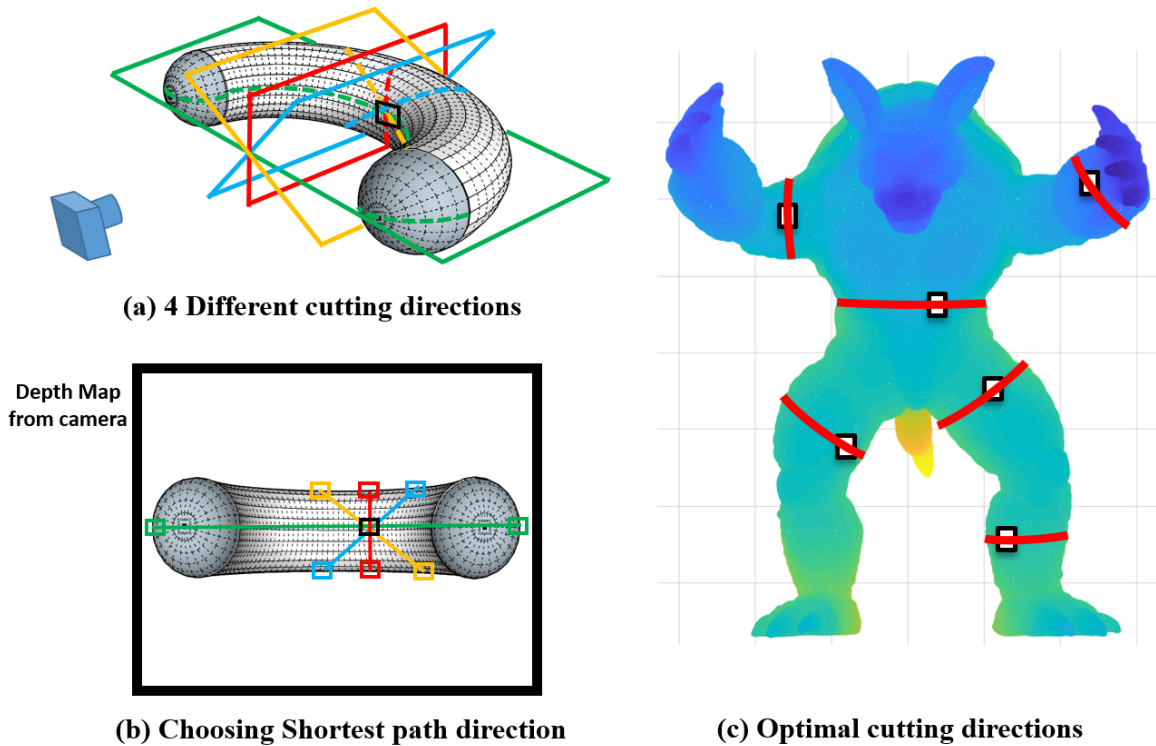
Figure 5.6: 1st Criterion: Illustration of 4 different angle directions: (a) 4 Different Cutting directions; (b) Choosing the shortest path direction; (c) Optimal Cutting directions.

2nd Criterion: Smallest Depth-Gap Direction between Two Endpoints of Input Mesh Boundary

Certain problems still remain even when we select the minimum 2D plane-distance among the 4 different angles directions. The primary reason is that this cutting line from the maximum curvature direction selected often fails to identify an optimal line mainly due to the complex shapes of the target and the various camera directions to the target surface.

As indicated in Figure 5.7 (a), from the top-down view in the 3D space, a green colored line is identified as the shortest 2D plane-distance in the range scan data from a camera view direction. However, the green contour line direction leads to a wrong
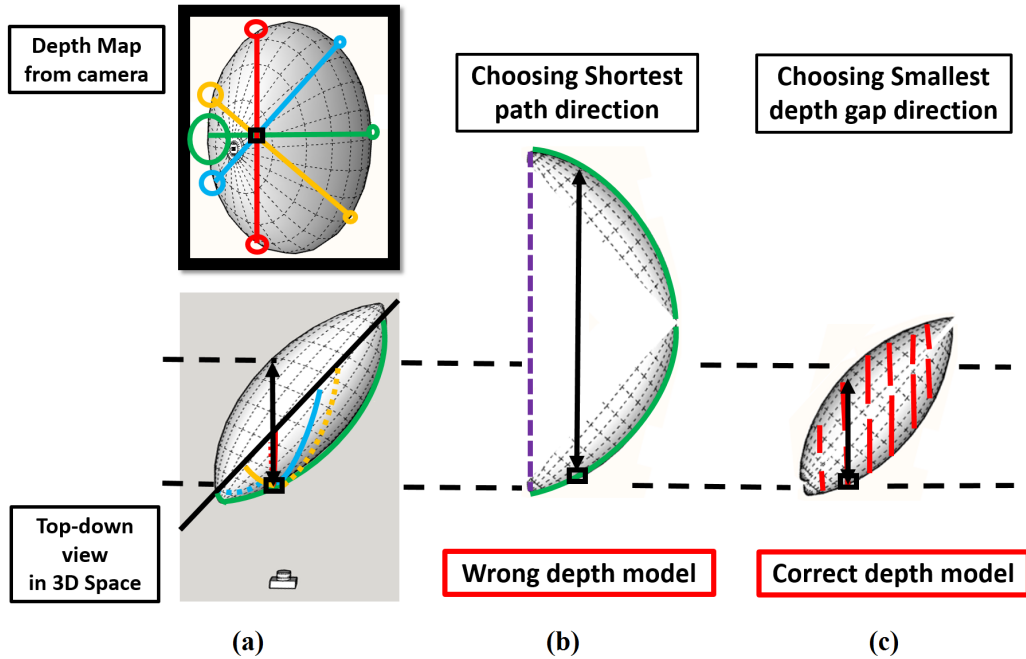
Figure 5.7: 2nd Criteria: Smallest depth-gap between two endpoints: (a) Top-down view in 3D space and Depth Map from the camera (in the Depth Map, the size of the colored circle indicates the depth value from the camera; the bigger size of circle means the closer distance depth value); (b) Wrong depth model based on the 1st Criteria (c) Correct depth model based on the 2nd Criteria.

artificial symmetry depth contour line mainly because the two unmatched depth contour lines fail to generate a fully closed ellipse shaped volume. The primary reason is that the left-end boundary point and the right-end boundary point have different depth values from the camera and accordingly these two endpoints have huge depth-gap, as demonstrated in Figure 5.7 (b). Hence, the left-end boundary points from the visible contour and its symmetrical counterpart are unable to meet each other and the linear contour line is used to generate a closed contour. Further, it results in the failure to generate a correct artificial 3D mesh. As an attempt to solve this problem, the cut line with the smallest depth gap between two endpoints is selected in order to successfully obtain the best results. To be more specific, as shown in Figure 5.7 (c),

the red direction is the longest path direction, which should be discarded following the first criterion. However, it is considered to be the optimal selection primarily because this direction entails the smallest depth gap. This direction is capable of providing the correct depth model to get the correct thickness of the model.

Depth gap between two-endpoints (first index (1), last index (n)) of continuous array is described by $\mathcal{G}_{i,j}^{(k)}$,

$$\mathcal{G}_{i,j}^{(k)} = |\mathcal{A}_{i,j}^{(k)}(1) - \mathcal{A}_{i,j}^{(k)}(n)|. \tag{5.5}$$

The second criterion to choose the correct depth is defined as $\mathcal{C}_{i,j}^2$,

$$\mathcal{C}_{i,j}^2 = \underset{k}{\operatorname{argmin}} \, (\mathcal{G}_{i,j}^{(k)}), \tag{5.6}$$

where $\mathcal{C}_{i,j}^2$ value entails the optimal cutting direction label as the second best candidate of the (i,j) pixel in the depth image, which is able to detect the optimal depth among the 4 different depth values.

Decision-Making Process on Depth

As previously explained in detail, the proposed algorithm considers two different criteria to identify an optimal mesh cut line direction for more accurate symmetry 3D volume mesh. Accordingly, the next research task that should intuitively arise will be which option should be prioritized between the two considerations. As an attempt to deal with this challenge, the proposed approach suggests a logical decision making process that carefully considers both concurrently. As described above, from the original range scan depth map, we extract symmetry volume depth which entails 4 different symmetry depth values from the 4 different angle directions. Thus, the next important step is to label the most appropriate candidate among those four by prioritizing combination of 2D plane-distance and depth-gap of two endpoints. The top priority goes to the combination where the best directions from both criteria are matched. Therefore, two candidates of the best priority are available for the best

cutting direction; and it is mandatory to make an appropriate decision to identify the optimal direction based on the combination of two different priorities.
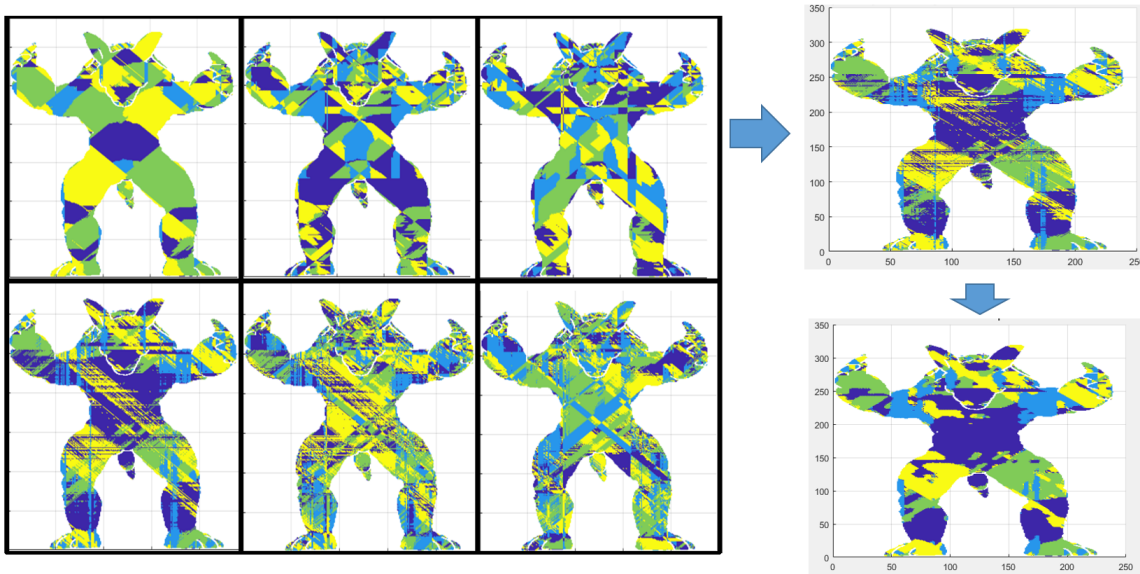
Figure 5.8: Priority combination between 2D plane-distance and depth-gap of two endpoints and denoising results.

In Figure 5.8, the 3 top left figures illustrate the 3 best candidates in the order of the 2D plane-distance standpoint whereas the 3 bottom left figures demonstrate another 3 best in the order of the depth-gap standpoint. The upper right picture represents the labeling results based on the priority combination whereas the bottom one shows the outcome of denoising and smoothening. The right side of Figure 5.9 demonstrates 4 different depth volumes from the 4 different angle directions which are selected on the basis of labeling as shown in the bottom right of Figure 5.8.

Refinement

The final stage in generating an artificial symmetry 3D volume mesh is to refine the outcomes of the previous step through denosing and removing. The selected depth values from the smoothened labels still have some errors in depth continuity. Thus, firstly, this stage attempts to denoise those depth values to obtain smooth depth
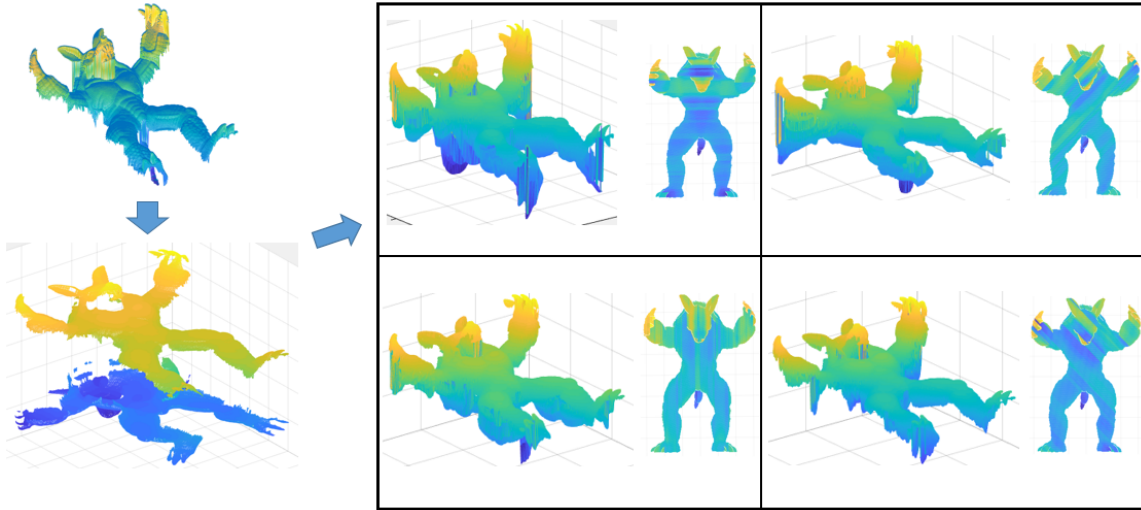
Figure 5.9: Artificial Symmetry 3D volume mesh and 4 Different depth volumes based on 4 Different angle directions (0°,45°,90°,135°).

surfaces. As stated, the artificial symmetry 3D volume mesh aims to extract HKS feature points only in the visible areas of the target and to find their corresponding HKS feature points from multiple partial overlapping range scan data. To accomplish this purpose, fully closed range scan data is required and furthermore, symmetrical counterparts should have smooth surfaces without depth discontinuity. Therefore, in this stage, we perform the procedure to denoise some depth values to identify the accurate HKS feature points required. The second and third pictures of Figure 5.10 show the results of this denoising step: initial depth values and artificial mesh depth values, respectively.

Another refinement step, removing is illustrated in the bottom pictures of Figure 5.10. It shows the merging results of visible and invisible surface mesh after removing unnecessary broken artificial symmetry counterpart meshes. The original range scan data and its symmetrical counterparts are often divided into several separate meshes by depth discontinuity. In such cases, in order to generate a fully closed artificial 3D mesh, it is required to reconnect the biggest sized symmetrical pair and other symmet-
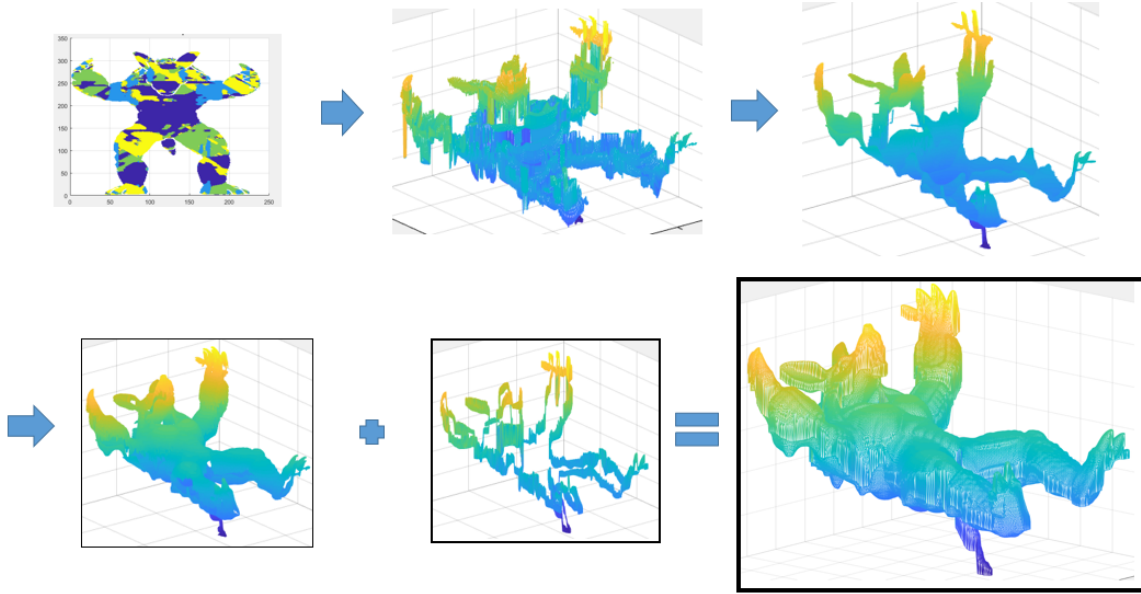
Figure 5.10: Outcomes of Denoising and Removing.

rical pairs which entails a close distance to the biggest one. With this reconnection process, the algorithm is capable of distinguishing the appropriate symmetrical pairs which have smaller distance than a threshold to detect depth discontinuity and also able to remove unnecessary broken meshes. The refined symmetrical pair is completely connected with a side mesh and further can generate a fully closed artificial symmetry 3D volume mesh.

5.3.2 Coarse Registration by 3 pairs of AS-HKS

AS-HKS keypoints and AS-HKS descriptors

Based on the fully closed artificial 3D model from multiple range scan data generated by the previous stage, we extract AS-HKS features and group the AS-HKS keypoints in order to ensure one-to-one mapping across multiple views. Grouping the keypoints is performed by using their 3D geodesic distance and the similarity of their AS-HKS descriptor value over a long period of time. A longer period of time is required to check the similarity of global AS-HKS descriptors mainly because grouping demands

global closeness on the surface.
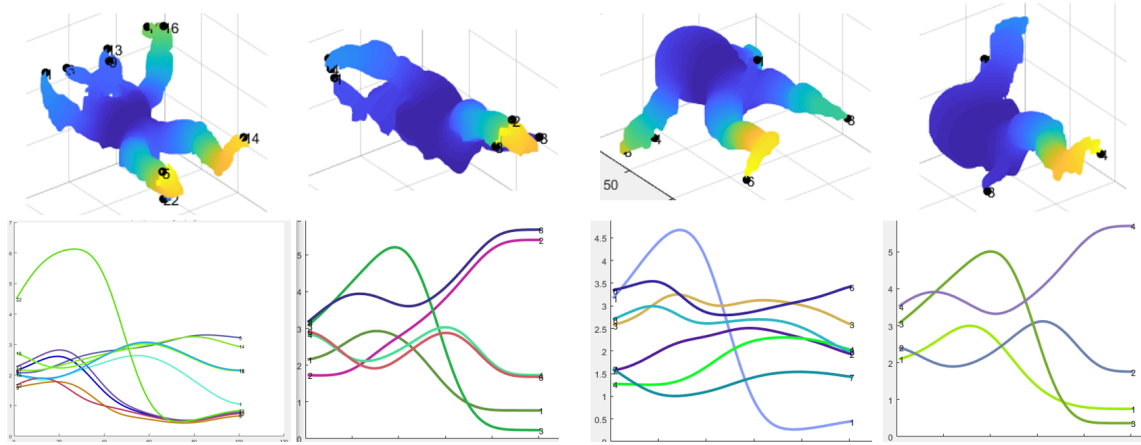
Figure 5.11: AS-HKS keypoints in artificial 3D mesh and AS-HKS descriptors over time.

Top pictures in Figure 5.11 demonstrate heat kernel values and the grouped AS-HKS keypoints on the surface of the artificial 3D mesh model. The yellow colored area represents high values of heat kernel function and corresponds to positive Gaussian curvature areas. In case of the long fixed time period for heat kernel function, high values of heat kernel indicate the end region of the target whereas low values of the heat kernel indicate the center region. Accordingly, as shown in the top pictures of Figure 5.11, the end regions of the target are presented with yellowish colors whereas the chest or body regions of the target are identified with dark-blueish colors. These extracted AS-HKS keypoints over the fixed long time period, which have only global AS-HKS features, are not sufficient to find corresponding AS-HKS features; hence, the full-period time AS-HKS descriptors of the AS-HKS feature points should be checked to use both global and local AS-HKS descriptors, as shown in bottom pictures of Figure 5.11.

In those figures, the X axis indicates different time periods whereas the Y axis presents heat kernel values. The curves illustrate AS-HKS values over different time

periods. The similar shaped curves over time indicate the globally and locally similar AS-HKS keypoints, which are considered as the possible corresponding points.
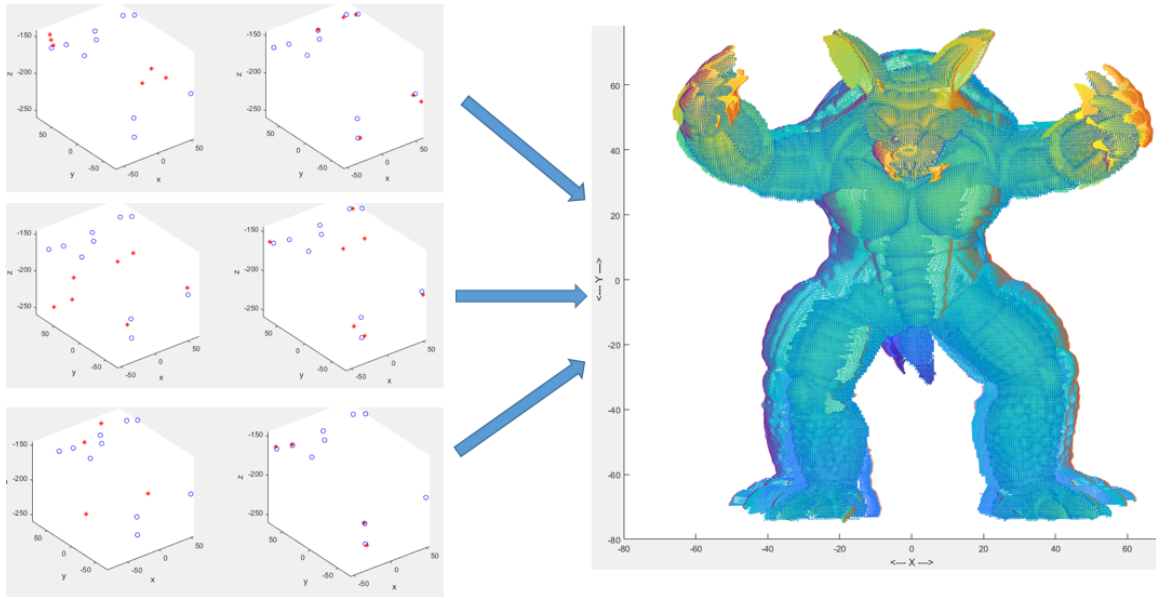
Figure 5.12: Initial registration results based on 3-pairs of AS-HKS features keypoints and AS-HKS descriptors.

Coarse Registration based on 3 pairs of AS-HKS

The possible corresponding AS-HKS keypoints identified above are created on the basis of the AS-HKS descriptor curves from the artificial 3D mesh model. Therefore, they can be similar to the original target but not completely equal depending on the original range scan view directions. Thus, we propose a new approach to perform initial registration based exclusively on the 3 best pairs of the AS-HKS keypoints. We repeat registration based on the 3 pairs of AS-HKS keypoints and find the pair with the smallest RMS error. The left 3D plot in Figure 5.12 shows the initial position prior to initial registration whereas the right 3D plot presents the result of the 3 pairs AS-HKS points-based registration. And the right Figure 5.12 represents the initial registration results of multiple range scan data with no initialization.

5.4 Experimental Results

In Figure 5.13, we thoroughly evaluated the accuracy of the AS-HKS coarse registration under the same test setting as the previous one utilized in Chapter 4. The 4 different input data which have approximately 90° rotation gap and some translation gap were employed to verify the AS-HKS coarse registration algorithm; as a result, it was possible to obtain relatively higher accuracy in comparison with the results of the PA-HKS coarse registration.
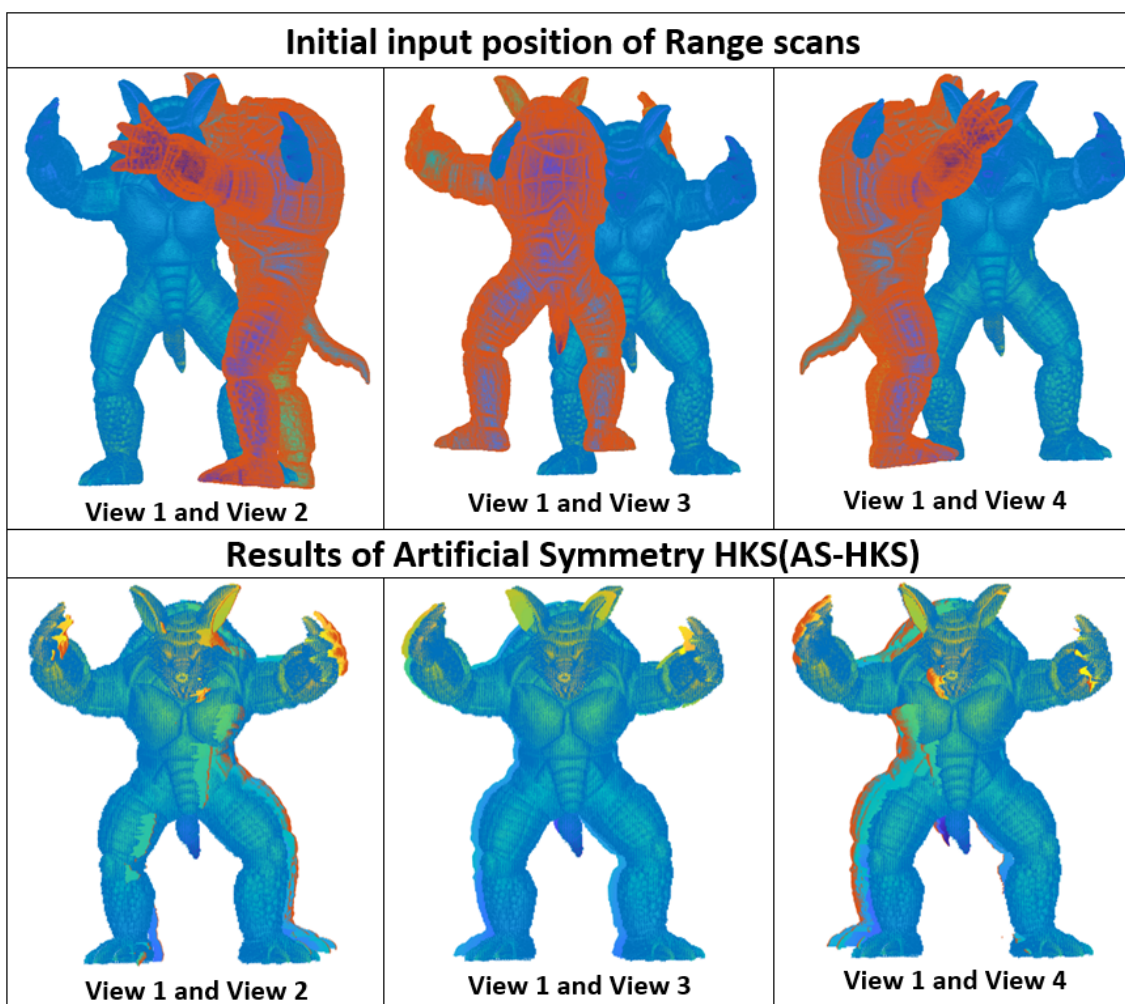
Figure 5.13: Results of each view transformation based on the AS-HKS.

In Table 5.1, we also can verify the effectiveness of the AS-HKS coarse registration

			Rotation Angle Gap			Translation Gap		
			Roll	Pitch	Yaw	X	Y	Z
Case 1	Overlap	Ground truth	2.07°	1.93°	88.00°	196	3	-203
(V_1, V_2)	15.11%	AS-HKS	5.95°	4.52°	95.17°	198.3	17.9	-226.4
Error of AS-HKS			**3.88°**	**2.59°**	**7.17°**	**2.3**	**14.9**	**23.4**
Case 2	Overlap	Ground truth	4.57°	4.49°	−174.4°	-5	2	-402
(V_1, V_3)	29.80%	AS-HKS	3.44°	7.39°	−176.8°	-0.3	12.7	-398.5
Error of AS-HKS			**1.13°**	**2.90°**	**2.40°**	**4.7**	**10.7**	**3.5**
Case 3	Overlap	Ground truth	−1.78°	2.20°	−96.0°	-197	2	-195
(V_1, V_4)	27.89%	AS-HKS	−5.84°	4.82°	−96.1°	-200.7	16.2	-197
Error of AS-HKS			**4.06°**	**2.62°**	**0.10°**	**3.7**	**14.2**	**2**

Table 5.1: Results of Coarse registration by AS-HKS in comparison with given ground truth.

numerically from the test setting. The estimation of transformation by AS-HKS was compared with ground truth values in order to show accuracy of the AS-HKS algorithm. As shown in the 3 cases in the table, the estimation error of rotation in comparison with ground truth shows approximately less than 8° by Rall, Pitch, and Yaw rotations; translation error is less than approximately 25. It proves the effectiveness of the proposed algorithm with enhanced accuracy compared with the PA-HKS coarse registration.

Comparison: AS-HKS vs PA-HKS

The present chapter successfully proves that the AS-HKS algorithm is capable of providing more accurate outcomes in comparison with the previous PA-HKS. Compared with Table 4.1, Table 5.1, in the same test setting, represents enhanced accuracy in the AS-HKS algorithm. In Figure 5.14, it is clearly illustrated that the AS-HKS, (a)

provides much more accurate outcomes in comparison with the PA-HKS, (b) in the setting of using 4 input range scan data to perform coarse registration. Figure 5.14 (c) and (d) present the results using only 3 inputs range scan data. As demonstrated, the PA-HKS algorithm fails to perform registration; on the contrary, the newly proposed AS-HKS algorithm is still capable of providing robust results as shown in Figure 5.14 (d).
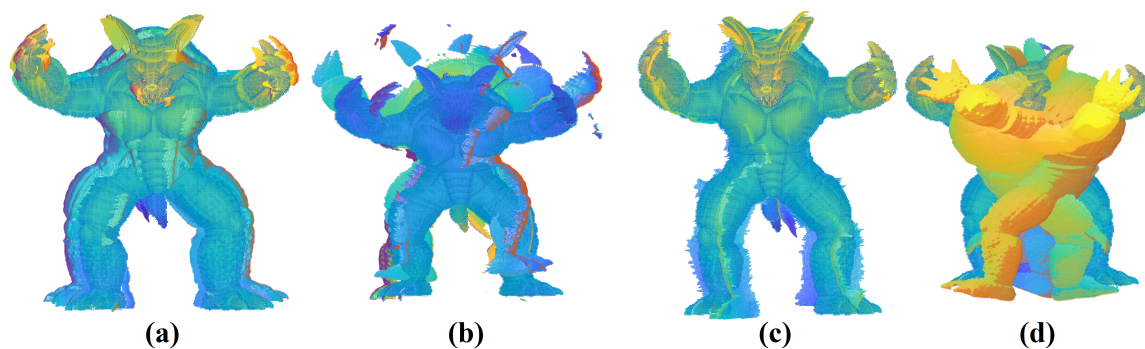

(a) (b) (c) (d)

Figure 5.14: Results of Coarse registration: AS-HKS and PA-HKS : (a) Coarse registration by AS-HKS using 4 inputs; (b) Coarse Registration by PA-HKS using 4 inputs; (c) Coarse registration by AS-HKS using 3 inputs; (d) Coarse Registration by PA-HKS using 3 inputs.

CHAPTER VI

Fine Registration based on MM-ICC

6.1 Outline of M-ICC

Wang [52] proposed the wide baseline 3D modeling algorithm, called the M-ICC, that performs registration of multi-view range scans through maximizing contour coherence among the observed and predicted contours across multiple views. It is grounded on the fact that the contour has been recognized as a rich source of geometric information for motion estimation and 3D reconstruction [49,52]. As shown in Figure 6.1 (a), the observed contours, which are derived from the original 2.5D range scans, show discordance to the corresponding predicted contours, which are extracted from the projected 2.5D range scans. To be more specific, the red colored 'observed' lines do not match with the blue colored 'predicted' line in the left-side view; and the blue colored 'observed' lines do not match with the red colored 'predicted' line in the front view. Accordingly, in the present approach, contour coherence is maximized by iterative construction of the robust correspondences among apparent contours and minimization of the distances. Figure 6.1 (b) demonstrates the registration results with the maximized contour coherence and two well-aligned wide base line range scans. The observed and predicted contours extracted involve false contour points which are generated due to self-occlusion. Accordingly, two main research challenges come to attention: how to remove the false contour points and how to preserve only the corresponding contour points.

In Figure 6.2, the 3D object model entails the contour points, which are represented with a red solid line, in the view direction. In case that the 3D model is
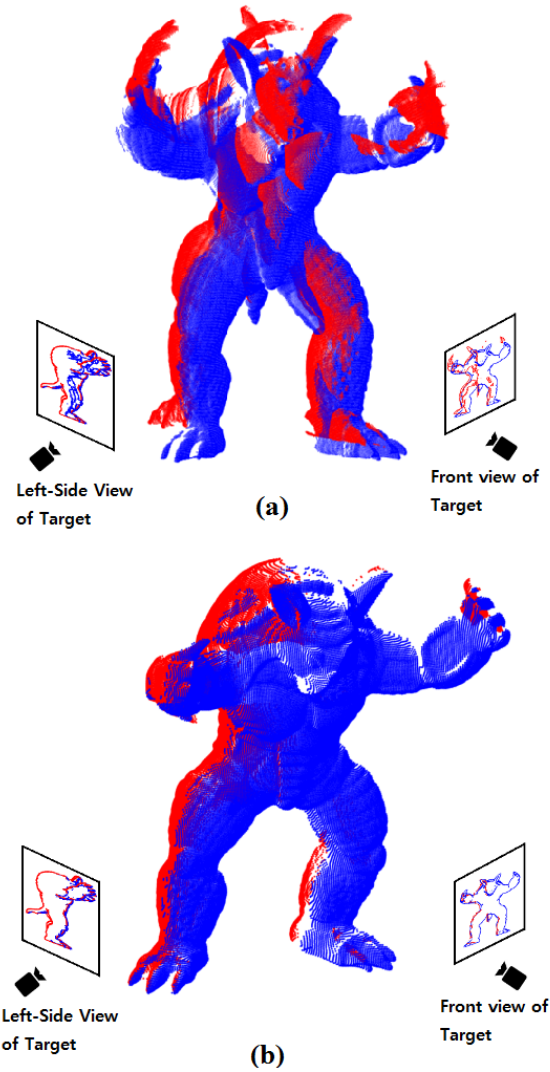
Figure 6.1: (a) Two roughly aligned wide baseline 2.5D range scans of the Stanford armadillo with the observed and predicted apparent contours extracted. Two meshed point clouds are generated from two 2.5D range scans; (b) Registration results of maximizing the contour coherence.

rotated to the different view direction, after rotation, the 3D model should include the new contour points, represented with a yellow solid line. If the 3D model entails fully covered 3D data, the previous contour, which exists before rotation, cannot be considered as contour points in the new direction. On the contrary, if the 3D model involves partial range scan data, not fully covered 3D data, then we can obtain the
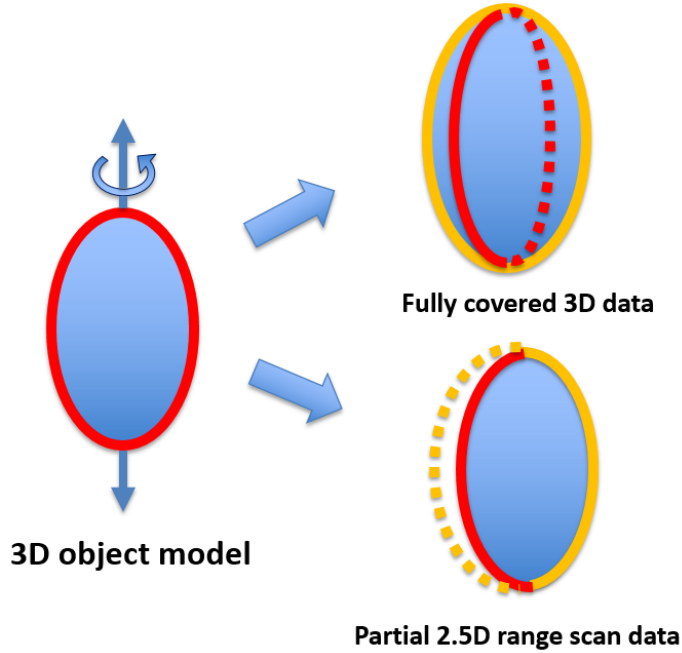
Figure 6.2: Illustration of the main idea of the pruning step.

red solid line and the yellow solid line as the new contour points instead of the yellow dotted line. It is mainly because the range scan data involve the invisible area due to self-occlusion and the surface area between the yellow dotted line and the red solid line cannot exist. Therefore, the red solid line still remains as valid contour points even after rotation. These false contour points increase errors in finding corresponding contour points between two different range scan data. Thus, these false contour points should be eliminated for successful outcomes. This is the basic concept of the pruning step.

6.1.1 Generating Observed R_i and Predicted Range scan data $R_{i \to j}$

A depth value, $R_i(\mathbf{x})$ is created by range scan R_i of view i at each image pixel $\mathbf{x} = (x, y)^T \in \mathbb{R}^2$. Range scan R_j also generates meshed point cloud M_j and $R_{i \to j}$ is provided by projecting M_j to the ith view. In addition, $N_i(\mathbf{x})$ is the surface normal vector of image pixel $\mathbf{x}$ in R_i.

6.1.2 Extracting Contour Points

The observed range scan data R_i entails two different sets of contour points. One set comes from the front contours whereas the other set comes from the back contours. The first pruning step sets the back contours as occlusion. In case of setting the pixel belonging to the object in view i as X_i, the depth of pixels which belong to the background is set by infinite, i.e., $R_i(\mathbf{x}) = \infty$ for $X \notin X_i$. The visible contour point set, $\mathcal{C}_i$ and the occlusion contour point set, O_i are differentiated by depth discontinuity of a pixel and its eight neighboring pixels, $N_X{}^8$ of the range scan, as represented in the following:

$$\mathcal{C}_i = \{\mathbf{x} \in X_i | \exists \mathbf{y} \in N_{\mathbf{x}}{}^8, R_i(\mathbf{y}) - R_i(\mathbf{x}) > \tau\}, \tag{6.1}$$

and

$$\mathcal{O}_i = \{\mathbf{x} \in X_i | \exists \mathbf{y} \in N_{\mathbf{x}}{}^8, R_i(\mathbf{x}) - R_i(\mathbf{y}) > \tau\}, \tag{6.2}$$

where τ is a threshold to control the quality of the PA-HKS features selected. Depth discontinuity occurs when the contours and occlusion contours are connected; it implies that self-occlusion in the range scan data creates some holes on the surface. These surface holes remain as the incorrect contour points and require a pruning step in order to obtain the successful registration outcome. In this step, R_i and $R_{i \rightarrow j}$ generate $\mathcal{C}_i$ and $\mathcal{C}_{i \rightarrow j}$ as the observed contour set and the predicted contour set, respectively.

6.1.3 Two Step Pruning

The First Pruning: Self-occlusion of the Predicted Contour

As mentioned above, self-occlusion creates some holes on the surface and the boundary points of these surface holes cause errors; hence, $\mathcal{C}_{i \rightarrow j}$ involves false contour points.

$$\mathcal{C}_{i \rightarrow j}^{(1)} = \{X \in \mathcal{C}_{i \rightarrow j} | \mathcal{C}_{i \rightarrow j}(X) \cap (\mathcal{O}_i(X) \cup \mathcal{C}_i(X))^c\}. \tag{6.3}$$
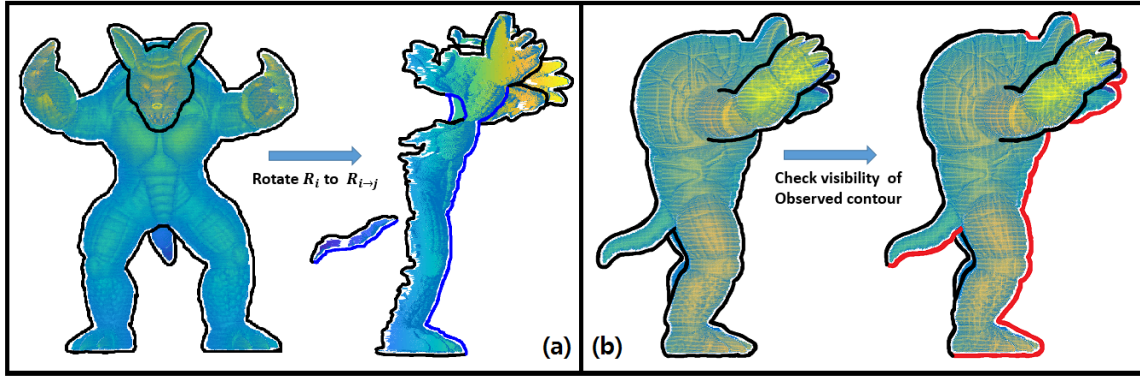
Figure 6.3: Illustration of 2 pruning steps in the M-ICC algorithm: (a) 1st pruning: the black line is the previous contour points C_i from the observed view i and the blue line is the new contour points $C_{i \to j}^{(1)}$ from the predicted view j; (b) 2nd pruning: the black line is C_j from camera j and the red line is the visible contour points from view i.

As in the equation above, fundamentally, the contour points fluctuate depending on different view angles in the fully covered 3D mesh data. Therefore, $\mathcal{C}_i$ and $\mathcal{O}_i$ from the observed view direction cannot be considered as the members of $\mathcal{C}_{i \to j}$ from the predicted view direction. In Figure 6.3 (a), the black colored line represents a visible contour in the previous camera i direction whereas the blue line indicates a new contour in the j direction after rotation of the range scan data R_i. The rotated range scan data R_i does not include the full surface of the target in the camera j direction; therefore, the black line cannot be recognized as a valid contour in the same camera j direction.

In Figure 6.4, the square point corresponds to a contour $\mathcal{C}_{i \to j}$ from the camera view j whereas the dot point refers to a contour $\mathcal{C}_i$ from the camera view i. In case that these contours are included in the same 3D location, the contours should be pruned for registration.
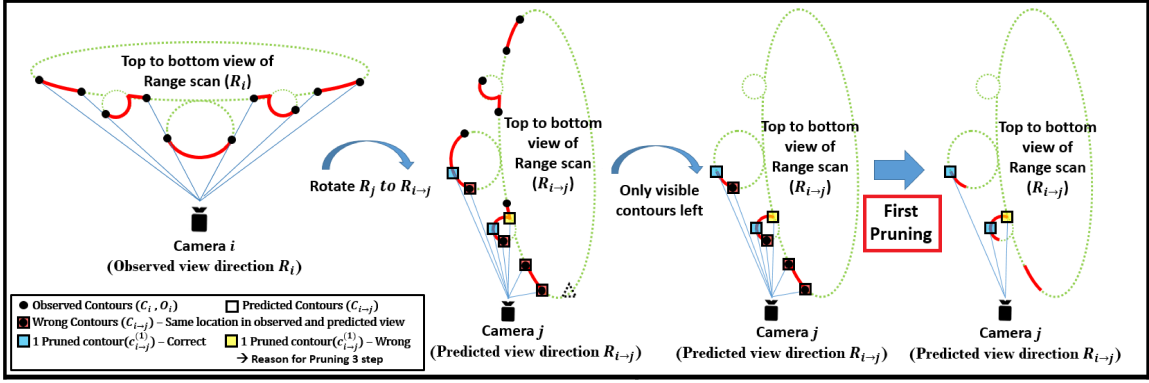
Figure 6.4: Illustration of the 1st pruning step.

The Second Pruning: Visibility of the Observed Contours

C_j should be pruned on the basis of the visibility of the corresponding contour in view i primarily because some contour points in C_j become invisible from the camera location of view i.

$$\mathcal{C}_{j/i}^{(2)} = \{X \in \mathcal{C}_j | N_j(X)^T \cdot (p_{i \to j} - V_j(X)) > 0\}, \tag{6.4}$$

where $p_{i \to j}$ refers to the camera location of frame i in camera j and $V_j(X)$ refers to the back-projection operator which plots X in frame j to its 3D location. Finally, $N_j(\mathbf{x})$ is a surface normal vector of each image pixel in frame j. In Figure 6.3 (b), the black colored line indicates a visible contour from camera j direction and the red line shows an invisible contour in i direction. The red contour need to be pruned in order to identify exclusively the corresponding contour points. Hence, only the black contours should remain after the first and second pruning steps mainly because the black contours include the corresponding contours. Again, in Figure 6.5, the red triangle point represents a contour from camera j and becomes invisible from camera i. Since these points do not entail correspondences in camera i frame, the pruning process is accordingly required.
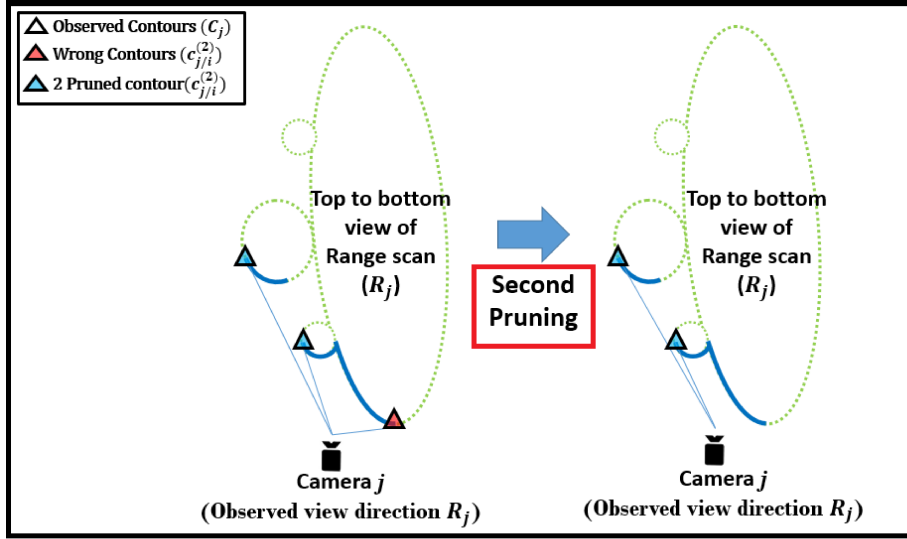
Figure 6.5: Illustration of the 2nd pruning step.

6.2 Modified M-ICC(MM-ICC)

6.2.1 Motivation of MM-ICC

Wang [52] claimed one algorithm to eliminate incorrect contour points through two-step pruning. However, this algorithm functions limitedly with a simple setting with less occlusions. Therefore, the present paper attempts to advance the contour coherence by the refinement process of the contour correspondences via the third pruning step. This additional pruning step is capable of eradicating incorrect correspondences of the predicted contours according to the invisibility condition. This upgraded algorithm is named as the Modified M-ICC, MM-ICC. Figure 6.6 shows the motivation of the third pruning step. Figure 6.6 (a) shows some wrong contour points as the results of the 1st and 2nd pruning. The blue dots in the black circle are the wrong contour points and increase errors in the registration outcome.
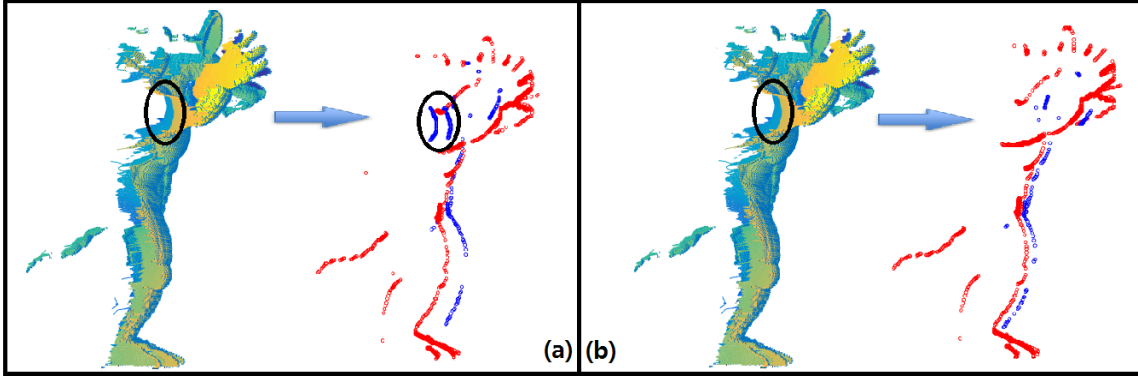
Figure 6.6: Motivation of Third pruning step in the MM-ICC algorithm: (a) Results of the 1st and 2nd pruning: the blue dots $(C_{i \to j}^{(1)})$ and the red dots $(C_{j/i}^{(2)})$ are the pruned contour points sets. The blue dots in the black circle are the wrong contour points and increase errors in the registration outcome; (b) Results of third pruning step: the wrong blue dots are pruned.

6.2.2 Main Contribution : Third Pruning Step

This paper proposes three pruning steps in order to find only the corresponding contour points from different views. Figure 6.7 illustrates the overview of the three pruning steps.

The Third Pruning: Visibility of the Predicted Contours

The third pruning is a newly proposed step in the present dissertation research. This stage is to be applied preceding to the first pruning mainly because the results of the first pruning step may still include incorrect contour points. Some contour points $C_{i \to j}$ generated by $R_{i \to j}$ are invisible in camera j; however, due to the self-occlusion effect, the points become visible in camera j. Accordingly, these incorrect points result in the errors in the matching step and further hinder accurate registration. As illustrated in Figure 6.4, the yellow square points are still identified as the visible contours in the predicted views although they should be invisible in camera j. Hence,
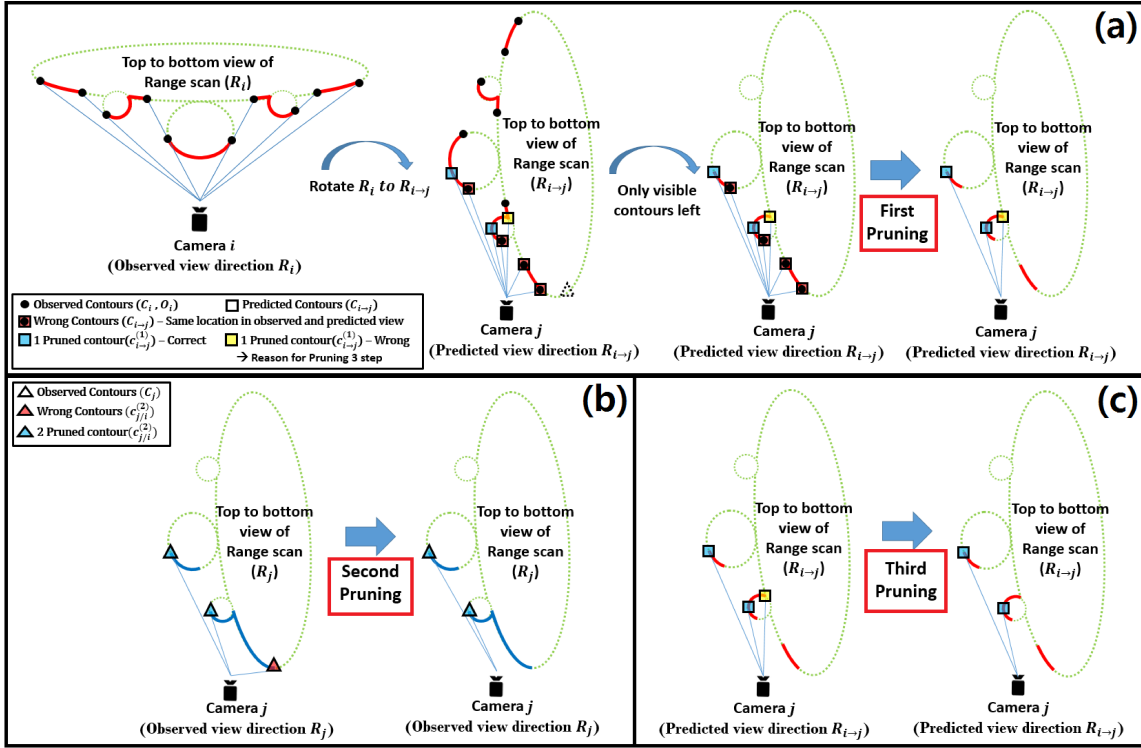
Figure 6.7: Illustration of the 3-step pruning from a top-down view: (a) 1st Pruning step: Removal of the wrong contours (black dots with a square) to remain the contour points $\mathcal{C}_{i \to j}^{(1)}$ (blue square and yellow square) in camera j; (b) 2nd Pruning step: Removal of the invisible contours (red triangles) in camera i; (c) 3rd Pruning step: Removal of the remained wrong contour (yellow squares) after the 1st pruning.

the third pruning is performed with a focus on the visibility of the predicted contour, as described in Figure 6.8. This supplementary pruning stage is the core part of the proposed MM-ICC algorithm:

$$\mathcal{C}_{i \to j}^{(3)} = \{X \in \mathcal{C}_{i \to j}^{(1)} | N_j(X)^T \cdot (p_{i \to j} - V_{i \to j}(X)) > 0\}, \tag{6.5}$$

where $V_{i \to j}(X)$ refers to the back-projection operator which maps X in frame $R_{i \to j}$ to its 3D location.

Therefore, using camera direction and surface normal vector$(N_i(\mathbf{x}))$ of image pixel, incorrect contour points are removed in this step.
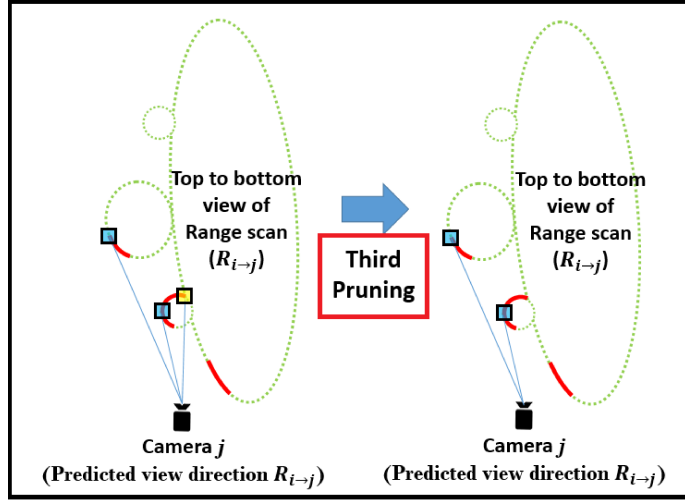
Figure 6.8: Illustration of the 3rd pruning step.

6.2.3   Matching in 3D using Trimmed ICP

Following the three pruning steps, two pruned contour point sets, $\mathcal{C}_{j/i}^{(2)}$ and $\mathcal{C}_{j\to i}^{(3)}$, are attained as the pruned observed contour and predicted contour, respectively. However, one research challenge still remains; not all points in the two contour point sets involve correspondences and further these contour points have high sensitivity to the minor changes of the viewing direction. Thus, there is still a need to identify the corresponding contour points and to perform precise matching. As an attempt to address this issue, the trimmed ICP algorithm [6] in the 3D space is proposed in the present research. The trimmed ICP is grounded on a consistent use of the Least Trimmed Squares (LTS) in order to categorize the square errors and to minimize a certain number of smaller values. Figure 6.9 shows the overview of the Trimmed ICP process. In this algorithm, the pairs which entail a big distance among the set of point pairs is neglected in order to avoid the incorrect corresponding points. This feature, accordingly, allows more robust outcome in comparison with the bijective method which is incapable of covering distant points [52].

Trimmed Iterative Closest Point

For each point of $\mathcal{P}$, find the closest point in $\mathcal{M}$ and compute the individual distances d_i^2.

⇩

Sort d_i^2 in ascending order, select the N_{po} least values and calculate their sum S'_{LTS}.

⇩

Stopping condition — Yes → **Stop**

⇩ No

set $S_{LTS} = S'_{LTS}$

⇩

Compute for the N_{po} selected pairs the optimal motion $(\mathbf{R}, \mathbf{t})$ that minimises S'_{LTS}.

⇩

Transform $\mathcal{P}$ according to $(\mathbf{R}, \mathbf{t})$
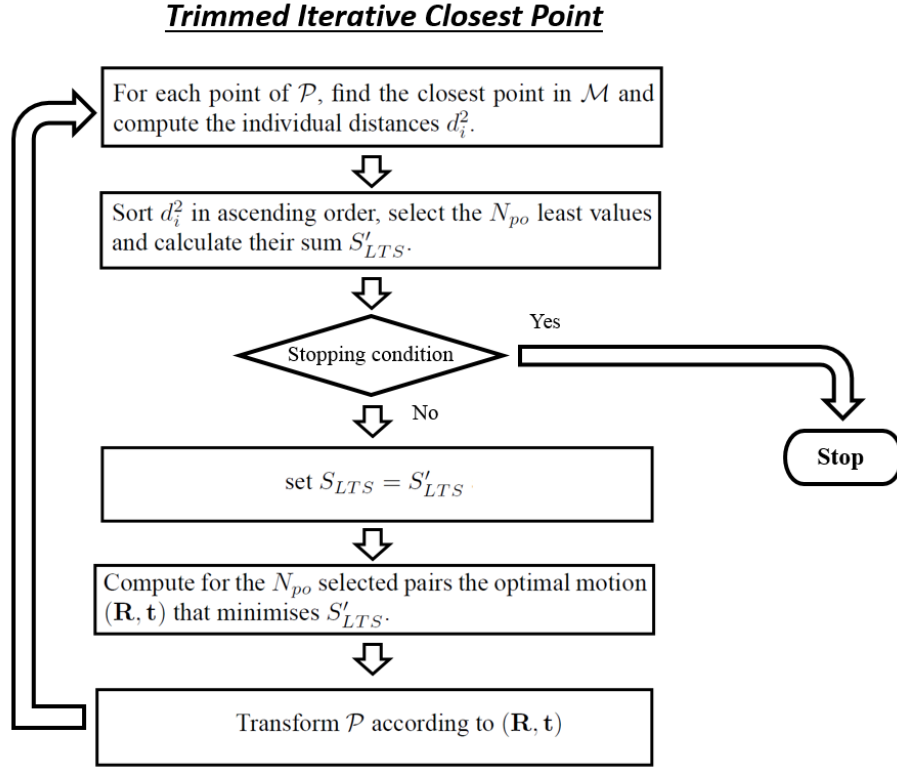
Figure 6.9: Overview of Trimmed ICP [6].

6.3 Results of the MM-ICC algorithm

MM-ICC for Refined Registration

Figure 6.10 verifies the effectiveness and accuracy of the MM-ICC algorithm in comparison with the M-ICC in the simple view setting which includes only 60° gap and less occlusion between the input views. The first row including (a), (b), and (c) shows the pruned observed and predicted contour points, initial location of the two data sets, the M-ICC results, and the MM-ICC results, respectively whereas the second row presents the point cloud data sets of the two range scans. Lastly, the third row illustrates the RMS error of the M-ICC (g) and the MM-ICC (h). In this comparison of the two algorithms, the M-ICC and the MM-ICC, the RMS error of the MM-ICC provides relatively small improvement in the simple input setting.

However, in case of the complex setting which entails more occlusion or large rotation angle gap, approximately 90°, the effectiveness of the MM-ICC algorithm is clearly proven as illustrated in Figure 6.11. The comparison of (e) and (f) visually validates the effectiveness of the MM-ICC; moreover, another comparison of (g) and (h) provides a numerical evidence to verify higher accuracy of the MM-ICC algorithm.

6.4   Discussion

The MM-ICC algorithm proposes the additional supplementary pruning step in order to effectively eliminate the supposedly invisible points in the predicted contours. This third pruning stage play a highly crucial role as a powerful assistance in the second-round re-registration; consequently, it significantly enhances the quality of the final registration outcomes.
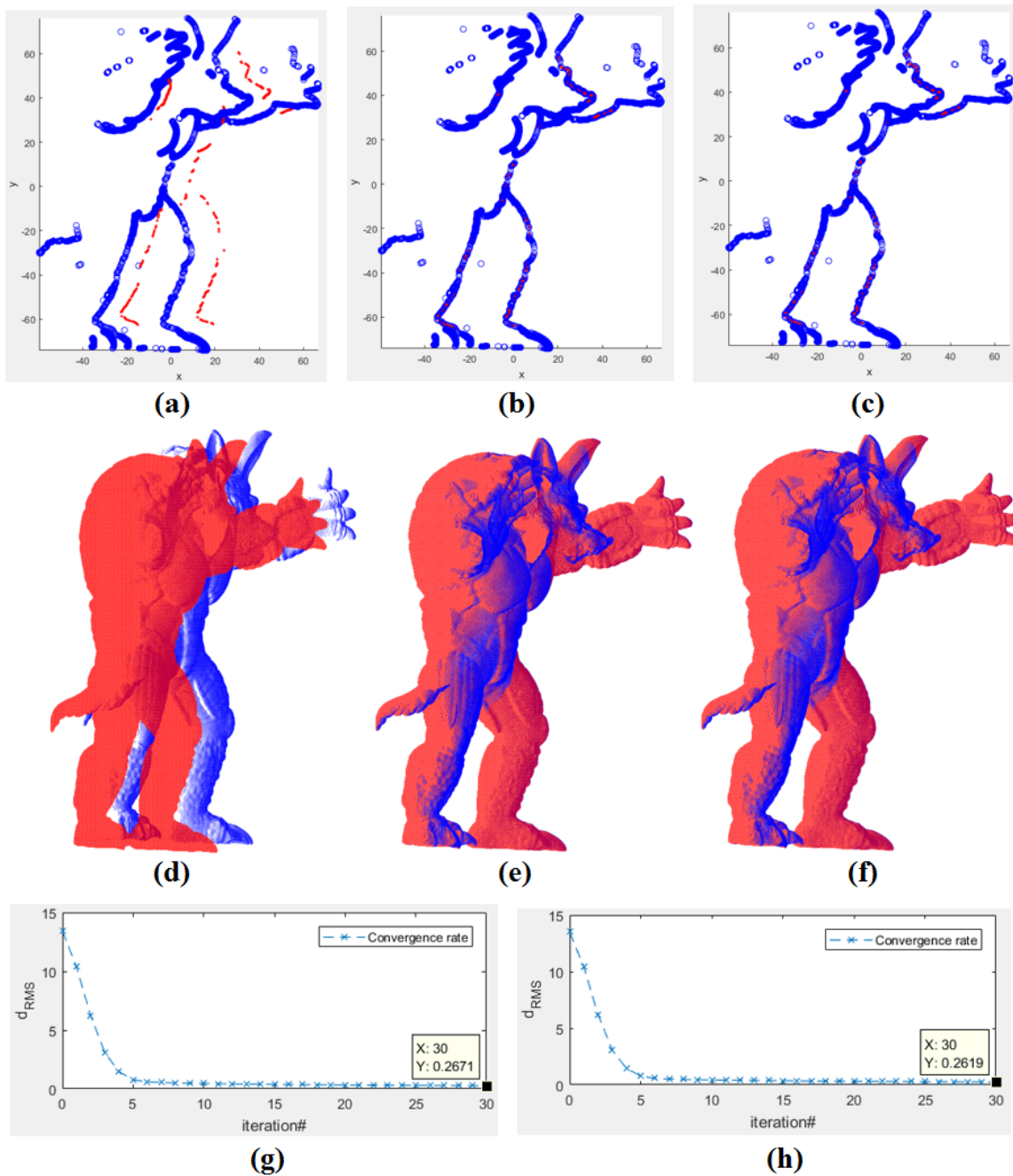
Figure 6.10: Results of M-ICC and MM-ICC in a simple view. Test Setting: Stanford armadillo 60° gap.

1st Row : Contour data. ((a)Initial position, (b)M-ICC, (c)MM-ICC)

2nd Row : Range scan data. ((d)Initial position, (e)M-ICC, (f)MM-ICC)

3rd Row : RMSE after registration algorithms. ((g)M-ICC, (h)MM-ICC).
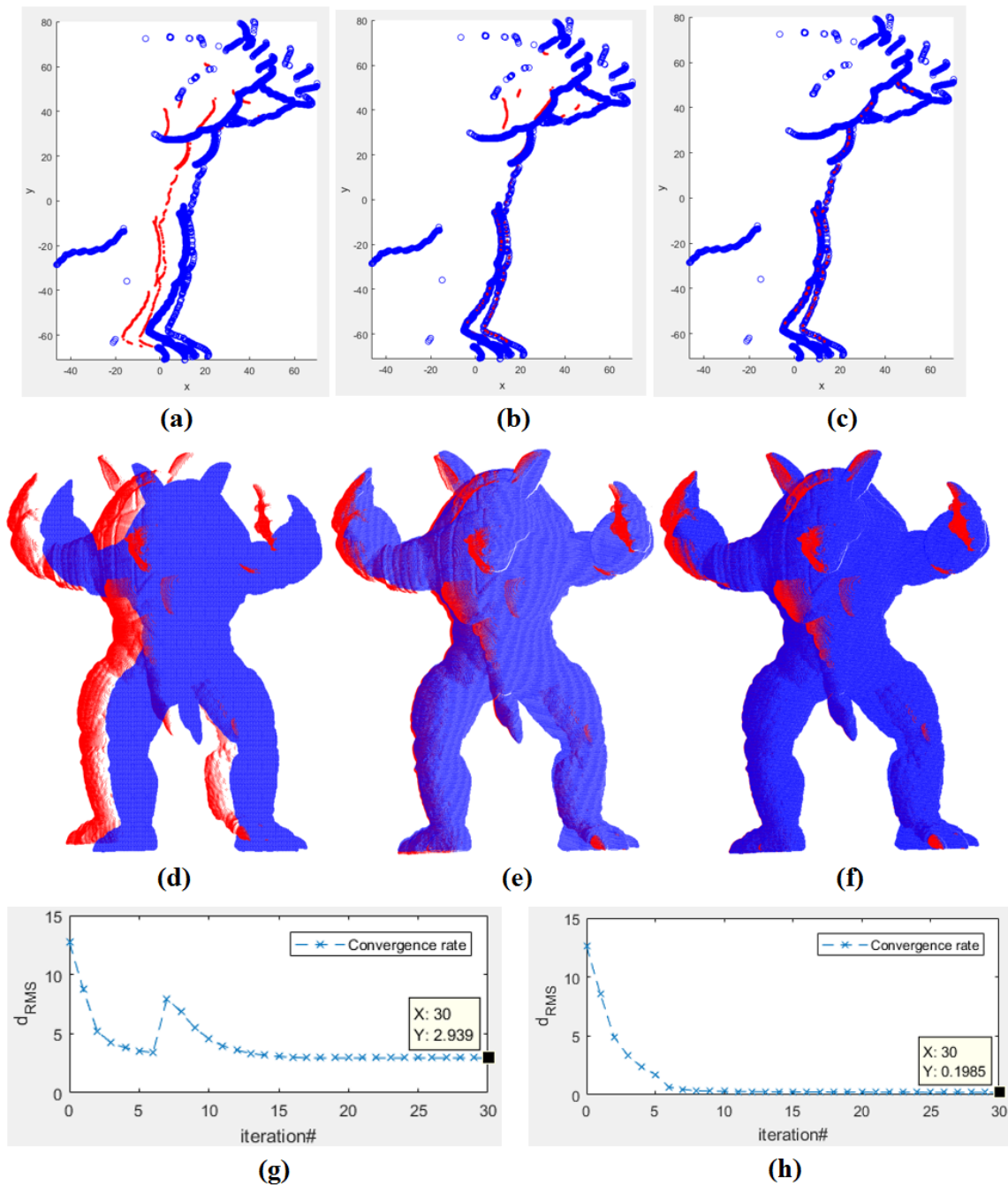
Figure 6.11: Results of M-ICC and MM-ICC in a complex view (Effectiveness of 3rd pruning). Test Setting: Stanford armadillo 90° gap.

1st Row : Contour data. ((a)Initial position, (b)M-ICC, (c)MM-ICC)

2nd Row : Range scan data. ((d)Initial position, (e)M-ICC, (f)MM-ICC)

3rd Row : RMSE after registration algorithms. ((g)M-ICC, (h)MM-ICC).

CHAPTER VII

Experimental Results

This chapter provides a detailed explanation about the research outcomes of the current disssertation research, "Fully Automatic Registration based on Combination of Coarse and Fine registration". In this chapter, the effectiveness of our proposed algorithm is evidently validated in comparison with the previous M-ICC algorithm and ground truth values.

7.1   Verification Criteria

Two separate criteria were employed in the present paper in order to validate a hypothesized range alignment. The first criterion is the grounded Root Mean Square (RMS) errors as the measure used to determine the accuracy, using the overlapping areas of the aligned scans. It was considered that corresponding points should be registered in the same location from the overlapping points. The second verification criterion is the visibility information. The smoothness and connectedness are visually evaluated for the verification. To be more specific, it was attempted to visually find out how smooth the registered surface would be and further how well connected the edge of each range scan data would be.

Root Mean Square Error (RMSE)

Root Mean Square Error (RMSE), which is also known as Root Mean Square Deviation (RMSD), has been a commonly employed criterion to measure the difference between the values predicted by a model and the values actually observed from the
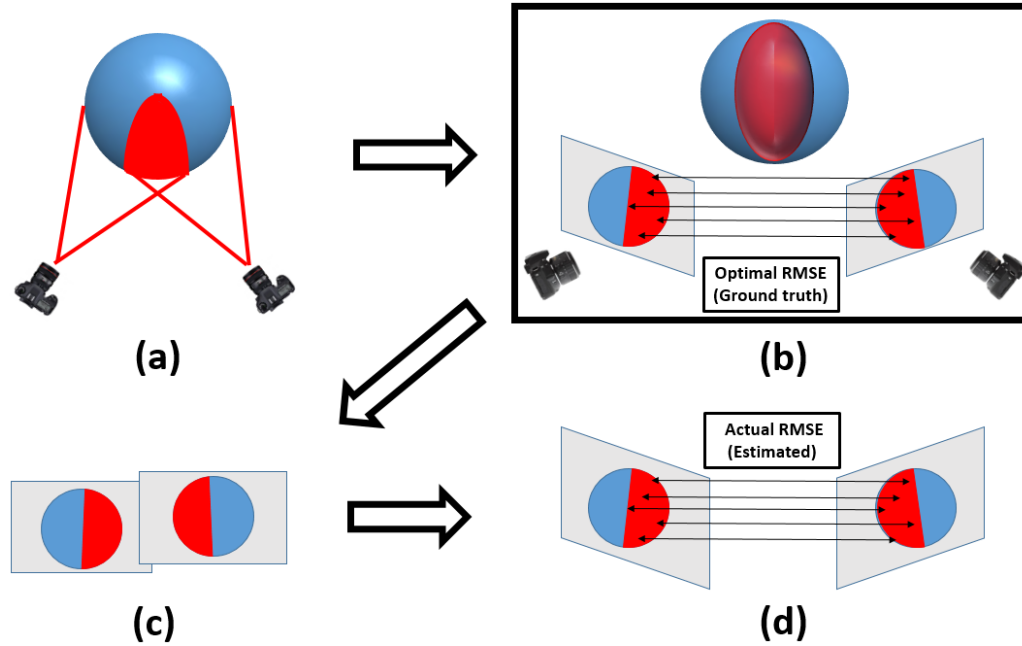
Figure 7.1: Illustration of Verification Criteria using RMSE: (a) Two range scan data for blue sphere (the red area is overlapped from two camera view directions); (b) Calculation of Ground truth optimal RMSE; (c) Arbitrary position of Range scans without initialization or camera calibration; (d) Results of the proposed algorithms and actual estimated RMSE.

environment that is being displayed [87–89]. These individual differences measured are also entitled as residuals; RMSE plays an important role to collectively calculate them into a single measure of prediction.

Figure 7.1 is the illustration of RMSE which is one of the verification criteria to evaluate accuracy of registration results of the proposed algorithms. Figure 7.1 (a) shows two range scan data of the blue sphere target from the top down view. Each of view camera directions covers different surface areas of the target and the red area is the overlapping area of the different view range scan data. Figure 7.1 (b) describes the optimal ground truth RMSE. In order to use RMSE as a valid verification criterion, only the overlapping areas should be used to calculate RMS. It is mainly because

corresponding points exist only in the overlapping areas. This optimal RMSE is used as a verification step by comparing with actual RMSE as in Figure 7.1 (d). Figure 7.1 (c) shows the arbitrary position of range scans without initialization or camera calibration and those range scans are used as input data for the proposed algorithms. Figure 7.1 (d) illustrates the estimated registration results based on the proposed algorithms and the actual estimated RMSE. Thus, in order to use RMSE as the verification criterion, we compare the optimal RMSE and the estimated RMSE. To be specific, we can validate accuracy of the proposed algorithms based on the degree of similarity between the estimate RMSE and the optimal RMSE: the closer values, the higher accuracy.

RMSE of a model prediction in regard to estimated variable $X_{predict}$ is defined as square root of mean squared error:

$$RMSE = \sqrt{\frac{\sum_{p=1}^{n}(X_i^{obs}(p) - X_j^{pre}(p))^2}{n}}, \tag{7.1}$$

where X_i^{obs} refers to the observed values in the view i direction and X_j^{pre} means the predicted values in the view j direction at place p, and n is the total number of corresponding points. We calculate the pairwise RMSE of two adjacent views to verify accuracy of the proposed algorithms. Thus, in the equation above, the view i and view j alternatively become the observed and predicted view.

RMSE values are still found to be beneficial to differentiate model performance in a calibration period from the performance in a validation period; moreover, this RMSE values can also be utilized to provide a compared result of the individual model performance to that of other predictive models.

7.2   Results of Proposed Algorithm

This chapter intends to provide the results of fully automatic registration based on the combination of coarse registration and fine registration. Accordingly, on the basis

of the results, this chapter attempts to validate the effectiveness of the proposed algorithm using the results of the combined registration algorithm which are the PA-HKS with the MM-ICC algorithm (PA-MMICC) and the AS-HKS with the MM-ICC (AS-MMICC) algorithm in comparison with the M-ICC and ground truth values.

7.3 Results of PA-HKS with MM-ICC(PA-MMICC) algorithm

This section provides the results of the proposed algorithm which combines the PA-HKS coarse registration with the MM-ICC fine registration as an attempt to verify the effectiveness. For this purpose, the results were compared with the previous M-ICC algorithm in the same test settings using different number of input range scan data.

The test setting includes two different types of the simple view range scan data which entail 70-degree angle gap and 90-degree angle gap in order to evaluate the capability to recover rotational errors of the input data. By 'simple', it refers to the setting with less self-occlusion views. Additionally, the complex view setting, which involves 90-degree angle gap between two input data, was also designed to validate the robustness of the proposed algorithm in overcoming the negative effect of occlusion.

As a result, the M-ICC showed relatively fine outcome exclusively in the simple view setting where low rotation angle gap exists. On the contrary, the proposed algorithm was capable of providing constantly successful performance both in the simple and complex view settings with high rotation angle gap.

In Figure 7.2, the left column demonstrates the results from the M-ICC algorithm under four different settings; the right column illustrates the results from the MM-ICC algorithm. In addition, it also provides RMS errors in each setting. Figure 7.2 (the 1th rows specifically show relatively small registration errors which accordingly indicate that the M-ICC algorithm is capable of producing successful results in the case of simple views with little occlusion. However, the outcomes entails inconsistency,
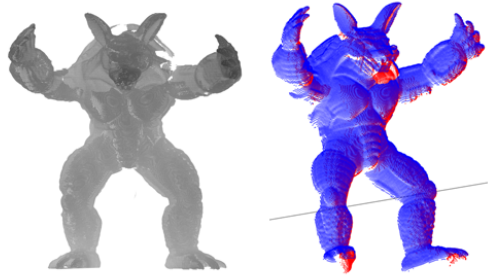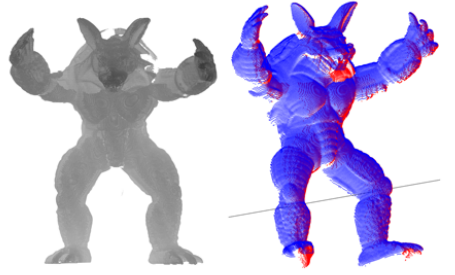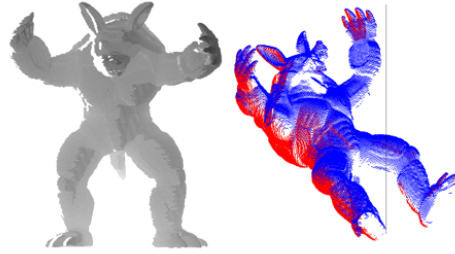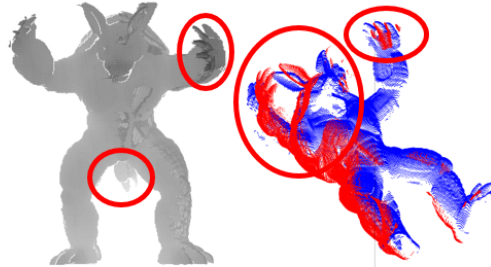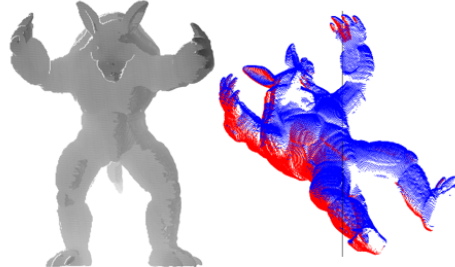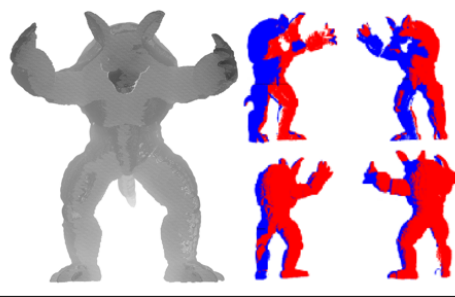
#	M-ICC	PA-HKS with MM-ICC
1		
	RMS error = 1.0999	RMS error = 0.290
2		
	RMS error = 3.169	RMS error = 0.281
3		
	RMS error = 3.289	RMS error = 0.233
4		
	RMS error = = 4.476 (Ave. of 4 pairs)	RMS error = 0.279 (Ave. of 4 pairs)

Figure 7.2: Results using Stanford Armadillo. Test setting (#1): 70°, 2 simple views (Less self-occlusion views). (#2): 70°, 2 complex views (More self-occlusion views). (#3): 90°, 2 complex views (#4): 90°, 4 complex views.

particularly in more challenging conditions, such as the complex views with more self-occlusion areas (2th rows) and with large rotation angles among multi-view range

scans (3th rows)). In these perplexing settings, the M-ICC algorithm is incapable of generating the accurate results, as illustrated in Figure 7.2 (the 2th, 3th row). Moreover, as demonstrated in Figure 7.2 (the 4th rows), the M-ICC algorithm is unable to provide successful outcomes in four pair-wise registrations mainly because the registered range data show significant mismatches and the average of the 4 pairs of registration RMS errors is quite big. On the contrary, the PA-MMICC algorithm is fully capable of obtaining stable and accurate matching outcomes for all four pair-wise registrations. In addition, the RMS results clearly indicate the effectiveness, accuracy and robustness of the proposed PA-MMICC algorithm. Overall, the proposed PA-MMICC algorithm is proven to be highly robust and accurate for the registration of the complex 3D objects which even involve large gaps of multi-view scans and significant occlusion in each scan.

Figure 7.3 presents the test results using another data set, Stanford Bunny. Similar to the test setting in Figure 7.2, (the 1th row represents the simple view which involves only 60-degree angle gap; in this setting, both of the M-ICC algorithm and the PA-MMICC algorithm provided successful results. However, in the complex views with more self-occlusion areas (2th rows), the M-ICC algorithm showed big RMS errors and failed to perform successful registration. In the 4th row, only two of the four pair-wise registrations from the M-ICC algorithm offered relatively successful outcomes whereas the other two provided significant mismatching results. On the contrary, the PA-MMICC algorithm was fully capable of obtaining stable and accurate matching outcomes for all the four pair-wise registrations. Therefore, these contrasting results clearly indicate that the proposed algorithm is highly robust in the different data set.

7.4 Results of AS-HKS with MM-ICC(AS-MMICC) algorithm

The previous section positively verified the robustness of the combination registration including PA-HKS and the MM-ICC algorithm(PA-MMICC); as shown, it was able
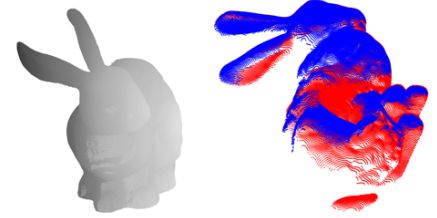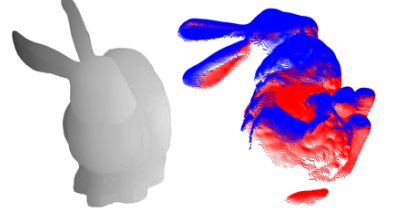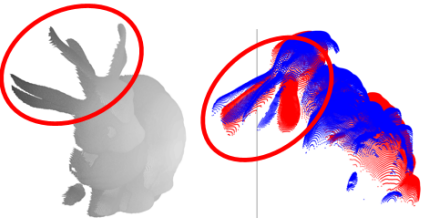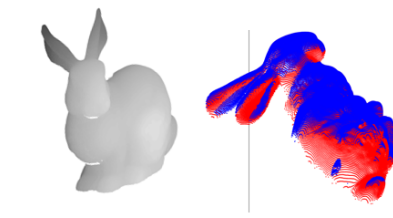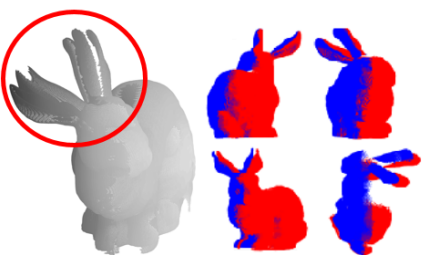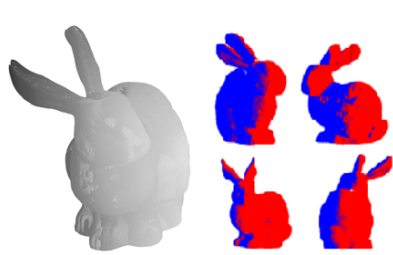
#	M-ICC	PA-HKS with MM-ICC
1		
	RMS error = 0.521	RMS error = 0.189
2		
	RMS error = 5.116	RMS error = 0.116
3		
	RMS error = 1.595 (Ave. of 4 pairs)	RMS error = 0.206 (Ave. of 4 pairs)

Figure 7.3: Results using Stanford Bunny. Test setting (#1): 60°, 2 simple views. (#2): 60°, 2 complex views. (#3): 90°, 4 complex views.

to provide promising outcomes despite tough and challenging conditions. Nevertheless, a limitation still remains in this combined approach in terms of the robust range; accordingly, we attempted to further maximize robustness to tougher and more challenging settings. In such an attempt, we proposed another combination registration algorithm which includes AS-HKS and the MM-ICC algorithm(AS-MMICC). Here in this section, we aim to verify the effectiveness of this newly proposed combination algorithm.

Setting(v1-v2)		Algorithms		
Angle Gap (degree)	Overlap Area (%)	M-ICC (without)	PA-MMICC (without)	AS-MMICC (without)
10°	87.80%	0.85	0.36	0.27
20°	78.39%	0.61	0.40	0.25
30°	68.33%	0.53	0.34	0.18
40°	58.78%	0.57	0.33	0.21
50°	49.80%	0.49	0.36	0.18
60°	41.64%	0.50	0.36	0.18
70°	33.68%	N/A	0.36	0.17
80°	25.29%	N/A	0.36	0.17
90°	15.11%	N/A	0.26	0.26
100°	12.38%	N/A	N/A	0.22
110°	11.79%	N/A	N/A	0.25
120°	9.21%	N/A	N/A	0.33
130°	6.70%	N/A	N/A	0.44
140°	3.57%	N/A	N/A	0.37
150°	1.38%	N/A	N/A	0.14
160°	0.47%	N/A	N/A	3.47

Table 7.1: Final Registration Errors: Comparison of the proposed algorithm and the previous algorithm using RMS errors (Tested in the "with no initialization" setting).

7.4.1   Registration errors according to angles

Table 7.1 compares the results of the AS-MMICC algorithm with the two previous ones including the M-ICC and the PA-MMICC using RMS errors in order to verify the effectiveness of the proposed algorithm. RMS errors consider corresponding points in overlapping areas, which have closest distance from different views. In addition, we also examined the case with no initialization in order to investigate how much angle gap between two different view range scan data could be recovered by each of the algorithms. For this process, the first view was fixed and the main rotation angle of the second view to the first one was measured at an interval of 10 degrees as an attempt to validate the maximum angle gap of each algorithm to obtain successful outcomes. As illustrated above, in case of the M-ICC algorithm, it was capable of recovering only up to 60 degrees of main rotation angles; beyond that degree, it failed to provide registration with higher RMS errors. The PA-MMICC algorithm showed a slightly better performance; it was able to recover up to 90 degrees with no initialization but it still failed operating registration of any further degree. On the contrary, the proposed algorithm using artificial symmetry 3D volume performed vastly successful recovery up to 160 degrees. One particularly important point to be emphasized here is that this AS-MMICC algorithm was capable of successful registration even with very little overlapping area between two input views: nearly closed to 0%. Moreover, it also presented higher accuracy with RMS error values as low as approximately 0.2.

About $0.1 \sim 0.2$ is ground truth RMS error which is the average of the distances between point-correspondences of only overlapping area in our test setting. Because we use points sets from the different range scan data, ground truth of RMSE is not zero in the Table 7.2. This result unmistakably indicates that the AS-MMICC algorithm enables us to obtaion highly robust registration with great accuracy, especially with no initialization and no overlapping areas of different range scan data. It is still true that RMS errors are not always a correct representative of the accurate registra-

tion, particularly in case that corresponding points are located closed to each other, not exactly on the same position due to using different data set. However, the corresponding points from different views are still capable of providing verification criteria mainly because RMS errors are calculated by the average of the distances between point-correspondences of only overlapping area and we compared RMS errors with ground truth RMS errors, which is not a zero.

Figure 7.4 illustrates the visual representation of the numbers from Table 7.1 above. Each row represents the differences according to different angle gaps, 30°, 60°, 90°, 120°, 160°, respectively. Each column demonstrates the actual outcomes from the 3 comparing algorithms; the first three columns illustrate two original range scan data, overlapping area, and initial pose from depth cameras whereas the last three show registration results of the M-ICC, the PA-MMICC, and the AS-MMICC algorithm. As clearly indicated in Table 7.1 and Figure 7.4, the M-ICC algorithm restrictively allowed registration when main rotation angle gap is less than 60° and the PA-MMICC algorithm up to 90°; on the contrary, the proposed algorithm was able to provide successful registration outcomes up to 160° with no initialization. Furthermore, in case of small angle gaps, the AS-MMICC algorithm presented highest accuracy compared the previous two. For instance, in 30°, the surface of the left leg part, which is the edge of range scan data, shows very smooth registration results. It is true that the AS-MMICC algorithm has relatively high RMS error value, 3.4567 in case of 160° and accordingly its result in Figure 7.4 shows rather uneven surface; nevertheless, it is still important to emphasize that the new algorithm illustrates more successful registration results compared to the other two algorithms.

7.4.2 Registration errors according to the number of views

Table 7.2 illustrates and compares the results of the three algorithms in two different settings. It shows maximum main rotation angle of recovery of each algorithm in

Figure 7.4: Results from Table 1 : Rows (30°,60°,90°,120°,160°), Columns (Two original range scan data, overlapping area(magenta), initial pose from the depth camera, M-ICC, PA-MMICC, AS-MMICC algorithm results, respectively).

two types of settings: the simple initial setting which entails more overlapping areas and less occlusion effect and the complex setting that involves less overlaps and more occlusion. The M-ICC algorithm was verified with initialization whereas the PA-MMICC and the AS-MMICC algorithms were inspected to compare RMS error

Setting			Comparing Algorithms			
Using Views	Angle Gap (degree)	Overlap Area (%)	M-ICC (with)	PA-MMICC (without)	AS-MMICC (without)	Ground truth
V1-V2	90°	15.11%	0.32	0.26	0.26	0.20
V2-V3	90°	29.80%	0.44	0.37	0.25	0.13
V3-V4	90°	27.89%	0.38	0.34	0.20	0.13
V1-V2	120°	9.21%	0.36	N/A	0.33	0.22
V1-V3	120°	9.70%	0.39	N/A	0.33	0.23

Table 7.2: Final registration errors: Comparison of the results of the 3 algorithms in different number of input (Tested in the "with" or "without" initialization settings).

values of ground truth data and final registration outcomes in the setting with no initialization. It is vital to indicate that in an attempt to compare final registration of multiple scan data, Table 7.2 uses the results of the "With initialization" case for the M-ICC mainly because it could perform registration only up to 60° in the setting with no initialization. As explained above, we performed registration using two different input range scan data; accordingly, RMS errors were calculated using average distance between two closest points in two range scan data. It should be noted that ground truth RMS error cannot be a zero primarily because geodesic distance between closest overlapping point clouds is calculated using two different range scan data.

Figure 7.5 visually represents the results of Table 7.2. Each row shows the results in cases that the number of input is four(90°) and three(120°), respectively. In addition, each column represents the outcomes of the M-ICC, the PA-MMICC, and the AS-MMICC algorithm. As explained above, in case of registration using 4 input range scan data, the AS-MMICC algorithm provided smaller values of RMS errors. In the M-ICC algorithm, the connection areas involve uneven surface even in the
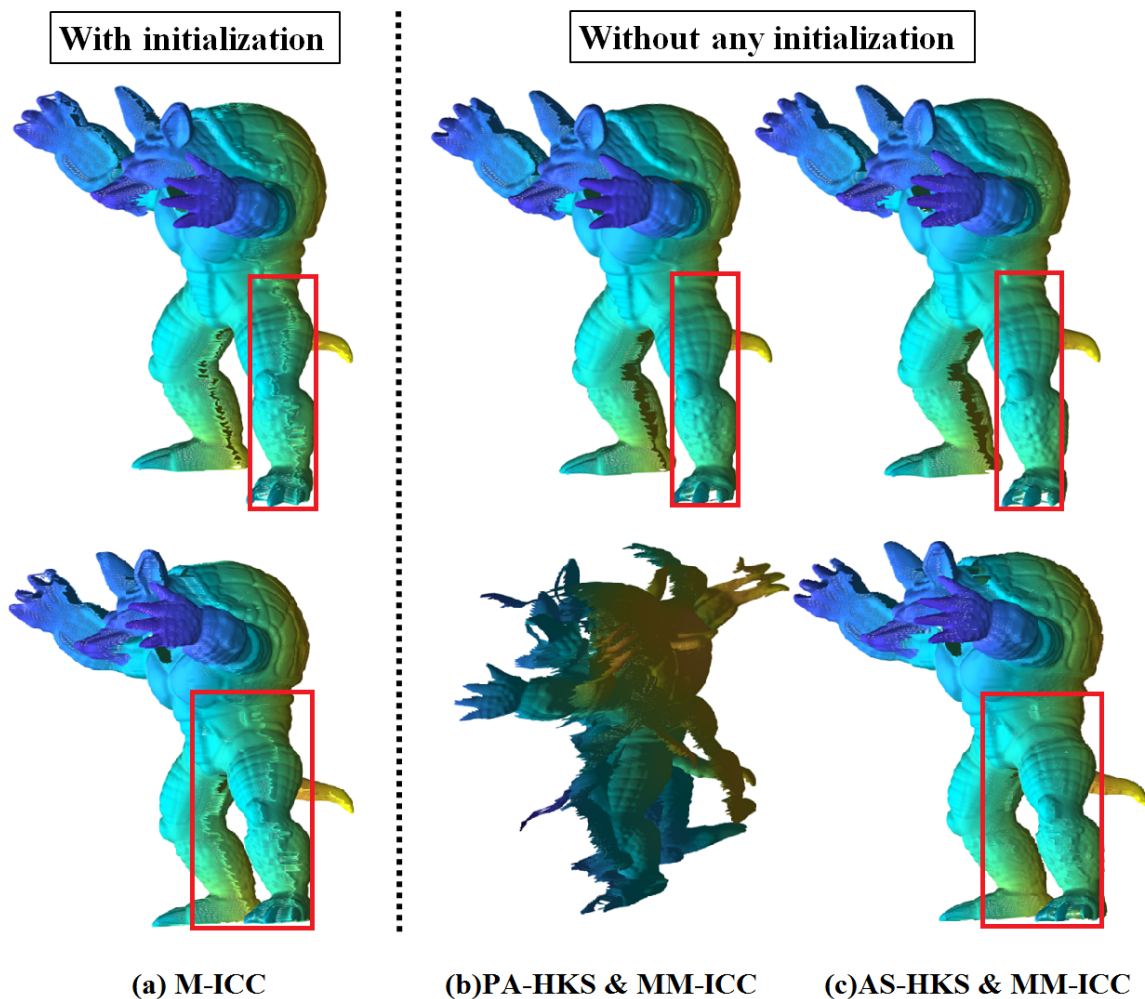
Figure 7.5: Results from different numbers of input in Table 2: Rows (4 inputs, 3 inputs), Columns (M-ICC, PA-HKS with MM-ICC, AS-HKS with MM-ICC results, respectively).

setting with initialization. Moreover, when using 3 input range scan, the PA-MMICC algorithm was unable to obtain successful registration outcomes. In both cases, the AS-MMICC algorithm proved its robustness and accuracy with outstanding outcomes even in ground truth RMS errors.

7.4.3 Registration errors according to the different inputs

Figures 7.6 and 7.7 illustrate the results of registration errors according to the different input data sets using Stanford Armadillo, Bunny, Happy Buddha, and Lucy. Four different views were considered in the test setting; and in case of M-ICC, 3D reconstruction was performed with initialization whereas PA-MMICC and AS-MMICC were tested with no initialization. In case of Armadillo, the average of RMS error in M-ICC was 4.476, which entails relatively larger values, in comparison with the RMS errors of PA-MMICC and AS-MMICC, 0.279 and 0.232, respectively. This difference can be also found visually in Figure 7.6. The results using Bunny demonstrate similar values with the average of RMS error in M-ICC as 1.595. This average is considerably higher than the RMS errors of PA-MMICC and AS-MMICC, 0.206 and 0.197, respectively. Especially, the ear part of the Bunny clearly indicates that M-ICC fails to perform registration. On the contrary, the proposed algorithms using artificial mesh were capable of eliciting successful registration outcomes.

In case of Happy Buddha, similarly, M-ICC showed the highest average value of RMS error whereas PA-MMICC and AS-MMICC illustrated lower average errors. As in Figure 7.7, the face and boundary part indicates that M-ICC entails lower accuracy in registration.

Finally, the results using Lucy also illustrate that M-ICC has larger average values of RMS errors in comparison to the proposed algorithms. To be more specific, the average RMS error of M-ICC was 1.057 based on those of 4 pairs of views, 3.498, 0.3705, 0.1494, 0.2118, respectively. As identified, one particular pair among the 4 pairs of views shows considerably higher error values; it is mainly because this pair entails more complex views due to self-occlusion. On the contrary, the two proposed algorithms overcome this complexity and show highly accurate registration outcomes.

In conclusion, this experimental test result clearly validates that the proposed algorithms are able to successfully perform 3D reconstruction despite the different
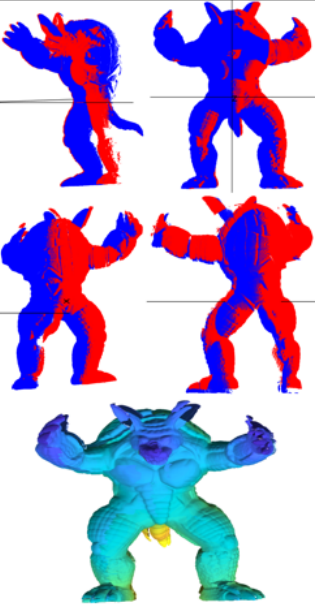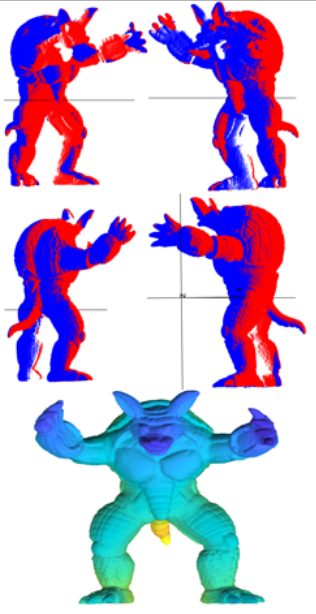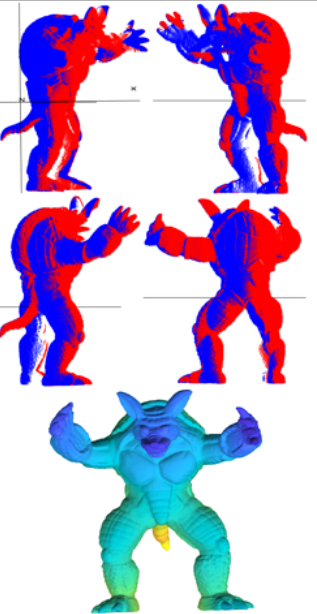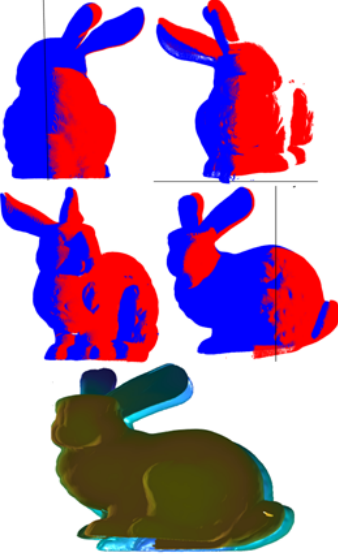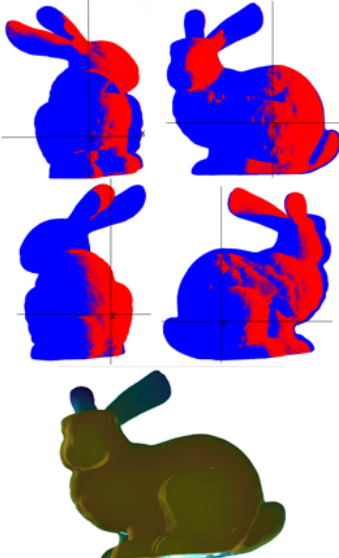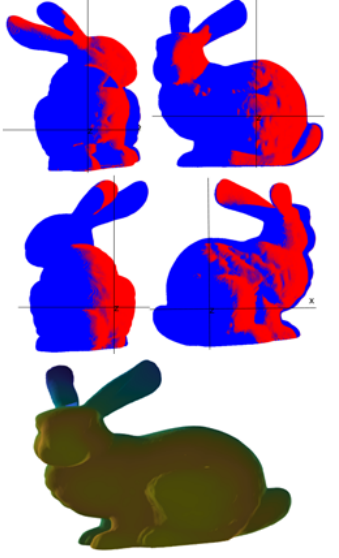
M-ICC (with)	PA-MMICC (without)	AS-MMICC (without)
Test Setting : 90° , 4 Complex views, Stanford Armadillo		
RMS error = 4.476 (Ave. of 4 pairs)	RMS error = 0.279 (Ave. of 4 pairs)	RMS error = 0.232 (Ave. of 4 pairs)
Test Setting : 90° , 4 Complex views, Stanford Bunny		
RMS error = 1.595 (Ave. of 4 pairs)	RMS error = 0.206 (Ave. of 4 pairs)	RMS error = 0.197 (Ave. of 4 pairs)

Figure 7.6: Results from different input data sets (Stanford Armadillo, Bunny).

input data sets.
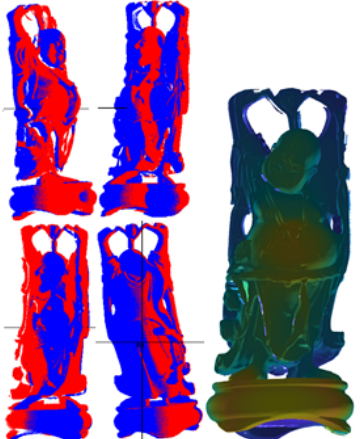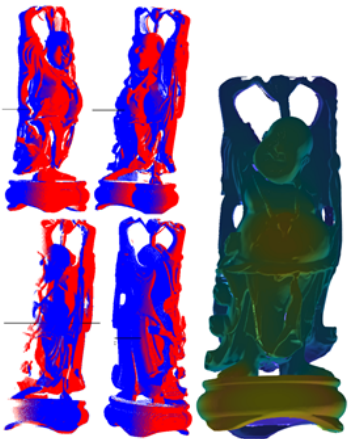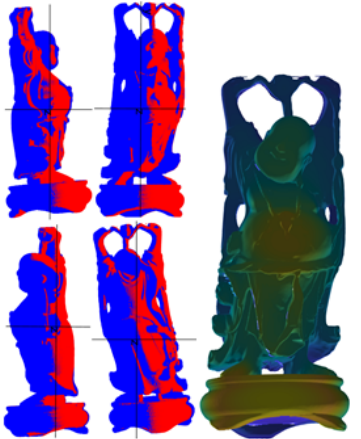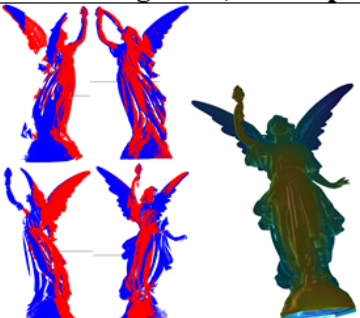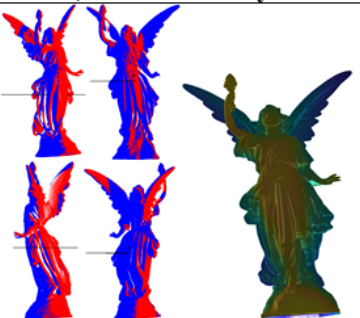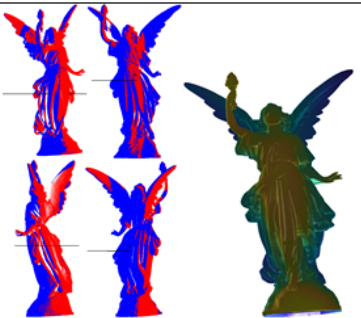
M-ICC (with)	PA-MMICC (without)	AS-MMICC (without)
Test Setting : 90° , 4 Complex views, Stanford Happy Buddha		
RMS error = 3.284 (Ave. of 4 pairs)	RMS error = 0.4002 (Ave. of 4 pairs)	RMS error = 0.3183 (Ave. of 4 pairs)
Test Setting : 90° , 4 Complex views, Stanford Lucy		
RMS error = 1.057 (Ave. of 4 pairs)	RMS error = 0.1847 (Ave. of 4 pairs)	RMS error = 0.1831 (Ave. of 4 pairs)

Figure 7.7: Results from different input data sets (Stanford Happy Buddha, Lucy).

7.4.4 Registration errors according to Main parameter

The proposed algorithms entail a main parameter which distinguishes depth discontinuity of each range scan data. The depth discontinuity parameter finds a self-occlusion area of each range scan from different views in order to avoid possible incorrect correspondences among input range data. This parameter is also used to determine the shape of the artificial 3D mesh in the coarse registration stage and the contour and occlusion points used in the pruning stage of the fine registration. Therefore, the parameter has a huge influence on accuracy of registration outcomes;

that is, if a wrong parameter is selected, registration fails. There are several affecting factors; in other words, an optical parameter value varies according to the shape of a target object, to degree of occlusion in view directions, and particularly to the scale of a target. Hence, identifying the sensitivity of the parameter over different models is important. In order to achieve this, we utilized a similar scale of a target to obtain an optimal parameter threshold value.
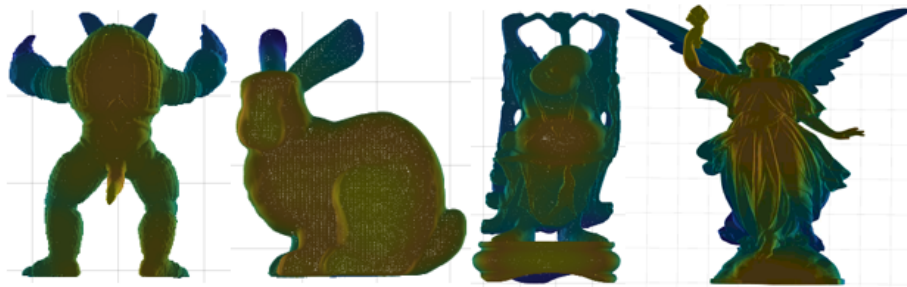
Figure 7.8: The Range of appropriate depth continuous thresholds for the four models

Figure 7.8 shows the range of proper threshold values to obtain correct registration results of 4 different testing data sets (Armadillo, Bunny, Buddha, and Lucy) in the similar scale of the target. As mentioned above, an optimal threshold value of discontinuity varies according to the scale of input data and view directions. Identifying a threshold is one of the challenges of the proposed algorithms.

In our experimental test setting, we set 160 for the longest dimension of the targets to use the same scale. The optimal range identified for different data sets are as follows: 5-7 for Armadillo, 4-10 for bunny, 4-8 for Buddha, and 6-9 for Lucy.

When similar values of an optimal threshold are given, accuracy of the registration outcomes decreases; and when choosing far smaller numbers than the optimal value, the proposed algorithms will fail.

7.4.5 Registration of an Extreme self-occluded 3D model

This section discusses the limitation of possible registration coverage of our proposed algorithm. One extremely large self-occlusion model, Stanford dragon is adopted in order to examine the proposed algorithms and its registration outcome was unsuccessful.

(a)   (b)   (c)
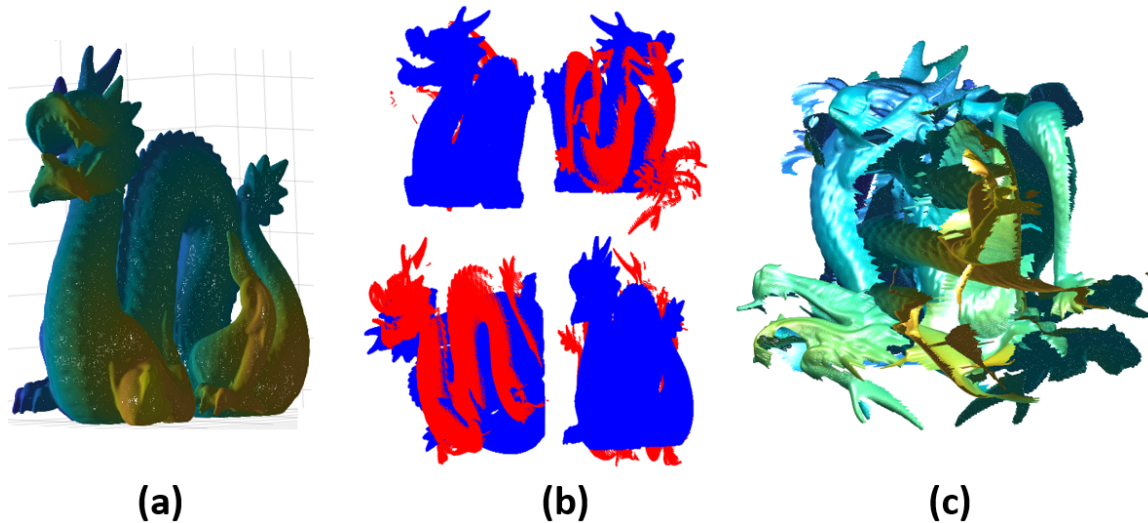
Figure 7.9: Results of dragon model: (a) 3D Stanford dragon; (b) four pair-wise registration results; (c) Final registration result of 4 inputs.

In Figure 7.9, (a) is the original 3D Stanford dragon model and (b) refers four pair-wise registrations from the AS-MMICC algorithm and shows significant mismatching results and (c) is the final registration results of 4 input range scan that are wrong. The main reason of this unsuccessful outcome is that the dragon model has a highly complicated 3D shape that will have significant self-occlusion areas under most perspectives. Therefore, through the projection of PA-HKS and the symmetry

of AS-HKS, it is incapable of generating correct artificial 3D mesh. Further, the body area of the dragon model has a long and winding shape which entails global similarity. Accordingly, when using symmetry 3D mesh, the AS-HKS algorithm fails to identify the difference of the object surface with this globally similar information.

7.5   Discussion

We proposed the two combination registration algorithms for multiple main rotation range scan data, which entails extremely little overlapping, with no initialization; that is, PA-MMICC and AS-MMICC. In conclusion, on the basis of RMS error values, the PA-MMICC algorithm, in comparison with the M-ICC, showed highly robust registration without any initialization. In addition, this PA-MMICC was also able to perform fast registration through fast generating artificial 3D mesh using projection, when comparing with AS-MMICC. The other proposed algorithm, the AS-MMICC was effectively capable of providing improvement in comparison to the PA-MMICC, on the basis of more accurate artificial 3D mesh. The main and significant contribution of the proposed algorithm should be that it is more robust for the diverse initial scan directions in obtaining accurate registration results. Although the PA-MMICC algorithm illustrated a good registration result, a limitation was also identified. It was not able to operate registration in the complex settings that limit to certain angles or that entail more occlusion; on the contrary, the AS-MMICC algorithm completely overcomes this limitation. Further, it even allows successful registration in complex settings of 120 degrees or higher. The PA-MMICC algorithm was also able to perform registration of the scan data with yaw rotation only up to the allowed maximum angle as 90 degrees. In other words, at least 4 input data were compulsorily required to generate one full covered 3D model which can cover 360 degrees. However, the AS-MMICC algorithm enables us to operate registration up to 120 degree or more angle between input scan data. Further this advancement allows us to use exclusively

the 3 input scan data to generate one full covered 3D model.

CHAPTER VIII

Conclusions and Future Research

8.1 Conclusions

In this dissertation, we made an attempt to address three research challenge in the field of 3D reconstruction using registration. The first challenge considered was registration of the 3D range scan without any pre-knowledge given, such as initialization or calibration. The second challenge was how to diminish the amount of the required minimum overlapping to guarantee successful registration results. The last but not least research challenge was how to effectively advance accuracy of 3D registration.

To resolve these research issues and challenges, the present dissertation research proposed the combination registration algorithm with the two-step coarse registration and the fine registration. In regard to coarse registration, we proposed two different algorithms, including the Partial Artificial Heat Kernel Signature (PA-HKS) algorithm and the Artificial Symmetry Heat Kernel Signature (AS-HKS) algorithm, as an important attempt to tackle the first challenge, the 'with no initialization' issue. Especially, the AS-HKS algorithm is a technique for coarse registration by using an artificial symmetry volume mesh; in addition to its robust outcome, this algorithm also provided a curial clue to resolve the second challenge, which considers a decrease of the minimum requirement of the overlapping area. As a subsequent step after the coarse registration, we performed fine registration by the newly proposed Modified Multi-view Iterative Closest Contour(MM-ICC) algorithm. This new MM-ICC algorithm was employed to mainly address and successfully provide a resolution to the third challenge, enhancing accuracy.

- In the current dissertation research, we proposed two algorithms, including the PA-HKS and the AS-HKS to perform coarse registration for the multiple partial range scan. The partial range scan data involves the surface information in the visible area; therefore, it is difficult to find correspondences between the partial range scans. In order to find the corresponding feature descriptors from the partial data, we suggested a new 3D reconstruction algorithm on the basis of the artificial volume 3D mesh and Heat kernel signature (HKS) which is generated from that artificial volume 3D mesh. To generate the artificial volume, we proposed two different methods, the PA-HKS and the AS-HKS. In the PA-HKS, the range scan data was projected to the plane and then connected to the original range data through mesh. On the other hand, the AS-HKS algorithm attempted to generate the artificial 3D volume mesh using symmetry of the visible and invisible surface. These two proposed ideas demonstrated successfully registration outcomes for coarse registration; subsequently, the results of these two coarse registration algorithms were adopted to operate the next step, fine registration using the MM-ICC. The PA-HKS algorithm was able to perform registration of scan data of yaw rotation only up to the allowed maximum angle as 90 degrees. In other words, the 4 input data were mandatorily required to successfully generate one fully covered 3D model which can deal with up to 360 degrees. However, the newly proposed algorithm allowed prosperous outcomes with extended angles over 120 degrees or higher between two input scan data, which qualifies us to request the less number of the input, specifically merely 3 input scan data to generate one full covered 3D model.

- The AS-HKS algorithm was capable of performing successful registration using the multi-view range scans which have extremely little overlaps. The artificial symmetry 3D volume mesh based on the symmetry idea is able to provide both global and local features of each range scan data in order to correctly identify

97

correspondences among the partial 3D range scan data. The results were highly positive even in case of 1-2% overlapping areas. This extremely small amount of overlapping areas is very inspiring particularly because the previous studies have demonstrated that at least 45-50% of overlapping regions are required to guarantee successful registration outcomes.

- As an attempt to address the last challenge and advance accuracy of the registration results, we proposed the Modified Multi-view Iterative Closest Contour(MM-ICC) algorithm. This newly proposed algorithm entails the additional supplementary pruning step in order to effectively remove the supposedly invisible points in the predicted contours. This third pruning phase serves as a powerful support in the second-round re-registration. As a result, it considerably improves the overall quality of the final registration outcomes.

In summary, on the basis of the methodological phases explained above, the present dissertation research proposed a new and robust technique for fully automatic 3D Reconstruction through registration of 3D range scans with no initialization. Consequently, this proposed algorithm successfully addressed and resolved the existing research challenges.

8.2 Future Research

Our future research will focus primarily on two major issues. One of our future research directions is centered on how to apply this registration under noise condition and the other research direction should be headed to the extended application of the proposed registration algorithm for reconstruction of the non-rigid objects. Each of these two directions will be discussed in more detail in the following section.

- In our current dissertation research, we proposed the robust registration algorithm with a consideration of input data without noise. Grounded on the fact that

the MM-ICC algorithm successfully performs registration on the basis of only the pruned contours which are derived from the observed and predicted range scan, not based on the entire surface, this newly proposed algorithm is capable of providing highly accurate results using extremely low overlap range scans input. Nevertheless, there exists a limitation. In the research condition including high noise, the proposed algorithm is not expected to demonstrate successful registration. Mainly due to the fact that the current algorithm utilized the limited amount of surface information, it entails high sensitivity on a small quantity of noise. Therefore, as one of the important future research direction, it should be considered to deal with the particular condition including noise and further advance the current algorithm to show more robustness in the challenging settings.

- Another limitation of the proposed algorithm leads to the second research direction. The proposed algorithm is able to provide successful outcomes with high accuracy in 3D registration exclusively for the rigid-3D model. Accordingly, the subsequent research step should deal with this limitation for the non-rigid 3D Reconstruction without correspondences. Currently, a number of previous studies on 3D reconstruction have made great deal of efforts to suggest a robust registration algorithm for reconstructing deformable shapes [90, 91]. Some of these studies have provided some process and proposed performing 3D registration on the template. However, more research is still required for more robust and effective 3D registration. Accordingly, we expect our proposed algorithm in this dissertation is highly possible to be extended to make new progress by operating registration for the non-rigid object without templates. This proposed algorithm, as proven so far, entails a number of robust features in successfully detecting correspondences on the basis of the artificial 3D volume; thus, it is expected to extend the matching algorithm which is capable of providing promising 3D reconstruction of deformable objects.

REFERENCES

[1] Z. Zhang, "Microsoft kinect sensor and its effect," *IEEE Multimedia*, vol. 19, pp. 4–10, 2012.

[2] S. Rogge and C. Hentschel, "A multi-depth camera capture system for point cloud library," in *Proc. of IEEE Fourth International Conference on Consumer Electronics*, pp. 50–54, 2014.

[3] A. Khan, F. Moideen, J. Lopez, W. L. Khoo, and Z. Zhu, "Kindectect: Kinect detecting objects," *International Conference on Computers for Handicapped Persons, Part II, LNCS*, vol. 7383, pp. 588–595, 2012.

[4] F. Weichert, D. Bachmann, B. Rudak, and D. Fisseler, "Analysis of the accuracy and robustness of the leap motion controller," *Sensors (Basel)*, vol. 13, pp. 6380–6393, 2013.

[5] J. Sun, M. Ovsjanikov, and L. Guibas, "A concise and provably informative multi-scale signature based on heat diffusion," in *Proc. of Eurographics Symposium on Geometry Processing*, vol. 28, pp. 1383–1392, 2009.

[6] D. Chetverikov, D. Svirko, and D. Stepanov, "The trimmed iterative closest point algorithm," in *16th International Conference on Pattern Recognition*, vol. 3, pp. 1–4, 2002.

[7] H.-Y. Lin, *Computer Vision Techniques for Complete 3D Model Reconstruction*. PhD thesis, State University of New York at Stony Brook, 2002.

[8] M. Ma, H. Zheng, and H. Lallie, "Virtual reality and 3d animation in forensic visualization," *Journal of forensic sciences*, vol. 55, p. 1227–1231, 2010.

[9] N. Dai, J. Hu, and H. Liu, "3d simulation modeling of the tooth wear process," *PLoS ONE*, vol. 10, 2015.

[10] J. Treil, J. Braga, J.-M. Loubes, E. Maza, J.-M. Inglese, J. Casteigt, and B. Waysenson, "3d tooth modeling for orthodontic assessment," *Seminars in Orthodontics*, vol. 15, pp. 42–47, 2009.

[11] A. Budroni and J. Boehm, "Automated 3d reconstruction of interiors from point clouds," *International Journal of Architectural Computing*, vol. 8, pp. 55–73, 2010.

[12] P. Henry, M. Krainin, E. Herbst, X. Ren, and D. Fox, "Rgb-d mapping: Using depth cameras for dense 3d modeling of indoor environments," *Experimental Robotics, Springer Tracts in Advanced Robotics*, vol. 79, pp. 477–491, 2014.

[13] H. Surmann, A. Nüchter, and J. Hertzberg, "An autonomous mobile robot with a 3d laser range finder for 3d exploration and digitalization of indoor environments," *Robotics and Autonomous Systems*, vol. 45, pp. 181–198, 2003.

[14] D. Baltieri, R. Vezzani, and R. Cucchiara, "3dpes: 3d people dataset for surveillance and forensics," *J-HGBU '11 Proceedings of the 2011 joint ACM workshop on Human gesture and behavior understanding*, pp. 59–64, 2011.

[15] A. Chowdhury, R. Chellappa, S. Krishnamurthy, and T. Vo, "3d face reconstruction from video using a generic model," *ICME*, 2002.

[16] B. Allen, B. Curless, and Z. Popovic, "Articulated body deformation from range scan data," *ACM Transactions on Graphics*, vol. 21, pp. 612–619, 2002.

[17] D. Roetenberg, H. Luinge, and P. Slycke, "Xsens mvn: Full 6dof human motion tracking using miniature inertial sensors," *Xsens Technologies BV*, 2009.

[18] T. B. Moeslud and E. Granum, "A survey of computer vision-based human motion capture," *Computer Vision and Image Understanding*, vol. 81, pp. 231–268, 2001.

[19] P. Axelsson, "Processing of laser scanner data—algorithms and applications," *ISPRS Journal of Photogrammetry and Remote Sensing*, vol. 54, pp. 138–147, 1999.

[20] V. Blanz and T. Vetter, "A morphable model for the synthesis of 3d faces," *SIGGRAPH '99 Proceedings of the 26th annual conference on Computer graphics and interactive techniques*, pp. 187–194, 1999.

[21] U. Buck, S. Naether, M. Braun, S. Bolliger, H. Friederich, C. Jackowski, E. Aghayev, A. Christe, P. Vock, R. Dirnhofer, and M. J. Thali, "Application of 3d documentation and geometric reconstruction methods in traffic accident analysis: With high resolution surface scanning, radiological msct/mri scanning and real data based animation," *Forensic Science International*, vol. 170, pp. 20–28, 2007.

[22] P. Treleaven and J. Wells, "3d body scanning and healthcare applications," *Computer*, vol. 40, pp. 28–34, 2007.

[23] A. 3D, "Artec eva 3d scanner," 2017.

[24] J. Winder and R. Bibb, "Medical rapid prototyping technologies: State of the art and current limitations for application in oral and maxillofacial surgery," *Journal of Oral and Maxillofacial Surgery*, vol. 63, pp. 1006–1015, 2005.

[25] J. Berkley, G. Turkiyyah, D. Berg, M. Ganter, and S. Weghorst, "Real-time finite element modeling for surgery simulation: An application to virtual suturing," *IEEE Transactions on Visualization and Computer Graphics*, vol. 10, pp. 314–325, 2004.

[26] X. P. LIVE, "Xtion pro live."

[27] D. Systems, "Sense 3d scanner."

[28] C. A. Technology, "Go!scan," 2017.

[29] Z. Zhang, "A flexible new technique for camera calibration," *IEEE Transactions on Pattern Analysis and Machine Intelligence*, vol. 22, pp. 1330–1334, 2000.

[30] R. B. Rusu, N. Blodow, and M. Beetz, "Fast point feature histograms (fpfh) for 3d registration," *2009 IEEE International Conference on Robotics and Automation*, pp. 3212–3217, 2009.

[31] A. Makadia, A. Patterson, and K. Daniilidis, "Fully automatic registration of 3d point clouds," in *IEEE Computer Society Conference on Computer Vision and Pattern Recognition*, 2006.

[32] D. F. Huber and M. Hebert, "Fully automatic registration of multiple 3d data sets," *Image and Vision Computing*, vol. 21, pp. 637–650, 2001.

[33] W. Chang and M. Zwicker, "Automatic registration for articulated shapes," in *Proc. of Eurographics Symposium on Geometry Processing*, vol. 27, pp. 1459–1468, 2002.

[34] F. Bernardini and H. Rushmeier, "The 3d model acquisition pipeline," *Computer Graphics Forum*, vol. 21, pp. 149–172, 2002.

[35] A. Hilton, A. J. Stoddart, J. Illingworth, and T. Windeatt, "Reliable surface reconstruction from multiple range images," *European Conference on Computer Vision 1006*, pp. 117–126, 1996.

[36] C. Baillard, C. Schmid, A. Zisserman, and A. Fitzgibbon, "Automatic line matching and 3d reconstruction of buildings from multiple views," *ISPRS Conference on Automatic Extraction of GIS Objects from Digital Imagery, IAPRS*, vol. 32, pp. 69–80, 1999.

[37] Z. Zhang, "Flexible camera calibration by viewing a plane from unknown orientations," *Proceedings of the 7th IEEE Conference on Computer Vision*, vol. 2, 1999.

[38] R. Tsai and R. Lenz, "A new technique for fully autonomous and efficient 3d robotics hand/eye calibration," *IEEE Transactions on Robotics and Automation*, vol. 5, pp. 345–358, 1989.

[39] F. Remondino and C. Fraser, "Digital camera calibration method: Considerations and comparisons," *ISPRS Commission V Symposium 'Image Engineering and Vision Metrology'*, pp. 266–272, 2006.

[40] J. Tong, J. Zhou, L. Liu, Z. Pan, and H. Yan, "Scanning 3d full human bodies using kinects," *IEEE Transactions on Visualization and Computer Graphics*, vol. 18, pp. 643–650, 2012.

[41] G. Wu, D. Li, Y. Zhong, and P. Hu, "A study on improving the calibration of body scanner built on multiple rgb-depth cameras," *International Journal of Clothing Science and Technology*, vol. 29, pp. 314–329, 2017.

[42] J.-M. Lu and M.-J. J. Wang, "Automated anthropometric data collection using 3d whole body scanners," *Expert Systems with Applications*, vol. 35, pp. 407–414, 2008.

[43] J. Shotton, A. Fitzgibbon, M. Cook, T. Sharp, M. Finocchio, R. Moore, A. Kipman, and A. Blake, "Real-time human pose recognition in parts from single depth images," *IEEC Conference on Computer Vision and Pattern Recognition (CVPR)*, pp. 1297–1304, 2011.

[44] S. Izadi, D. Kim, O. Hilliges, D. Molyneaux, R. Newcombe, P. Kohi, J. Shotton, S. Hodges, D. Freeman, A. Davison, and A. Fitzgibbon, "Kinectfusion: Real-time 3d reconstruction and interaction using a moving depth camera," *UIST'11 Proceedings of the 24th Annual ACM Symposium on User Interface Software and Technology*, pp. 559–568, 2011.

[45] "Microsoft corp. redmond wa. kinect for xbox 360,"

[46] R. A. Newcombe, S. Izadi, O. Hilliges, D. Kim, A. J. Davison, P. Kohi, J. Shotton, S. Hodges, and A. Fitzgibbon, "Kinectfusion: Real-time dense surface mapping and tracking," *10th IEEE International Symposium on Mixed and Augmented Reality*, pp. 127–136, 2011.

[47] C. Chow, H. Tsui, and T. Lee, "Surface registration using a dynamic genetic algorithm," *Pattern Recognition*, vol. 37, pp. 105–117, 2004.

[48] P. Besl and N. McKay, "A method for registration of 3-d shapes," *IEEE Transactions on Pattern Analysis and Machine Intelligence*, vol. 14, pp. 239–255, 1992.

[49] M. Ye, X. Wang, R. Yang, L. Ren, and M. Pollefeys, "Accurate 3d pose estimation from a single depth image," *IEEE Conference on Computer Vision (ICCV)*, pp. 731–738, 2011.

[50] S. Brandao, J. Costeria, and M. Veloso, "The partial view heat kernel descriptor for 3d object representation," in *Proc. of ICRA 2014*, vol. 28, 2014.

[51] M. Bronstein and I. Kokkinos, "Scale-invariant heat kernel signatures for non-rigid shape recognition," pp. 1704–1711, 2010.

[52] R. Wang, J. Choi, and G. Medioni, "3d modeling from wide baseline range scans using contour coherence," in *Proceedings of CVPR'14*, pp. 1–8, 2014.

[53] A. Myronenko and X. Song, "Point set registration: Coherent point drift," *IEEE Transactions on Pattern Analysis and Machine Intelligence*, vol. 32, pp. 2262–2275, 2010.

[54] A. Myronenko, X. Song, and M. Carreria-Perpinan, "Non-rigid point set registration: Coherent point drift," *Advances in Neural Information Processing Systems 19*, 2006.

[55] P. Scovanner, S. Ali, and M. Shah, "A 3-dimensional sift descriptor and its application to action recognition," *MM'07 Proceedings of the 15th ACM International Conference on Multimedia*, pp. 357–360, 2007.

[56] I. Sipiran and B. Bustos, "Harris 3d: A robust extension of the harris operator for interest point detection on 3d meshes," *The Visual Computer: International Journal of Computer Graphics-Special Issues on 3DOR 2010*, vol. 27, pp. 963–976, 2011.

[57] A. Segal, D. Haehnel, and S. Thrun, "Genearlized-icp," in *Proc. of Robotics: Science and Systems*, 2009.

[58] J. Dong, Y. Peng, S. Ying, and Z. Hu, "Lietricp: An improvement of trimmed iterative closest point algorithm," *Neurocomputing*, vol. 140, pp. 67–76, 2014.

[59] D. Chetverikov, D. Svirko, D. Stepanov, and P. Krsek, "The trimmed iterative closest point algorithm," *16th International Conference on Pattern Recognition*, vol. 3, 2002.

[60] H. Chui and A. Rangarajan, "A feature registration framework using mixture models," *Mathematical Methods in Biomedical Image Analysis*, pp. 190–197, 2000.

[61] S. Rusinkiewicz and M. Levoy, "Efficient variants of the icp algorithm," in *Proc. of 3rd International Conference on 3-D Digital Imaging and Modeling*, pp. 145–152, 2001.

[62] V. Golyanik, B. Taetz, G. Reis, and D. Stricker, "Extended coherent point drift algorithm with correspondence priors and optimal subsampling," *IEEE Winter Conference on Applications of Computer Vision (WACV)*, pp. 1–9, 2016.

[63] D. Aiger, N. Mitra, and D. Cohen-Cor, "4-points congruent sets for robust pairwise surface registration," *ACM Transactions on Graphics (TOG)*, vol. 27, 2008.

[64] S. Shah, F. Bennamoun, F. Boussaid, and A. El-Sallam, "3d-div: A novel local surface descriptor for feature matching and pairwise range image registration," in *2013 IEEE International Conference on Image Processing*, pp. 2934–2938, 2013.

[65] Y. Guo, F. Sohel, M. Bennamoun, M. Lu, and J. Wan, "Trisi: A distinctive local surface descriptor for 3d modeling and object recognition," in *GRAPP 2013: International Conference on Computer Graphics Theory and Applicaitons*, pp. 86–93, 2013.

[66] C. Tardif, A. Schafer, M. Waehnert, J. Dinse, R. Turner, and P. Bazin, "Multi-contrast multi-scale surface registration for improved alignment of cortical areas," *Neuroimage*, vol. 111, pp. 107–122, 2015.

[67] I. Sipiran and B. Bustos, "A robust 3d interest points detector based on harris operator," in *Proceedings of Eurographics Workshop on 3D Object Retrieval*, pp. 7–14, 2010.

[68] H. Dutagaci, C. Cheung, and A. Godil, "Evaluation of 3d interest point detection techniques via human-generated ground truth," vol. 28, pp. 901–917, 2012.

[69] R. Xia, J. Zhao, and Y. Liu, "A robust feature-based registration method of multimodal image using phase congruency and coherent point drift," vol. 8919, 2013.

[70] C. Harris and M. Stephens, "A combined corner and edge detector," *Proceeding of the 4th Alvey Vision Conference*, p. 147–151, 1988.

[71] A. Bronstein, M. Bronstein, B. Bustos, U. Castellani, M. Crisani, B. Falcidieno, L. J. Guibas, I. Kokkinos, V. Murino, M. Ovsjanikov, G. Patane, I. Sipiran, M. Spagnuolo, and J. Sun, "Shrec 2010: Robust feature detection and description benchmark," *In Proc. Eurographics Workshop on 3D Object Retrieval*, p. 79–86, 2010.

[72] A. J. Davison, I. D. Reid, N. D. Molton, and O. Stasse, "Monoslam: Real-time single camera slam," *IEEE Transactions on Pattern Analysis and Machine Intelligence*, vol. 29, pp. 1052–1067, 2007.

[73] N. Fioraio and K. Konolige, "Realtime visual and point cloud slam," 2011.

[74] M. Y. Yang, Y. Cao, W. Förstner, and J. McDonald, "Robust wide baseline scene alignment based on 3d viewpoint normalization," *ISVC 2010: Advances in Visual Computing, Part I, LNCS 6453*, pp. 654–665, 2010.

[75] H. Du, P. Henry, X. Ren, M. Cheng, D. B. Goldman, S. M. Seitz, and D. Fox, "Interactive 3d modeling of indoor environments with a consumer depth camera," *Proceedings of the 13th International Conference on Ubiquitous Computing*, pp. 75–84, 2011.

[76] Y. Liu, Q. Dai, and W. Xu, "A point-cloud-based multiview stereo algorithm for free-viewpoint video," *IEEE Transactions on Visualization and Computer Graphics*, vol. 16, 2010.

[77] C. Strecha, T. Tuytelaars, and L. V. Gool, "Dense matching of multiple wide-baseline views," *ICCV'03 Proceedings of the 9th IEEE International Conference on Computer Vision*, vol. 2, pp. 1194– 1201, 2003.

[78] R. A. Newcombe and A. J. Davison, "Live dense reconstruction with a single moving camera," *IEEE Conference on Computer Vision and Pattern Recognition (CVPR)*, pp. 1498–1505, 2010.

[79] T. Stoyanov, M. Magnusson, H. Andreasson, and A. J. Lilienthal, "Fast and accurate scan registration through minimization of the distance between compact 3d ndt representations," *The International Journal of Robotics Research*, vol. 31, pp. 1377–1393, 2012.

[80] A. Grigor'yan, "Heat kernels on weighted manifolds and applications," *Contemporary Mathematics*, vol. 398, pp. 93–192, 2006.

[81] R. Ahdid, S. Safi, M. Fakir, and B. Manaut, "Geodesic distance on riemannian manifold using jacobi iterations in 3d face recognition system," *International Journal of Informatics and Communication Technology*, vol. 6, pp. 10–19, 2017.

[82] "Matlab toolbox graph," pp. https://www.mathworks.com/matlabcentral/fileexchange/5355–toolbox–graph?requestedDomain=www.mathworks.com.

[83] S. Katz and A. Tal, "Hierarchical mesh decomposition using fuzzy clustering and cuts," *ACM Transactions on Graphics: Proceedings of AC SIGGRAPH 2003*, vol. 22, pp. 954–961, 2003.

[84] "The stanford 3d scanning repository," 2014.

[85] E. O. S. Guide, "Anatomical plane," pp. http://www.scientistcindy.com/anatomy–exam–one–study–guide.html.

[86] T. Saunders, "Everything you ever wanted to know about breast fat but were afraid to ask," *Diverse Perspectives on Science and Medicine*, pp. http://blogs.plos.org/obesitypanacea/2014/10/23/everything–you–ever–wanted–to–know–about–breast–fat–but–were–afraid–to–ask–2/, 2012.

[87] H. Li, B. S. Manjunath, and S. K. Mitra

[88] C. J. Willmott, S. G. Ackleson, R. E. Davis, J. J. Feddema, K. M. Klink, D. R. Legates, J. O'Donnell, and C. M. Rowe, "Statistics for the evaluation and comparison of model," *Journal of Geophysical Research*, vol. 90, pp. 8995–9005, 1985.

[89] C. J. Willmott and K. Matsuura, "Advantages of the mean absolute error (mae) over the root mean square error (rmse) in assessing average model performance," *Climate Research*, vol. 30, 2005.

[90] M. Zollhofer, M. Nießner, S. Izadi, C. Rehmann, C. Zach, M. Fisher, C. Wu, A. Fitzgibbon, C. Loop, C. Theobalt, and M. Stamminger, "Real-time non-rigid reconstruction using an rgb-d camera," *ACM Transactions on Graphics (TOG) - Proceedings of ACM SIGGRAPH 2014*, vol. 33, 2014.

[91] R. Yu, C. Russell, N. D. F. Campbell, and L. Agapito, "Direct, dense, and deformable: Template-based non-rigid 3d reconstruction from rgb video," *2015 IEEE International Conference on Computer Vision (ICCV)*, pp. 918–926, 2015.

VITA

JUNGJAE YIM

Candidate for the Degree of

Doctor of Philosophy

Dissertation: FULLY AUTOMATIC 3D OBJECT RECONSTRUCTION FROM MULTI-VIEW RANGE SCAN DATA

Major Field: Electrical Engineering

Biographical:

Education:

Completed the requirements for the Doctor of Philosophy in Electrical Engineering at Oklahoma State University, Stillwater, Oklahoma in Dec, 2017.

Completed the requirements for the Master of Science in Electrical Engineering at Oklahoma State University, Stillwater, Oklahoma in 2009.

Completed the requirements for the Bachelor of Information Communication Engineering at Hanbat National University, Daejeon, South Korea in 2007.

Experience:

Graduate Research Assistant in Visual Computing and Image Processing Lab (VCIPL), School of Electrical and Computer Engineering, Oklahoma State University, January 2010 - December 2013.